January 2022

# Photophysics Of Metalloporphyrins Strongly Coupled To Cavity Photons

Aleksandr Avramenko
*Wayne State University*

**PHOTOPHYSICS OF METALLOPORPHYRINS STRONGLY COUPLED TO CAVITY PHOTONS**

by

**ALEKSANDR GREGOROVICH AVRAMENKO**

**DISSERTATION**

Submitted to the Graduate School

of Wayne State University,

Detroit, Michigan

in partial fulfillment of the requirements

for the degree of

**DOCTOR OF PHILOSOPHY**

2022

MAJOR: PHYSICAL CHEMISTRY

Approved By:

_____

Advisor Date

_____

_____

_____

**DEDICATION**

To Tetiana M. Avramenko, whose support made this work possible.

**ACKNOWLEDGEMENTS**

I would like to thank some of the people that helped me reach this point of my studies. First, I would like to thank my undergraduate professors for building the knowledge base which I continue to rely on. In particular, I would like to thank Professor Brandon Canfield for introducing me to a vast array of instruments and allowing me hands on access to conduct experiments. I would also like thank Professor Mark Paulsen, who first introduced me to physical chemistry. Second, I would like to thank my professors from Eastern Michigan University, Dr. John Texter and Dr. Vijay Mannari, both of whom were very patient in their teaching, in particular since I knew little about coatings when I started the program. Third, I would like to thank my advisor, Dr. Aaron Rury. Through my time at Wayne State University I have been involved in multiple projects, ranging from working with Dr. Adedayo Sanni in constructing hybrid organic-inorganic perovskites to creating LabVIEW programs for the instrumentation in our laboratory. I feel it was a big advantage that I was exposed to such a wide range of research projects, as many graduate students often do not have a chance to work outside of their field of specialty. I would also like to thank Professors Vladimir Chernyak and Ivan Avrutsky for their availability and collaboration, in particular, helping me understand the principles of distributed Bragg reflectors and strong light-matter coupling. Finally, I would like to thank my wife, Tetiana Avramenko. When I met my wife I was an Army medic on leave while deployed to Afghanistan. While I was a good soldier I did not see myself pursuing a military career. However, I was always interested in science, my wife encouraged me to pursue these interests, which resulted in me focusing on studying chemistry.

**TABLE OF CONTENTS**

**LIST OF TABLES**

**LIST OF FIGURES**

# CHAPTER 1 INTRODUCTION TO HYBRID-LIGHT MATTER STATES

## 1.1 Introduction to the physics of hybrid light-matter states

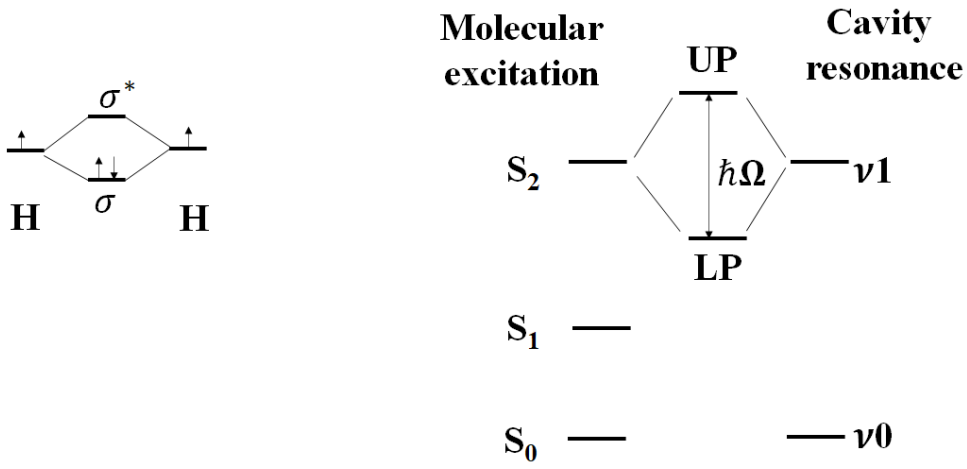


Figure 1.1: The formation of hybrid light-matter states due to the interaction between the $S_2$ energy level of a porphyrin molecule and a resonant cavity photon can be visualized as being analogous to the formation of bonding and anti-bonding orbitals in a hydrogen atom.

Interactions between light and matter is a fundamental part of chemical sciences, being responsible for photophysical processes such as phosphorescence and fluorescence. The first step in a photophysical process is a molecular electron transition from a molecule's ground to excited state. A molecular electron transition may occur when an incident photon's frequency matches the frequency difference between two electronic states of molecule[1]. By constructing a Fabry-Pérot cavity, which traps light of a certain frequency, then placing a molecule in a cavity that undergoes a molecular electron transition at the same frequency we force light-matter interaction. If the energy exchange between the light of the cavity mode and the molecule's excited state is faster than the decay rate of either state, then the system enters the strong coupling regime where a hybrid light-matter state is sustained. Figure 1.2 shows how this strong coupling can lead to a formation of hybrid

light-matter states called the upper polariton (UP) and the lower polariton (LP), which have an energy different from either of the starting states[2,3]. This phenomenon is similar to the molecular orbital picture when describing the formation of a hydrogen molecule, as seen in Figure 1.1. In the molecular orbital picture two atomic orbitals interact to form two molecular orbitals, the bonding and anti-bonding orbitals, just as the photon and molecular modes of a cavity interact to form the two polariton energy levels. A polariton is a hybrid light-matter state that must be described by referencing both, the photon mode, and the molecular resonance mode, as seen in Eqs (1.1) and (1.2)[2,4,5],

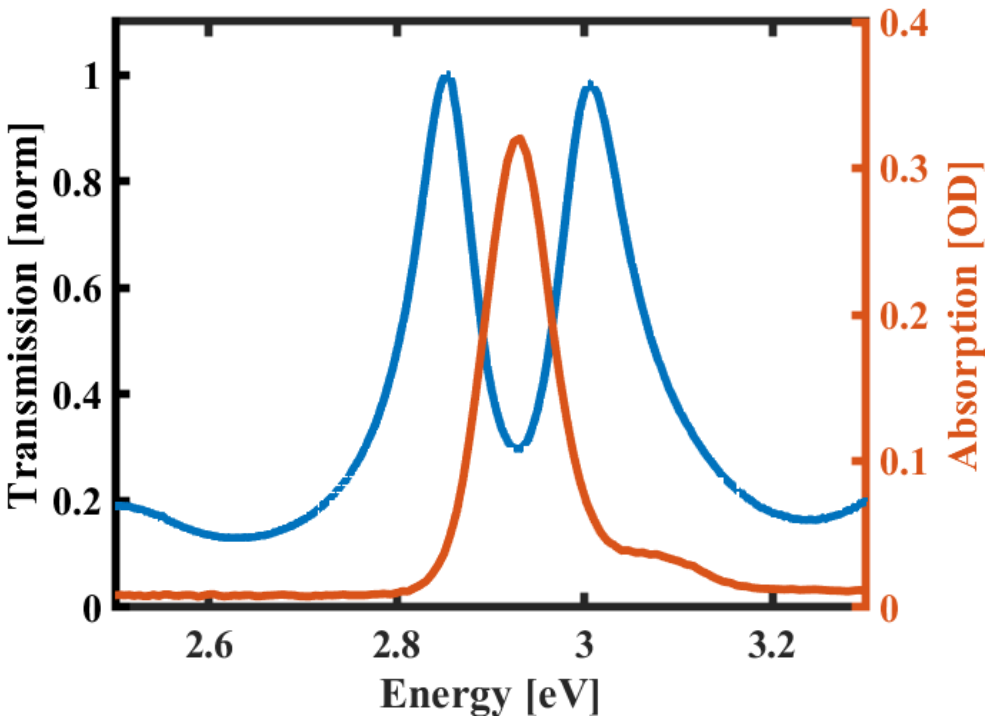


Figure 1.2: Comparison of the Soret band (red) of a Zinc (II) tetraphenyl porphyrin molecule to the normalized transmission spectra of the molecule in a Fabry-Pérot cavity (blue). The single Soret band splits into two peaks, an upper and a lower polariton separated by a Rabi splitting of ∼160 meV

$$|UP\rangle = \frac{1}{\sqrt{2}}[|e\rangle_e|0\rangle_c + |g\rangle_e|1\rangle_c] \tag{1.1}$$

$$\left|LP\right\rangle = \frac{1}{\sqrt{2}}[\left|e\right\rangle_e\left|0\right\rangle_c - \left|g\right\rangle_e\left|1\right\rangle_c] \tag{1.2}$$

in the above equation $\left|\mathrm{e}\right\rangle_e$ and $\left|\mathrm{g}\right\rangle_e$ describe the excited and ground state of the chromophore with 0 and 1 photons in the cavity respectively.

The energy difference between the UP and LP states is referred to as the Rabi splitting. Without accounting for dissipation, the Rabi splitting can be estimated as[2,6],

$$\hbar\Omega = 2d\sqrt{\frac{\hbar\omega}{2\epsilon_0\nu}} \times \sqrt{(n_{photon}+1)}, \tag{1.3}$$

where $\hbar\Omega$ is the cavity resonance near the excitation energy, $\epsilon_0$ is the vacuum permittivity, $\nu$ is the volume of the electromagnetic mode, and $n_{photon}$ is the number of photons in the cavity. From Eq. (1.3) we observe that the polariton is sustained even in the absence of photons. We also observe that the Rabi splitting will be proportional to the square of the excitation energy. Typically, the volume of the electromagnetic mode is much larger than the volume of the molecule that is coupling to the cavity photon. Therefore, many molecules are expected to couple to a single cavity photon, increasing the Rabi splitting. The Rabi splitting will be proportional to the square root of the number of molecules divided by the electromagnetic volume, or the square of the concentration, $\hbar\Omega \propto \sqrt{\frac{N}{\nu}} = \sqrt{C}$[2,6]. Maximum absorption will occur when the dipole moment of the molecules and the electric field are parallel. Because the orientation of molecular dipoles is often randomized there will be a large number of molecules that will form uncoupled states. These uncoupled states do not participate in polariton formation. Beside the uncoupled states we must account for the formation of so-called "dark states" within our polariton system. We can

imagine that the number of molecules coupled to a cavity photon as some arbitrarily large number N. These N number of molecules interact with a single cavity photon, leading to the creation of a total of N+1 collective states. Out of all of the collective states there will form two polariton states, one UP state, one LP state, leaving N-1 dark states. In simple terms, these dark states can be thought of as a superposition of molecular excitations with a very small photonic contribution. Despite not being spectroscopically observable, these states play an important role in polariton dynamics and will be discussed in Chapter 2.

Because of their partially photonic nature hybrid light-matter states take on a dispersive characteristic[2,7]. The behavior of a purely photonic state can be described as $E_{ph}(\theta) = E_{cutoff}\left(1 - \frac{sin^2\theta}{n_{eff}}\right)^{-1/2}$[7,8]. Where $E_{cutoff}$ is the cavity cutoff energy calculated as $E_{cutoff} = \frac{hc}{2n_{eff}L}$[6,7,9]. The dispersivity of a hybrid light-matter state formed by coupling a single exciton to a single cavity photon must be described by the two level interaction Hamiltonian[10],

$$\begin{bmatrix} E_{ph} & \frac{\hbar\Omega}{2} \\ \frac{\hbar\Omega}{2} & E_{ex} \end{bmatrix} \begin{bmatrix} \alpha \\ \beta \end{bmatrix} = \epsilon \begin{bmatrix} \alpha \\ \beta \end{bmatrix} \tag{1.4}$$

where $\hbar\Omega$ is the coupling between the photon and the exciton. By examining the Hamiltonian, it is clear there will be two energy eigenvalues representing the UP and LP. The values $\alpha$ and $\beta$ are the Hopfield coefficients and represent the photonic and excitonic contribution to the polariton states[11–13]. It should be noted that this model assumes that a single exciton is coupling to a single cavity photon. However, cavities in which multiple excitons couple to a single cavity photon are also possible[7,14]. In this case the matrix in Eq. (1.4) would be expanded to include the additional exciton and the interaction terms.

Moreover, the number of the final polariton states created should equal the number of starting states. Therefore, a system in which three components are involved, two excitons and one photon, would result in the formation of three polaritons, an upper, middle, and lower state.

So far, we have not accounted for dissipation of energy within the cavity system. Polaritons are sustained by energy exchange between resonant molecular and photon modes. Molecules in the excited state will naturally decay to the lowest energy state, be it by the emission of a photon or through nonradiative decay pathways. A free space molecule will have a propensity to move along the excited state potential energy surface (PES) to the lower energy ground state[15].Just as the lifetime of the molecular excited state is finite so is the lifetime of a cavity photon. The cavity photon lifetime is limited to several femtoseconds, depending on the size and reflectivity of the cavity[16]. Because the nature of the cavity controls the characteristics of the photon mode, proper cavity design is essential in creating hybrid light-matter states.

## 1.2 Cavity design

Building a cavity that entraps the proper photon to exchange energy with a molecular excitation is perhaps the most important step to polariton formation. In this work I will focus on forming polaritons using the Soret band of porphyrin molecules, which is formed by exciting the molecules into the $S_2$ state. During my experiments I measured the full width half maximum (FWHM) of this molecular mode to be 0.04584 eV-0.05622 eV while embedded in a polymer matrix. In order to enter the "strong coupling" regime the maximum Rabi splitting must be larger than the FWHM of either the photon or molecular

modes[2,4]. While the FWHM of the molecule is dependent on the local environment and is difficult to manipulate, it is possible to deterministically control the photon mode by manipulating the parameters of the Fabry-Pérot cavity[16,17].

The Fabry-Pérot cavity consists of two parallel mirrors separated by some distance. Light entering the structure will be repeatedly reflected by the two mirrors. Most of the light waves will be attenuated as they interfere with each other during reflection between the two mirrors. However, there will exist a wavelength whose $\frac{\lambda}{2}$ is equal to the distance between the mirrors. The transmittance of this mode and its harmonics will be greatly amplified. The spacing between the fundamental frequency and its subsequent harmonic is referred to as the Free Spectral Range (FSR). Expressed in frequency terms it is defined as $FSR = \frac{c}{2nd}$, where $d$ is the distance between the mirrors and $n$ is the refractive index of the spacer layer between the mirrors[16].

The Finesse of a Fabry-Pérot cavity is the relation of the Free Spectral Range to the FWHM, $F = \frac{FSR}{FWHM}$. The finesse is a measure of how narrow each resonance peak is. The higher the finesse, the narrower the resonance peaks. Finesse is also related to the reflectance of the mirrors[16,17]:

$$F = \frac{2\pi}{\ln(\frac{1}{R_1 R_2})} \tag{1.5}$$

A photon mode whose FWHM was similar to that of the molecular mode would result in the largest number of excited state porphyrin molecules interacting with the cavity photon. Because the FSR and FWHM are calculated based on the properties of the chromophore absorption peak when designing cavity polariton structures, all that is needed is

to calculate the finesse and the reflectance of the mirrors using Eq. (1.5).

Another important metric in cavity design is the structure's round trip attenuation coefficient. This component measures how the intensity of a photon decreases during a single round trip inside the cavity structure and is expressed as[16],

$$r = R_1 R_2 exp(-2\alpha nd) \tag{1.6}$$

where $R_1$ and $R_2$ is the reflectively of the two mirrors forming the cavity and $\alpha$ is the loss coefficient $\alpha = \frac{1}{2nd} \ln \frac{1}{R_1 R_2}$. By using the information from Eqs. 1.5 and 1.6 the intensity of the photons in the cavity can now be modeled[16]:

$$I_{max} = \frac{I_0}{(1- \mid r \mid)^2} \tag{1.7}$$

$$I_{final} = \frac{I_{max}}{1 + (\frac{2F}{\pi})^2 sin^2(\frac{\pi \nu_{incidence}}{\nu_{FSR}})} \tag{1.8}$$

## 1.3 Mirror design

Once the required reflectance of the mirrors has been calculated it is necessary to properly design them. One method would be to use two metallic mirrors separated by a polymer spacer layer. While this is a method that has been shown to form hybrid light-matter states it possesses certain limitations[18]. Our experimental goal is to form a cavity which has relatively high reflectivity around the Soret band. However, we also require relatively low reflectivity around the Q band so that the lower lying state could be probed. A metallic mirror thick enough to give us the required reflectance in the Soret region would also reflect a high amount of light in the Q region[19]. This would reduce the efficiency of pump

and probe pulses interrogating the sample. Perhaps most importantly, metallic films are more susceptible to damage and, as is the case for silver, which will react with oxygen to form silver oxide, resulting in the change in its reflective properties. Studies by Burge, Bennett *et al.* found that in a normal laboratory setting a 0.1 nm tarnished layer appeared as soon as 1 hour after deposition of a silver film, growing to 6 nm in one month[20]. By using distributed Bragg reflectors (DBRs) we can manipulate the reflectance over the desired Soret region while allowing more light transmission in parts of the electromagnetic spectrum we are interested in probing. We are also able to store DBRs in a laboratory setting for an extended period without the mirror losing its optical properties.

To understand how reflectance and transmission is manipulated by DBRs we recall that a light wave is a periodic structure, that is the time between two successive peaks in a light wave will be consistent. When light passes through a periodic medium wavelengths whose size match the periodicity of the medium its intensity will be attenuated[16,21]. To achieve periodicity a DBR is typically constructed as a layered material of alternating refractive indices. I utilize $SiO_2$ and $Si_3N_4$ as the periodic materials in my DBR structures. To determine the transmission of a wave through a DBR structure it is first necessary to understand the behavior of light at a single DBR interface. This is achieved by utilizing the Fresnel equations for reflectance and transmission[21]:

$$r = \frac{n_1 - n_2}{n_1 + n_2} \tag{1.9}$$

$$t = \frac{2n_1}{n_1 + n_2} \tag{1.10}$$

To obtain the final reflectance and transmission the Fresnel equations must be cal-

culated at each boundary of the DBR. To keep track of the transmission and reflectance coefficients the scatter matrix is used[16,22]:

$$S = \begin{bmatrix} t_{12} & r_{21} \\ r_{12} & t_{21} \end{bmatrix} = \begin{bmatrix} \frac{2n_1}{n_1+n_2} & \frac{n_2-n_1}{n_2+n_1} \\ \frac{n_1-n_2}{n_1+n_2} & \frac{2n_2}{n_2+n_1} \end{bmatrix} \tag{1.11}$$

The $t_{12}$ coefficient represents transmission from medium 1 to medium 2 while $t_{21}$ represents transmission of the light back from medium 2 to medium 1. Similarly, $r_{12}$ represents reflection from medium 1 to medium 2 while $r_{21}$ represents reflection from medium 2 to medium 1. A single 2x2 scatter matrix represents light interaction at a single boundary of a DBR. The DBRs used in my experiments were typically 11-13 layer structures. The scatter matrix only accounts for the behavior of light through a single interface. To calculate the transmittance through the entire DBR I convert the scatter matrix into a wave-transfer matrix using the relationship[16]:

$$M = \begin{bmatrix} \frac{t_{12}t_{21}-r_{12}r_{21}}{t_{12}} & \frac{r_{21}}{t_{12}} \\ \frac{r_{12}}{t_{12}} & \frac{1}{t_{12}} \end{bmatrix} \tag{1.12}$$

By substituting the Fresnel equations into the wave transfer matrix in Eq. (1.12) it is possible to solve for the transmittance of an entire DBR structure by multiplying the transfer matrices created at each boundary of the DBR. To simplify this computation we rely on the relationship that transmittance power $T_f = |t^2|$. $T_f$ is defined as[16],

$$T_f = \frac{T_i}{T_i + \Psi^2(1 - T_i)} \tag{1.13}$$

where $T_i$ is the single segment transmission based on Fresnel equations and $\Psi$ is a factor

accounting for interference inside the DBR structure defined as $\Psi = \frac{sinN\Phi}{sin\Phi}$, where N is the number of DBR segments. $\Phi$ is a factor that represents single segment transmittance inside the DBR and is calculated as[16]:

$$\Phi = acos[\frac{(n_1+n_2)^2}{2n_1n_2}cos(\phi_1+\phi_2) - \frac{(n_1-n_2)^2}{2n_1n_2}cos(\phi_1-\phi_2)] \tag{1.14}$$

In Eq 1.14 $\phi_1 + \phi_2 = \frac{\pi\nu}{\nu_b}$ and $\phi_1 - \phi_2 = (\frac{n_1d_1-n2d_2}{n_1d_1+n2d_2})\frac{\pi\nu}{\nu_b}$ and $\nu_b$ is the Bragg frequency: $v_b = \frac{c}{2[(n_1d_2)+(n_2d_2)]}$. Finally, some conclusions of how the transmission of an incidence wave will depend on the incidence frequency $\nu$ can be made. First, wavelengths that are near $\frac{\lambda}{4n_{avg}}$ will be maximally transmitted. This area of maximal transmittance is referred to as the stop band. Second, as the number of segments increases the final transmission will decrease. This can be understood by examining the wave transfer matrix. After each successive layer the transmission power will be reduced. Lastly, increasing the difference between $n_1$ and $n_2$ will cause an increase in the FWHM of the stop band. My goal is to form hybrid light-matter states using the Soret band of porphyrins, which lies between 2.92-2.98 eV depending on the type of porphyrin used. The mirrors would also need to create a cavity mode with a FWHM of $\sim$0.05 eV. Based on the described formalism the approximate thickness of individual $SiO_2$ and $Si_3N_4$ layers would be $\sim$60 nm and require 11 layers. While I focus on discussing transmissive behavior of a DBR, it should be noted that in the absence of absorption, the reflected power can be related to the transmitted power through the relationship $R = 1 - T$[16].

## 1.4 History and application of strong light-matter coupling

Early studies of strong-light matter interaction involved forming hybrid light-matter states by coupling the excitons of a quantum well semiconductor to a cavity photon. The small exciton binding energy of most quantum well materials caused these structures to be highly sensitive to temperature changes[23–25]. Lidzey *et al.* were the first to form polaritons using an organometallic molecule[26]. The ability to strongly couple molecular excitations to resonant cavity photons presented the question of how polariton formation would impact the photochemistry and photophysics of a molecule?

Ebbesen *et al.* showed that the reaction rate of photoisomerization of a spiropyran molecule were considerably slower under strong light-matter coupling conditions[6]. Because a molecule's reactivity is dominated by the shape of its potential energy surface (PES) it is necessary to understand how the formation of polaritons impacts its PES. If we imagine a model molecule without strong-light matter coupling, then we can assign three PESs, the ground state, $V_g$, the excited state $V_e$, and the photo-excited cavity state $V_c$. The $V_c$ PES will simply be a copy of the ground state PES shifted by the energy of the photon: $V_g + \nu_{ph}$[27,28]. When light-matter coupling becomes strong enough, and if $V_e$ and $V_c$ are close in energy, then the two states can hybridize, forming a polariton PES. During hybridization the $V_c$ PES will inherit exciton properties from $V_e$, while $V_e$ will inherit some light-like properties from $V_c$. This hybridization is believed to result in the polariton PES possessing a shape unique to that of either the $V_e$ or $V_c$ states[27,28]. In particular, because the polariton states are separated by the Rabi splitting energy, the lower polariton state is pushed down in energy in the area where the coupling is the strongest. Galego *et al.*

calculated that these effects, which re-shape the polariton PES could be used to suppress the photoisomerization reaction of a stilbene molecule[27].

While the aforementioned studies showed that polariton formation can be used to impact the photochemistry of molecules, they did not address what relaxation mechanisms are involved when a molecule is in the strong coupling regime and near the resonance point. Houdré, Ilegems and coworkers considered how inhomogeneous (Gaussian) broadening would impact the linewidth of a polariton system[29]. It was determined that polariton linewidths will inherit the average homogeneous lineshape $(\gamma_c+\gamma_e)/2$ of the photon and exciton respectively when the Rabi splitting is large. However, as the interaction between the photon and molecular modes decreases the lineshape inherits a more inhomogeneous characteristic; $(\gamma_c+\sigma_e)/2$. Whittacker *et al.* observed that lineshapes of a InGaAs cavity's lower polariton are below the predicted $(\gamma_c+\sigma_e)/2$ value, attributing this to a motional narrowing effect[30]. Moreover, the model described by Ilgems *et al.* predicted identical lineshapes for the upper and lower polaritons. However, it was observed on multiple occasions that the lifetime of the lower polariton was longer than that of the upper polariton[3,30–32]. Lidzey and Agranovich invoked Fermi's golden rule to explain this discrepancy in semiconductor microcavities[33]. In summary, the rate of a quantum transition is faster to a state with higher density of final states than to a state with a lower density of final states, provided they are mediated by the same perturbation. In a polariton system the density of dark states is large compared to that of the polariton states, allowing for a fast transition between the upper polariton and dark states. The authors also described the dark states as a broad collection of incoherent states, with the dark states assuming a "dark band" configuration. This model was further expanded by Lidzey *et al.* by additionally

accounting for the changes in photon fraction with cavity detuning and the optical decay of the photons from the cavity[34]. Based on these studies molecular dynamics of hybrid light-matter states are expected to be heavily impacted by the formation of the dark states. Indeed, while studying the impact of strong light-matter coupling on reverse intersystem crossing Kena-Cohen, Eizen and co-workers reported that the rate was unchanged when the molecule was under strong light-matter coupling conditions. This was despite the energy of the lower polariton being inverted relative to that of the triplet states. The authors attributed this to the large density of states of the dark states as compared to the lower polariton[35]. While these models provide a good approximation for the dynamics of cavity polaritons there exists ambiguity of how these results can be applied to the photophysics and photochemistry fields. Polaritons are hybrid states, which partially inherit the nature of a molecule. However, each molecule has unique properties with a unique potential energy surface. It remains an open question how properties such as vibronic coupling between the B and Q states in porphyrin molecules or internal conversion is impacted by polariton formation.

Ebbesen *et al.* showed that while fluorescence is present in the lower polariton, the nonradiative decay pathway is the dominant mechanism for the polariton state in a TDBC dye (5,6-Dichloro-2-[[5,6-dichloro-1-ethyl-3-(4-sulfobutyl)benzimidazol-2-ylidene]propenyl]-1-ethyl-3-(4-sulfobutyl)benzimidazolium hydroxide)[32].The rate of nonradiative relaxation, such as internal conversion, is dependent on the gap law, which generally states that that the rate is proportional to the energy gap between the higher and lower lying states[36]. Despite the gap law being defined over fifty years ago chemists still lack a deterministic way to control internal conversion through traditional synthesis methods. In my work I have

found evidence that the rates of internal conversion of a Zinc (II) tetraphenyl porphyrin (ZnTPP) molecule are directly impacted by polariton formation[4]. More specifically, the rate of internal conversion between the $S_2$ and $S_1$ states increased as the Rabi splitting was made larger. While the study demonstrated that polariton formation can exhibit rational control over internal conversion, the rates of internal conversion measured also did not match the established gap law. The reasons behind this disagreement will be discussed in Chapter 2. Furthermore, I provide evidence that under strong light-matter coupling conditions the vibronic coupling between B and Q states of Copper tetraphenylporphyrin (CuTPP) leads to the formation of a "Herzberg-Teller" polariton below the $S_1$ energy of the CuTPP molecule.

Polaritons are a hybridization of light and matter and inherit properties of both states. However, as long as the excitons meet a certain criteria such as having a matching energy with the photon and having sufficient oscillator strength, there is no set limit to how many exciton states can couple to a cavity photon. Naturally, it is easy to assume that such a structure would have some hybrid characteristic of the three or more starting states. Research on studying such multi-layer cavities has been ongoing. Lidzey *et al.* created a multi-layer cavity system consisting of two J-aggregates whose absorption peaks were separated by 0.064 eV and were spaced apart by a 100 nm polystyrene layer. The authors observed that the photoluminescence from the lower polariton and middle polariton states varies with angle[14]. Ebbesen *et al.* observed a similar phenomenon in that fluorescence from the lower polariton was dominant when forming polaritons using J-aggregates. However, they did not use a multi-layer cavity, coupling only one type of molecule to a cavity photon. Ebbesen *et al.* attributed this to Kasha's rule, in which emission from the lowest

lying state is expected to dominate[3]. Agranovich *et al.* described the emission from a two level J-aggregate system that assumes the upper polariton can quickly decay into the lower branch when $\Delta E = E_{up} - E_{lp} = h\nu$[37]. If the Rabi splitting is close to $h\nu$, then energy transfer from the upper to the lower branch can rapidly occur. Lidzey *et al.* modified this model to describe the emission of their three level system, where energy transfer was allowed not just between the upper and lower polariton, but between the upper and middle, and middle and lower polaritons. The model produced good fits at angles below cavity resonance, however, the fit above resonance was less satisfying. Lidzey *et al.* also demonstrated the hybridization between organic and inorganic excitons by forming cavity polaritons using J-aggregates and InGaP quantum wells. Hybridization using multiple excitons opened the possibility to creating structures, which possess chemical properties of both species. Forrest *et al.* expanded on this work by hybridizing two nearly degenerate exciton states of an napthalene tetracarboxylic dianhydride (NTCDA) molecule and Zinc Oxide (ZnO) nanoparticles. The authors concluded that the excitonic portion of the upper polariton was a mixture of the NTCDA/ZnO excitons. While the lower polariton's dominant exciton component was the NTCDA exciton. Moreover, the authors observed an increase in the Rabi splitting of 1.44 times in the hybrid cavity over the pure NTCDA cavity, which they attributed to as evidence that both excitons couple to the cavity simultaneously[7].

Impact of polariton formation on energy transfer processes such as the Förster mechanism are another area which has attracted scientific interest. The Förster resonance energy transfer (FRET) is nonradiative and relies on dipole-dipole interactions between the donor and acceptor molecules[1]. The rate of Förster resonance energy transfer is also highly sensitive to distance between the donor and acceptor molecules as well as the spectral overlap

between the donor emission and acceptor absorption spectra. Recently, scientists have attempted to overcome this limitation by using hybrid light-matter states[18,38]. Ebbesen *et al.* studied the energy transfer of between two dye molecules, using TDBC as a donor and a triethylammonium salt (BRK 5714) acceptor. The donor molecule had a strong absorption peak in the 590 nm region, while the acceptor molecule had a strong emission peak in the 659 nm region. The authors varied the spacer layer thickness between 10-75 nm. The authors reported that when excited outside the cavity only emission from the TDBC donor is observed. However, under strong light-matter coupling emission from both, TDBC, and BRK are observed, suggesting an energy transfer process between the two molecules is occuring[18]. Moreover, the authors reported this process occurred independent of distance. Most recently, Scholes *et al*. concluded that the delocalized nature of polaritons can serve as an advantage in improving change transfer along a donor-acceptor interface[38]. The authors created a bi-layer cavity using a P3HT donor and a PCBM acceptor. When excited near the dark state resonance they find the presence of a new decay pathway in their excited state absorption spectra. The new decay pathway is not present in a P3HT neat cavity, suggesting the presence of acceptor molecules is required for the observation of this pathway, and therefore, that this decay channel plays a role in charge transfer. The authors conclude that the delocalized nature of the polariton states allows for efficient donor-acceptor interaction. However, as a trade-off the charge transfer reaction is slowed. This is because while the polariton is delocalized the acceptor molecule is not. Each acceptor molecule, therefore, interacts with only a small portion of the polariton. Thus, creating a structure in which both, the donor, and acceptor, are simultaneously coupled to a cavity photon should result in efficient donor-acceptor interaction and an efficient reaction.

In my work I create hybridized light-matter states by strong coupling spatially separated quasi-degenerate B states of CuTPP and $H_2$TPP. The absorption and emission band of these molecules is separated by hundreds of meV. I use a three oscillator Hamiltonian to model the dispersive behavior of the cavity structure from which I extract the Hopfield coefficients. This is done to establish the photonic and excitonic nature of such a three level system so that the correct angle and energy is selected when probing the energy transfer mechanism in the cavity. My calculations show that polariton formation from quasi-degenerate excitons whose energies are separated by less than $1\%$ leads to each polariton branch inheriting a vastly different excitonic character. The middle polariton branch was also calculated to have a negligible amount of photonic content, suggesting its dynamics would be dominated by a mixture of the two excitonic states. Moreover, we observe a decrease in the lineshape of the quasi-degenerate CuTPP/$H_2$TPP cavities near resonance, which was predicted by Whittacker's motional narrowing model[30,39].

# CHAPTER 2 LOCAL MOLECULAR PROBES OF ULTRAFAST RELAXATION CHANNELS IN STRONGLY COUPLED METALLOPORPHYRIN-CAVITY SYSTEMS

Reproduced from (A. G. Avramenko and A. S. Rury, "Local molecular probes of ultrafast relaxation channels in strongly coupled metalloporphyrin-cavity systems" The Journal of Chemical Physics, vol. 155, no. 6, p. 064702, 2021.), with the permission of AIP Publishing.

## 2.1 Introduction

The manipulation of excited state molecular dynamics via fully quantum mechanical means remains one of the central goals of the chemical physics community. To achieve this lofty goal researchers have begun to assess the ability of resonator photons to control the photophysics and photochemistry of cavity-confined molecules[2,4,5,11,18,28,35,40–56]. In particular, by embedding photo-activated molecules in a nano or micro-scale electromagnetic resonator one can take advantage of the quantum nature of photonic fluctuations to form strongly coupled states of light and molecular electrons known as cavity polaritons. Over the course of the last few years theorists have predicted cavity polariton formation amends several molecular properties including photochemical rates[28,44,46,47,57] and excited state photophysical processes such as singlet fission[50].

In contrast to these theoretical predictions, studies examining the experimental dynamics of molecular polaritons conclude the presence of a large density of dark states corresponding to molecules uncoupled from cavity photons impedes the precise manipulation of excited state molecular processes central to quantum mechanically controlled optoelectronic technologies[34,35,56]. In particular, the authors of these studies propose when one excites the higher energy of the two polariton states, the upper polariton (UP), localization into the reservoir of dark states (DS) out-competes non-radiative relaxation into the lower

polariton (LP) and complicates how polariton formation can be used to amend molecular dynamics crucial to applications such as lasers, light emitting diodes, and photo-catalytic platforms. Despite these claims, it remains unclear if the dynamics uncovered in these studies stem from the choice of optical transitions to probe.

Given their large linear and nonlinear interactions with light, many researchers examine polariton dynamics by measuring changes in the transmission or reflection of a probe pulse resonant with one or both of the polaritonic transitions[56,58]. While straightforward in principle, the collective nature and many-body interactions necessary to form stable polaritons complicates the interpretation of these dynamical spectroscopic signals. Specifically, recent studies report non-zero $\Delta T/T$ or $\Delta R/R$ signatures appear at the polariton energies for pump-probe time delays exceeding the known lifetimes of molecular excited states[56,58]. Researchers propose these features result from a variety of sources ranging from reduction of the vacuum Rabi splitting energy due to depletion of the molecular ground state and excited state absorption into the manifold of multi-polaritonic states.

The choice of probe energy in assessing the ultrafast dynamics of cavity polaritons can be cast clearly by considering samples in which zinc (II) tetraphenyl porphyrin (ZnTPP) molecules couple strongly to photonic fluctuations in micro-scale Fabry-Pérot cavity structures. Early studies by Lidzey and co-workers indicated the lower polariton (LP) state relaxed into the states of localized ZnTPP molecules at a rate of 0.33 $ps^{-1}$ and did not depend dramatically on the Hopfield coefficients characterizing the photonic and molecular contributions to the LP state[59]. In stark contrast, we showed previously the ultrafast relaxation from the UP to the localized states of ZnTPP can occur as fast as 2.25 $ps^{-1}$ when we probed the dynamics experimentally through the lens of excited state absorption

processes imprinted onto the localized ZnTPP molecules[4]. Furthermore, we found this localization rate depended sensitively on the concentration of ZnTPP we embed within the resonator structure. These differences indicate local molecular probes can play an important role in assessing how polariton formation affects ultrafast relaxation dynamics of molecular moieties. While we showed experimentally the conversion of polaritons into localized molecules could occur more rapidly than thought previously, in that study we did not fundamentally assess the dynamical mechanism of polaritonic control. Moreover, we did not extend our studies to other metalloporphyrin moieties to uncover trends in cavity-amended dynamics.

In this study we systematically analyze both steady-state and time-resolved spectroscopic measurements to understand how polariton formation affects non-radiative relaxation in ZnTPP and copper (II) tetraphenyl porphyrin (CuTPP). Like other metalloporphyrins, ZnTPP and CuTPP both posses two prominent absorptive transitions in the visible region, a transition between the $S_0$ and $S_2$, or B, states denoted the Soret transition near 400 nm and a transition between the $S_0$ and $S_1$, or Q, states near 530 nm. While both transitions stem from a degenerate set of HOMO states, configuration interactions split these states' energies and cause the observation of distinct peaks in the absorption spectrum in ZnTPP and CuTPP[60]. Given its significantly larger oscillator strength, we use the Soret transition of each molecule to form cavity polaritons, like several previous studies[4,5,59,61].

Our using ZnTPP and CuTPP to study polariton dynamics benefits from earlier work on the ultrafast dynamics of each molecule in solution phase. Zewail and co-workers show when one pumped the Soret transition of ZnTPP, the photoexcited electronic population internally converts with a rate of 0.67 $ps^{-1}$ to the molecule's Q state[62]. In addition, these

researchers found the B state of ZnTPP absorbs probe pulses possessing central energies between 2.14 eV and 1.77 eV, which allows one to characterize the internal conversion process directly through conventional pump-probe measurements. Furthermore, while they could not measure the dynamics of light emission from the B state excited initially with their pump pulse, they did find the B state emits fluorescence. This light emission competes with the internal conversion process and affects the overall efficiency of the non-radiative relaxation in ZnTPP.

Several studies report the ultrafast spectroscopic excited state dynamics of CuTPP differ significantly from those of ZnTPP[63–66]. Most recently, Jeong *et al*. show the initially excited B state of CuTPP decays to the molecule's Q state within the 100 fs temporal resolution of their time-resolved spectroscopic apparatus. Following this initial decay, these authors show the Q state relaxes into the manifold of triplet states at a rate of $\sim$4 ps$^{-1}$ in benzene. We found similar results in toluene. The ultrafast formation of the triplet states in CuTPP stems from the open shell configuration of the central Cu atom, which confers a total doublet multiplicity onto the molecular electronic states possessing both singlet and triplet spin configurations. While the fundamental processes governing the ultrafast dynamics of CuTpP differ from those that dominate similar dynamics in ZnTPP, several authors show the triplet absorption between 2.64 eV nm and 2.48 eV allows one to track the formation of triplet states directly following photo-excitation[63–66].

We leverage the existing knowledge of the ultrafast excited state dynamics of ZnTPP and CuTPP to study how cavity polariton formation affects non-radiative relaxation processes. In particular, we use the established spectral signatures of specific excited electronic states characteristic to localized molecules within cavity structures to assess the rates at

which polaritons formed from each respective chromophore localize. We also vary the concentration of each respective chromophore inside different Fabry-Pérot (FP) cavity structures to understand how the change in the collective coupling of photons and molecules affects polariton relaxation rates.

To achieve our goal, we develop quantitative models of the transmission spectra of cavity polaritons formed from each molecule and use the coherence of the photonic contribution to the polariton states as an additional restraint on relaxation rates of the polariton states imprinted on the properties of peaks corresponding to each polariton in steady-state transmission spectra. For the case of ZnTPP, we use these upper limits on the relaxation rates in a kinetic model to motivate a physical picture in which the vibronic couplings present in ZnTPP play a critical role in how polariton formation can control ultrafast excited state relaxation. We find the lifetime of the UP state reduces significantly as we increase the concentration of chromophores within the FP resonators. Based on currently predominant theories of polariton relaxation, we use a harmonic model of polaritonic potential energy surfaces to propose vibronic resonances enhance a direct, interpolaritonic nonradiative relaxation path that can populate the LP substantially before the UP decays to the DS manifold. Furthermore, vibrationally mediated relaxation from the dark states to the LP increase with the collective vacuum Rabi splitting energy, $\hbar\Omega_R$, and drive an overall increased rate of localization into cavity-embedded ZnTPP molecules. By comparing to models in which we neglect these interpolaritonic relaxation we find the accurate prediction of the ultrafast localization rates necessitates we include these direct channels.

In the case of CuTPP, we find the fastest dynamical signals we measure in cavity polariton samples differ significantly from those we measure in the solution phase. We find

the transient absorption (TA) signal stemming from triplet excited state absorption (ESA) at 2.64 eV decays with an initial rate that does not depend on the intracavity chromophore concentration systematically, but is significantly slower than the rise of the triplet ESA in solution. By comparing to steady-state photoluminescence spectra of nano-fabricated control samples, we propose the ultrafast TA dynamics of CuTPP cavity polaritons stem from a novel ESA signal that decays as strongly coupled molecules localize into their individual excited states. We propose further experimental measurements to determine the fundamental mechanism explaining these findings. Our results indicate the important role of local molecular probes can play in elucidating the ultrafast non-radiative dynamics central to applicability of molecular cavity polaritons in optoelectronic and photochemical technologies.

## 2.2 Methods

Microscale Fabry-Pérot resonators were fabricated by first depositing 13 alternating layers of $Si_3N_4$ and $SiO_2$ under UHV conditions on a cleaned, optical grade fused silica substrate. Using a transfer matrix model, we designed the layers to possess equal thicknesses of approximately 60 nm. *Ex situ* ellipsometry measurements following deposition of the first $Si_3N_4$ layer showed a film thickness of 59.55 nm, which we presume was reproduced within 1 nm for the subsequent layers in the structure. We then formed films of poly methyl methacrylate (PMMA) from anisole-toluene solutions containing different concentrations of ZnTPP and CuTPP. To form active resonator layers capable of sustaining cavity polaritons, we spun 470 $\mu$L of the polymer/chromophore solutions on the DBR structure at 5500 rpm for ZnTPP and 6000 rpm for CuTPP. We capped the cavity structures with Al

layers whose thicknesses varied from 12 nm to 20 nm depending on the performance of the deposition system. A transfer matrix model indicates we form polaritons due to excitations of the TM mode (Transverse Magnetic) of the DBR structure detuned from the Soret resonances of ZnTPP and CuTPP by -235 meV and -286 meV, respectively, at normal incidence using these fabrication parameters. Angularly resolved transmission measurements confirmed the formation of cavity polaritons for all the samples we fabricated, as we show below.

Steady-state transmission measurements were carried out using a fiber-coupled deuterium lamp, free space optics to collimate the lamp output and focus the resulting beam onto the cavity samples, and a fiber-coupled spectrometer (OceanOptics OceanFX). Steady-state transmission spectra were taken at several incident angles to observe the dispersive and anti-crossing behavior of the cavity polariton transmission peaks. In addition to the cavity polariton samples, we fabricated DBR structures without converting them into complete cavity samples to reduce significant portions of the background on the polariton transmission spectra due to the highly dispersive DBR reflectivity. After subtracting the DBR background, we collected cavity polariton transmission spectra using light polarized in the plane of the optical table to ensure excitation of the TM mode of the DBR structure. We also used this system to measure steady-state absorption spectra of ZnTPP and CuTPP in polymer precursor solutions and characterized the energies and widths of the peaks corresponding to the Soret transition in each molecule, as we discuss in the Results section below. Steady-state photoluminescence measurements on CuTPP polaritons and control samples were made with a Horiba XPLoRA PLUS micro-spectrometer. We collected light emission spectra following excitation at 2.33 eV in a back-scattering geometry using a 10x

microscope objective.

Ultrafast transient absorption measurements were carried out using the 1.55 eV output of a regenerative amplified seed pulse from a Titanium-doped sapphire oscillator (Spectra Physics Solstice Ace). We frequency-doubled a portion of the amplified output to form 3.1 eV pump pulses. We used another portion of the fundamental output for our probe pulse. After steering the two beams to the sample, we overlapped them in space and collected the transmitted or reflected portions of the probe beam. We then steered those portions of the probe beam to a Si photodiode to which we affixed a 30 meV wide band-pass filter chosen based on excited state absorption features pertinent to cavity polariton localization in samples formed from each respective metalloporphyrin. For ultrafast transient transmission measurements on ZnTPP polariton samples we used the band of white light continuum around 1.97 eV formed in a 3 mm thick sapphire plate to probe internal conversion from the B state manifold involved in polariton formation to the Q states of localized molecules. Additionally, we used the output of an optical parametric amplifier to form $<$50 fs pulses at 2.64 eV to probe the formation of triplet states in localized CuTPP molecules following polariton pumping. To ensure transient measurements under resonant conditions between the molecular resonances and vacuum electromagnetic field of the cavity mode, we angled the Fabry-Pérot structure nearly 50 $^\circ$ relative to the pump incidence direction. We construct the transient absorption signals by measuring both transient transmission and reflectivity using the equation $\Delta A = -\Delta T - \Delta R$. We extract the relaxation rates following pump excitation by deconvolving a Gaussian response function from the transient absorbance (TA) data whose shape matches that of the rise of the measured signal. We find these response functions change between $\sim$ 225 fs and $\sim$100 fs for transient

measurements on ZnTPP and CuTPP, respectively, which are consistent with the difference in the mechanism through which we form probe pulses in each measurement.

To establish a fundamental physical understanding of changes to the dynamics of ZnTPP polaritons as a function of $\hbar\Omega_R$, we used the numerical diagonalization of harmonic potential energy surfaces (PESs) of polariton states to compute their vibrational sub-states based on the methods of Mukamel and co-workers, which we used previously to understand the resonance Raman spectra of molecular polaritons theoretically[5,46,67,68]. This approach allowed us to compute the vibrational sub-structure of the each respective polariton state, their overlaps, and the matrix elements of different molecular operators, as we define below. We assigned the modes along which each chromophore re-organizes using density functional theory calculations with B3LYP exchange and correlation functionals[69–71] and the 6-31g(d,p) basis set as implemented in the Gaussian09 package[72].

## 2.3 Results

Figure 2.1 compares the UV-vis absorption spectra of ZnTPP and CuTPP in the region around the Soret resonance of each respective molecule to the transmission spectrum of a model cavity structure we computed using transfer matrix theory with the parameters detailed in the Methods section. Figure 2.1 shows the established blue-shift of the CuTPP Soret resonance relative to its counterpart in ZnTPP. Close inspection of the absorption spectra show the excited state photo-physics of each molecule differ despite the resemblance of the structure of their respective macrocycles. In particular, we can discern the presence of a clear vibronic overtone in the absorption spectrum of ZnTPP we assign to a nearly 1190 $cm^{-1}$ totally symmetric vibration found from DFT calculations and shown

Table 2.1: Quantitative comparison between the steady-state energy ($\hbar\omega$) and width ($\Gamma$) of Soret resonances in the absorption spectra of solution phase ZnTPP and CuTPP molecules and the energy and width of the transmission spectrum of a model cavity model consistent with our experimental fabrication parameters.

| **Sample** | $\hbar\omega$ **[eV]** | $\Gamma$ **[ps$^{-1}$]** |
|---|---|---|
| ZnTPP | 2.923±0.001 | 9.7±0.3 |
| CuTPP | 2.984±0.001 | 13.7±0.1 |
| Cavity | 2.900±0.07 | 11.8±0.1 |

in the top right panel of Figure 2.1. In contrast, we model the absorption spectrum of CuTPP using a 394 cm$^{-1}$ vibrational mode shown in the bottom right panel of Figure 2.1 whose low frequency causes the appearance of a shoulder on the blue-edge of the molecule's Soret resonance. This difference suggests the reorganization of the B state in each molecule differs due to the difference in the electronic configuration of each respective central metal cation, which is also consistent with difference in the B state lifetimes established experimentally in previous studies[62,65,66].

We model the cavity transmission spectrum for an incidence angle of 52° to simulate resonant photon-molecule interactions given the detuning of our resonator structures from the molecular resonances, as we detailed above. We find the width of the cavity resonance nearly matches that of each respective molecular resonance. We tabulate the energies and widths of each peak of Figure 2.1 in Table 2.1.

The comparison in Figure 2.1 confirms a fundamental difference in the collective nature of the electronic states of molecules and the photons in the cavity mode. In particular, we need to model the molecular absorption peaks using Gaussian lineshapes due to the inhomogeneous broadening caused by differences in the local microscopic environments surrounding each excited molecule and we cannot assess the lifetime of the B state of

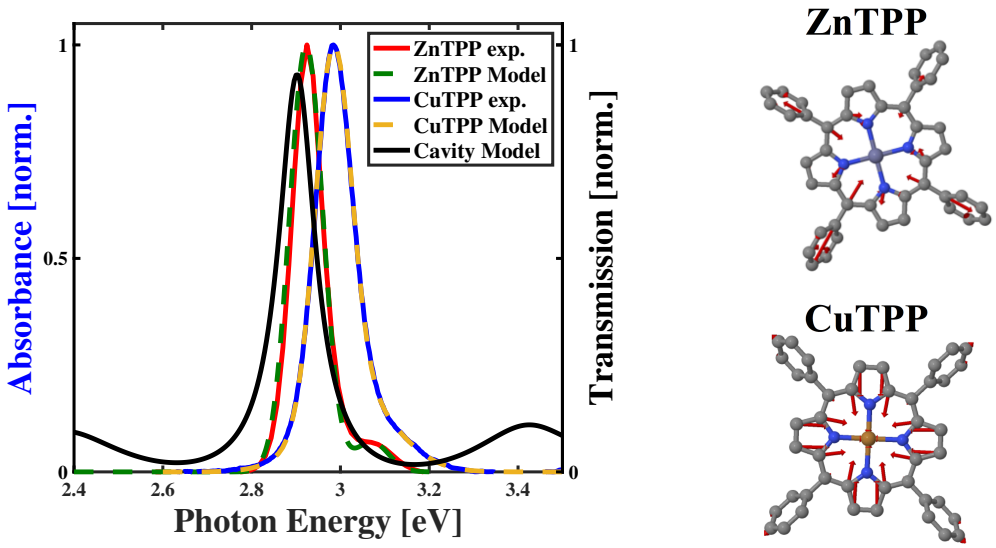


Figure 2.1: Left panel: comparison of the measured and modeled absorbance spectra of zinc (II) tetraphenyl porphyrin (ZnTPP) and copper (II) tetraphenyl porphyrin (CuTPP) to the transmission spectrum of a cavity mode calculated using our experimental fabrication parameters in a custom transfer matrix model. Model absorption spectra are calculated using harmonic potential energy surfaces displaced along reorganization modes identified by the vibronic overtones present in experimental spectra. We set the incident angle to 52° to approximate resonant molecule-cavity coupling for the CuTPP chromophore, as indicated by the overlap of those spectra. Top right panel: spatial representation of the eigenvector of a 1190 $cm^{-1}$ totally symmetric vibration of ZnTPP we assign as the mode along which the B state of this molecule re-organizes based on the linear absorption spectrum shown in the left panel. Bottom right panel: spatial representation of the eigenvector of a 394 $cm^{-1}$ totally symmetric vibration of CuTPP we assign as the mode along which the B state of this molecule re-organizes based on the linear absorption spectrum shown in the left panel.

either molecule from the width of the Soret peak directly. In contrast, the coherent nature of photons within the cavity mode means we can extract photonic lifetimes directly from the width of the Lorentzian peak in the model transmission spectrum.

The panels of Figure 2.2 compares the dispersion of the UP and LP states as a function of in-plane cavity photon momentum for three samples containing different concentrations of ZnTPP and three samples containing different concentrations of CuTPP. We model these dispersion curves using the equations[7,73],

$$E_{LP}(\theta) = \frac{E_{ph}(\theta) + E_{ex}}{2} - \frac{1}{2}\sqrt{[E_{ph}(\theta) - E_{ex}]^2 + 4V^2}, \tag{2.1a}$$

$$E_{UP}(\theta) = \frac{E_{ph}(\theta) + E_{ex}}{2} + \frac{1}{2}\sqrt{[E_{ph}(\theta) - E_{ex}]^2 + 4V^2}, \tag{2.1b}$$

where $E_{ph}(\theta) = E_{cutoff}\left(1 - \frac{sin^2\theta}{n_{eff}}\right)^{-1/2}$ is the dispersive energy of the cavity photon as a function of the angle the incident field makes with the surface normal of resonator structure, $\theta$, $E_{ex}$ is the energy of the excitonic Soret resonance, which we established from the models in Figure 2.1, and $V$ is the strength of the interaction between cavity photons and molecular excitons. Since we load the cavity structures with chromophores, we also allow for the adjustment of the intracavity index of refraction from that of neat PMMA, which we call $n_{eff}$[7]. We use the relation $\hbar\Omega_R = 2V$ to estimate the collective vacuum Rabi splitting for each polariton sample[73].

The dispersion curves of the cavity polariton transmission spectra for all our samples formed from polymer precursor solutions of ZnTPP and CuTPP demonstrate our successful formation of polaritons using both chromophores at all intracavity concentrations. These spectra show the polariton states formed using CuTPP lie at higher energies than their counterpart formed from ZnTPP, which conforms with the relative blue-shift of the Soret resonance of CuTPP when compared to ZnTPP we found in steady-state absorption spectra shown in Figure 1. We detail the model parameters used to explain the experimental dispersion curves in Table 2.2.

Unlike the case of cavity polariton formation using the progression of vibronic transitions common to acene molecules such as tetracene[53,56] and rubrene[74], we do not observe the formation of a middle polariton state when we strongly couple ZnTPP to cavity photons despite the presence of a vibronic overtone in this molecule's absorption spectrum. We attribute this difference in the polariton spectra of these respective samples to quan-

Table 2.2: Quantitative comparison between the collective vacuum Rabi splitting energies, cavity photon energy cutoff, and effective index of refraction found from models of the polariton dispersion curves shown in the panels of Figure 2.1.

| **Chromophore** | **Conc. [mM]** | $\hbar\omega_R$ **[meV]** | $E_{cutoff}$ **[eV]** | $n_{eff}$ |
|---|---|---|---|---|
| ZnTPP | 0.498 | 77 | 2.68 | 1.84 |
| | 0.996 | 108 | 2.66 | 1.84 |
| | 1.991 | 160 | 2.63 | 1.84 |
| CuTPP | 0.499 | 85 | 2.65 | 1.82 |
| | 0.988 | 117 | 2.66 | 1.82 |
| | 1.966 | 164 | 2.68 | 1.82 |

titative differences in the relative intensities of the vibronic overtones in these molecules. For example, while the 0-1 vibronic transition of tetracene is over 50% as intense as the 0-0 transition of this molecule in solution[75], we find the 0-1 vibronic overtone of the Soret resonance in ZnTPP is 7% as intense as the transition at the vibrational origin. This significant difference in the oscillator strengths of the vibronic transitions of ZnTPP implies one cannot form polaritons from 0-1 transition at the chromophore concentrations we use in our samples.

Given the collective nature of the coupling between the cavity photons and metalloporphyrin chromophores, we expect $\hbar\Omega_R \propto \sqrt{C}g^2$, where $g$ is the strength of the light-matter coupling and $N$ is the number of chromophores coupled to the cavity photons. Figure 2.3 confirms this expectation by showing the values of the collective vacuum Rabi splitting energies we find from our models using Eq. (2.1) obey square root dependence on the concentration of each chromophore we form in polymer precursor solutions prior to cavity fabrication.

Figure 2.4 shows the transmission spectra of cavity structures in which we embedded different concentrations of ZnTPP and CuTPP at angles that maintain the cavity-molecule resonance. One can discern the appearance of two distinct peaks in each of the transmis-

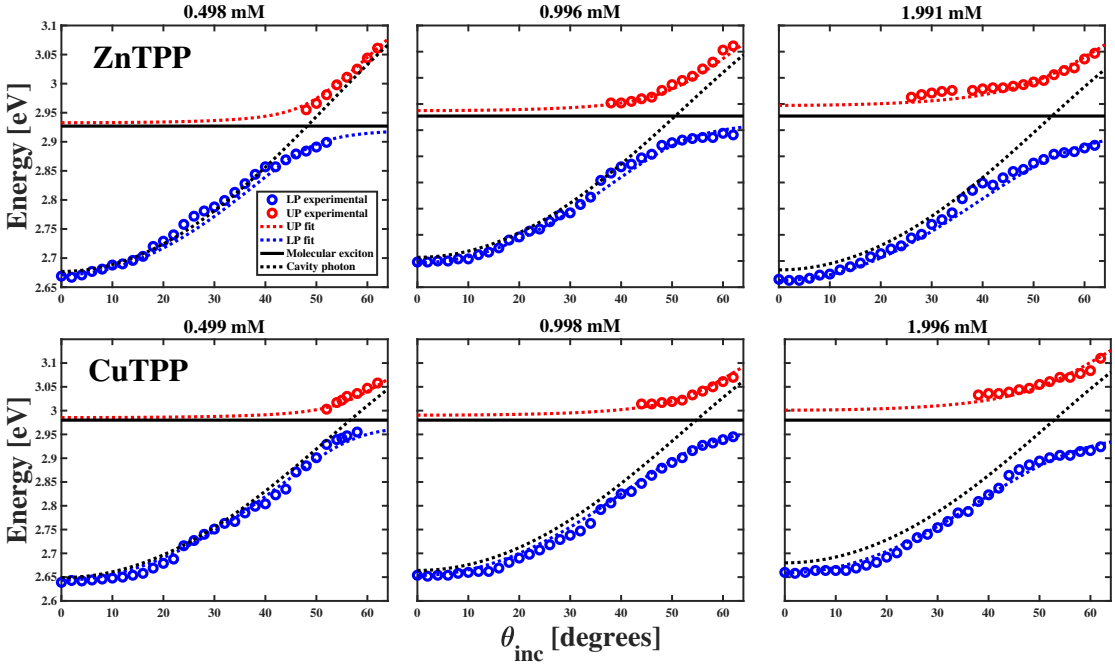


Figure 2.2: Top row of panels: comparison between the measured (open circles) and modeled (dashed line) dispersion of the upper polariton (UP, blue) and lower polariton (LP, red) states formed from the strong coupling of cavity photons to the Soret transition of ZnTPP molecules starting from a 0.498 mM (left), 0.996 mM (middle), and 1.991 mM (right) polymer precursor solutions. Bottom row of panels: comparison between the measured (open circles) and modeled (dashed line) dispersion of the upper polariton (UP, blue) and lower polariton (LP, red) states formed from the strong coupling of cavity photons to the Soret transition of CuTPP molecules starting from a 0.499 mM (left), 0.998 mM (middle), and 1.996 mM (right) polymer precursor solutions. The dispersion of the exciton Soret resonances and cavity photon energies are shown as solid and dashed black lines, respectively, in each panel.

sion spectra shown in Figure 2.4. However, the shapes of these peaks change as a function of the concentration of chromophores we embed in each respective cavity structure. In particular, we find the peaks corresponding to the UP states become increasingly asymmetric for polariton samples formed from the highest concentrations of both ZnTPP and CuTPP we consider.

To assess how the polariton states change in response to different concentrations of each molecule, we fit the peaks measured in the transmission spectra to Lorentzian shapes

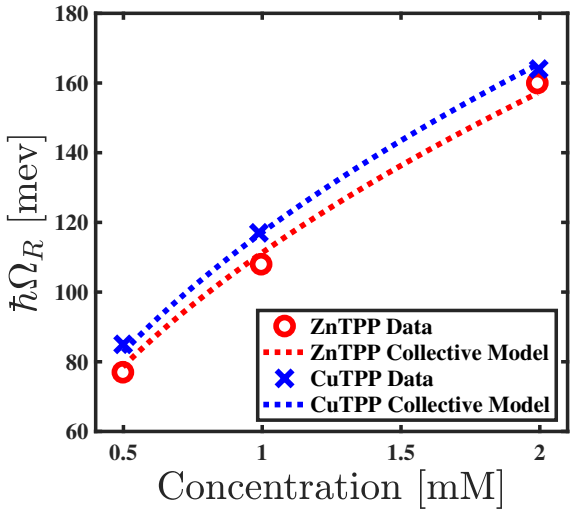


Figure 2.3: Comparison of the concentration dependent values of $\hbar\Omega_R$ found from the dispersion of cavity polariton states formed from ZnTPP (red circles) and CuTPP (blue x's) to $\sqrt{N}$ models confirming the collective nature of the strong coupling.

using two separate model functions. For the LP state we used a conventional Lorentzian shape possessing a constant width, $\Gamma$. In contrast, we fit the UP peaks using a Lorentzian possessing a phenomenologically asymmetric shape[76], which we write as,

$$I(\omega) = \frac{I_0}{[\omega - \omega_{UP}]^2 + [\Gamma_{UP}(\omega)]^2}, \tag{2.2}$$

where $\Gamma_{UP}(\omega) = 2\Gamma_{UP}/\{1 + \exp[a(\omega - \omega_{UP})]\}$ captures the asymmetry of the lineshape through the value of $a$ for a constant $\Gamma_{UP}$. Similar features appear in the absorption spectra of cavity polaritons formed from III-V semiconductor quantum wells and were shown to stem from the dispersive nature of exciton-exciton scattering in those systems caused by the finite effective mass of the exciton's constituent charges[77]. In the case of our samples, we believe the asymmetric lineshapes stem from the dispersive density of states into which the UP decays non-radiatively following excitation. Given that we observe the

most prominent asymmetries for the largest chromophore concentrations, we believe the overlap of the UP state with the 0-1 vibronic transition of each molecule causes a portion of the asymmetry. However, the introduction of additional relaxation channels at higher chromophore concentrations can also cause similar effects and affect the UP transmission lineshape[78], as we discuss below.

Previous studies consider the effect of strong light-molecule coupling on the shapes of spectra emitted by cavity polaritons following localization into the reservoir of dark exciton states. In particular, Mony *et al.* use the independence of the light emission lifetime of cavity polariton samples formed from perylene derivatives to propose most radiative relaxation stems from those cavity-embedded molecules decoupled from the cavity's photons[79]. However, many other studies stemming from fundamental treatments of the cavity photon-molecule interaction, like those we cite above, show the transmission, reflection, and absorption spectra of cavity polariton retain information on the coherent nature of the polariton states, which includes their lifetimes.

Table 2.3 compares the parameters we extract from fitting the peaks in Figure 2.4 to the shapes we detail above. One can ascertain several features of the dynamics of polaritons formed from each molecule directly from this comparison. First, cavity polaritons formed from CuTPP possess systematically broader peaks we assign to the LP state. This trend mirrors our observation that the peak corresponding to the Soret resonance of solvated CuTPP molecules is nearly 50% wider than that of ZnTPP and likely stems from the broader width of the Soret peak in the absorption spectrum of CuTPP relative to that of ZnTPP shown in Figure 2.1 and reported in Table 2.1, as we discuss in more detail below. Second, we find the width of the UP state becomes significantly larger as we increase the

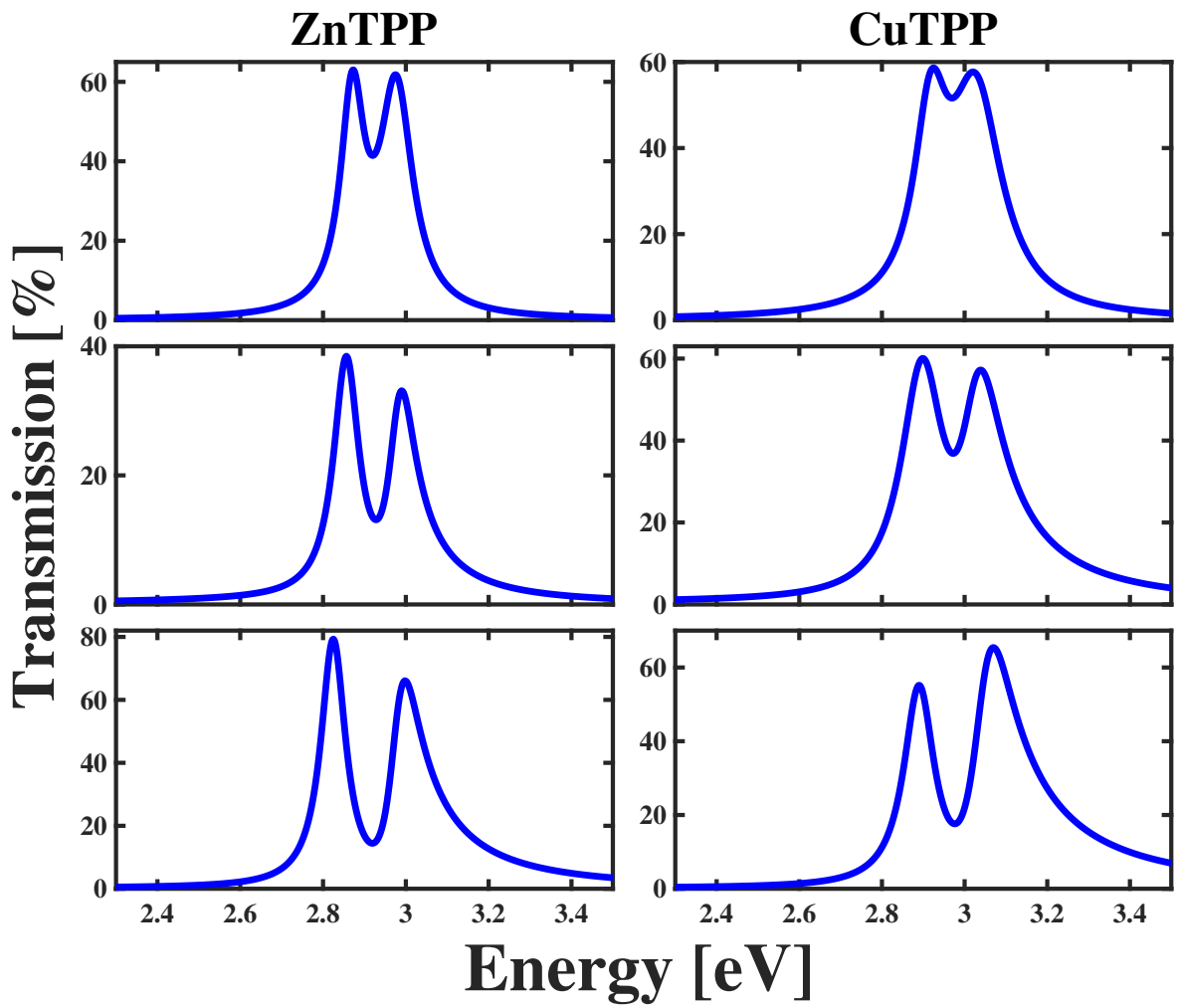


Figure 2.4: Comparison between the cavity polariton transmission spectra of samples formed from ZnTPP (left column of panels) to those formed from CuTPP (right column of panels) for the following chromophore concentrations in precursor polymer solutions: ∼0.5 mM (top panels), ∼1 mM (middle panels), ∼2 mM (bottom panels). We extract spectra following the fitting routine detailed in Methods.

concentration of either molecule within the cavities. This increase in peak width with increased concentration occurs simultaneously with our need to increase the asymmetry of the UP peak, as indicated by the value of the asymmetry parameter, $a$.

The values of the UP state energies at the highest intracavity concentration of each chromophore found from our fits to the peak shapes using the phenomenological model detailed above differ from values we find from simply identifying the peak position by

Table 2.3: Quantitative comparison between the energies and widths of cavity polaritons formed from the stated concentrations of ZnTPP and CuTPP in cavity structures prepared using the procedures detailed in Methods.

| **Chromophore** | **Conc. [mM]** | $\hbar\omega_{LP}$ **[eV]** | $\Gamma_{LP}$ **[ps$^{-1}$]** | Asym. Factor | $\hbar\omega_{UP}$ **[eV]** | $\Gamma_{UP}$ **[ps$^{-1}$]** |
|---|---|---|---|---|---|---|
| ZnTPP | 0.498 | 2.871±0.001 | 8.61±0.4 | 0 | 2.977±0.001 | 11.7±0.3 |
| | 0.996 | 2.856±0.001 | 9.12±0.1 | 29.64 | 2.915±0.002 | 68.4±4.6 |
| | 1.991 | 2.825±0.001 | 8.80±0.1 | 29.11 | 2.872±0.015 | 328±63 |
| CuTPP | 0.499 | 2.918±0.001 | 11.7±0.3 | 0.015 | 3.027 | 18.5 |
| | 0.988 | 2.898±0.001 | 19.9±0.4 | 20.38 | 2.911±0.016 | 160±63 |
| | 1.966 | 2.877±0.001 | 10.3±0.1 | 24.82 | 2.895±0.006 | 631±114 |

hand, as done in most studies. While there exists no fundamental understanding of this discrepancy currently, we point out fundamental theoretical treatments of vibrational anharmonicity do predict asymmetric peak shapes in vibrational spectra coincide with shifts in the apparent peak positions[80–83]. In the case of vibrational spectra, these coupled features of the peak characteristics stem from the presence of a dispersive density of states into which vibrational excitations can decay. This analogy to vibrational spectra may suggest the presence of a dispersive density of states into which the UP can decay when the energy of this state becomes pushed to higher and higher values through stronger and stronger coupling between cavity photons and the intracavity molecular chromophores. However, we do not investigate this facet of the polaritons in the current study.

The changes of peak shapes in steady-state polariton transmission spectra indicate the relaxation dynamics of metalloporphyrin cavity polaritons depend sensitively on the value of $\hbar\Omega$. To investigate this possibility, we undertook ultrafast transient spectroscopic studies of the ZnTPP and CuTPP cavity polariton samples whose steady-state spectra we show in Figures 2.2 and 2.4.

Figure 2.5 shows the comparison between the ultrafast transient absorption signals we measure at 1.97 eV for the 3 ZnTPP samples and at 2.64 eV for the 3 CuTPP samples whose

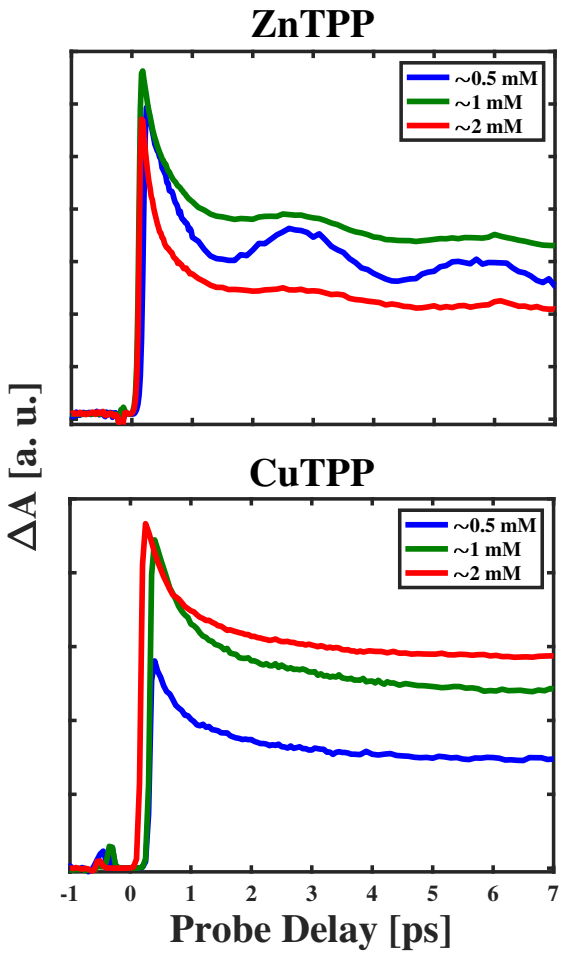


Figure 2.5: Comparison of the ultrafast transient absorption of cavity polariton samples formed from precursor polymer solutions containing ∼0.5 mM (blue), ∼1 mM (green), and ∼2 mM (red) of ZnTPP (top panel) and CuTPP (bottom panel) following 3.1 eV excitation. We probe ZnTPP and CuTPP cavity polariton samples at 1.97±0.015 eV and 2.64±0.015 eV, respectively.

steady-state transmission spectra are shown in Figure 2.5. We use a mutli-exponential model to extract the relaxation dynamics of each sample. In addition, we use an exponentially decaying sinusoidal function to extract the decay dynamics of each ZnTPP cavity polariton sample. The sinusoid stems from our excitation of coherent acoustic phonons in the Al thin film mirror whose evolution modulates both the transmission and absorption of the probe pulse. The first two decay rates we find from this analysis are shown in Table

2.4 as functions of chromophore concentration in the polymer precursor solutions.

The comparison in Figure 2.5 shows that the rate of the initial decay process in our ZnTPP samples increases as we increase the concentration of this molecular species in our polariton samples, as we have reported previously[4]. This increase in the initial decay rate coincides with the increased width of the peak we assign to the UP state in that steady-state transmission measurements shown in Figure 2.4. In addition, we find the overall behavior of the transient absorption signal of the ZnTPP cavity polaritons resembles that of solvated molecules reported by Zewail and our group previously[4,62]. In contrast, our analysis indicates the ultrafast localization dynamics of cavity polaritons formed from CuTPP do not change systematically as we change the concentration of this chromophore in our cavity structures.

For all three CuTPP cavity polariton samples we consider in this study we find an initial decay rate on the order of 1.3 $ps^{-1}$. Furthermore, we find the overall behavior of the transient absorption signal of the CuTPP polaritons does not resemble that of solvated molecules reported previously. While the relaxation of solvated molecules into the triplet states of CuTPP manifests itself as a $\sim$4.3 $ps^{-1}$ rise in the TA signal at 2.64 eV, we find TA signal for all the cavity polariton samples appears as an initial spike followed by a decay. The difference in the appearance of the TA signal from the CuTPP polaritons relative to solvated samples can be attributed to the significant increase in nonlinear interactions between the pump and probe pulses we anticipate to occur when these beams interact with the cavity polaritons[31]. However, this difference in the behavior of the TA signals complicates assignment of the states participating in polariton relaxation and necessitates further spectroscopic investigation to better understand from which mechanism the differ-

Table 2.4: Quantitative comparison between the decay rates of cavity polariton signals following a 3.1 eV pump pulse probed at 1.970±0.015 eV for samples formed from ZnTPP and at 2.64±0.015 eV for samples formed from CuTPP. We report these values for three different chromophore concentrations in precursor solutions made before cavity fabrication.

| **Chromophore** | **Conc. [mM]** | $k_1$ [ps$^{-1}$] | $k_2$ [ps$^{-1}$] |
|---|---|---|---|
| ZnTPP | 0.498 | 0.87±0.07 | 0.052±0.003 |
| | 0.996 | 1.28±0.07 | 0.051±0.004 |
| | 1.991 | 2.25±0.10 | 0.063±0.004 |
| CuTPP | 0.499 | 1.32±0.05 | 0.032±0.006 |
| | 0.988 | 1.22±0.05 | 0.014±0.003 |
| | 1.966 | 1.43±0.06 | 0.015±0.003 |

ence stems, as we discuss below.

Steady-state and ultrafast dynamical spectroscopic measurements suggest that cavity polaritons formed from ZnTPP differ fundamentally from those formed from CuTPP despite the fact that each organometallic molecule possesses the exact same organic ligand. To unravel how differences in the excited-state properties of each respective molecule imprint themselves on the dynamics of the cavity polaritons they form, we discuss the connections of the absorptive properties of ensembles of each molecular chromophore to the polariton spectra and possible mechanisms leading to polariton localization in each chromophore in separate sub-sections.

## 2.4 Connecting Molecular, Photonic, and Polaritonic Lineshapes and Lifetimes

The steady-state transmission spectra of Figure 2.4 indicate the cavity polaritons formed from ZnTPP and CuTPP differ on a fundamental level. As mentioned above and shown by several authors[29,84,85], strong coupling between the molecule and cavity photons imparts the photonic coherence onto the polariton states. However, the connection between

molecular and photonic broadening mechanisms to the widths of peaks in the steady-state spectra of polaritonic samples depends on the strength of the light-matter coupling. In the limit that $\hbar\Omega_R >> \Gamma_{inhom}$ and $\omega_{ph} = \omega_{ex}$, Houdré *et al.* show the width of both polariton peaks should be the geometric mean of the homogeneous widths of both the cavity photon and exciton peaks, i.e. $\Gamma_{pol} = (\Gamma_{ph} + \Gamma_{hom})/2$[29]. In contrast, when $\hbar\Omega_R \approx \Gamma_{inhom}$ the same authors demonstrate the polaritons peaks possess a width of $\Gamma_{pol} = (\Gamma_{ph} + \Gamma_{inhom})/2$. Using the values for $\Gamma_{ph}$ and $\Gamma_{inhom}$ and the fact our polaritons form in the limit that $\hbar\Omega_R \approx \Gamma_{inhom}$, we expect the peaks in the steady-state polariton spectra of ZnTPP and CuTPP should possess widths of 10.8$\pm$0.3 ps$^{-1}$ and 12.7$\pm$0.1 ps$^{-1}$, respectively. By comparing these values to those we report for the peak widths we find experimentally in Table 2.3, we find the model of Houdré *et al.* can qualitatively predict the widths of the LP peaks at all concentrations of ZnTPP, but cannot account for the significant broadening of the UP peaks for either chromophore we measure as we increase their concentrations in the polariton samples. We note for the reader that while Houdré *et al.* developed their treatment to explain the steady-state spectra of cavity polaritons formed from III-V semiconductor quantum wells, the equations stated above only necessitate the presence of an intracavity layer whose optical properties can be treated by a Lorentzian model, which can phenomenologically account for the dielectric properties of an ensemble of chromophores embedded with polymer layers like those we use to form our own cavity polariton samples.

The deviations between standard theories of polariton steady-state spectra and our measured results may result from changes in the ultrafast relaxation dynamics of metalloporphyrin cavity polaritons as we increase $\hbar\Omega_R$. Since strong light-matter coupling imparts the photonic coherence onto the polariton states, we expect one can infer the po-

lariton lifetime, $\tau_{pol}$, directly from the width of the polariton peaks[85]. In the absence of new relaxation channels caused by polariton formation, we propose $\tau_{pol}$ will be $1/\Gamma_{pol} = 2/(\Gamma_{ph} + \Gamma_{inhom})$, as described above. However, when additional relaxation channels become active through polariton formation, the decay of the polariton states can increase beyond this simple superposition of weighted rates stemming from photonic and excitonic losses.

For example, in their early work on cavity polaritons formed from resonator-confined III-V semiconductor quantum wells, Tassone *et al.* found polariton formation created new channels through which the UP state could relax into the LP state directly through phonon scattering events[78]. These workers predicted the presence of resonant coupling between the polariton states not only increased the UP to LP relaxation rate by almost a factor of 10, but also led to significant asymmetries between the relaxation rates of the UP and LP states. This asymmetry results from the fact that very few states lie below the LP state into which it can relax. These predictions indicate polariton formation can drive new types of relaxation processes that will affect polariton state lifetimes and should manifest themselves in the widths of polariton transmission peaks directly.

While Ref. 41 considers cavity polaritons formed from the excitons of nano-fabricated quantum wells of inorganic semi-conductors, we believe these interpolaritonic relaxation channels should be even more important in the dynamics of cavity polaritons formed from molecular chromophores since the localized molecular vibrations play no role in the conservation of polariton momentum. This lack of a role in momentum conservation implies the selection rules for vibrational transitions will be less strict in cavity polaritons formed from an isotropic sample of uncoupled molecules than inorganic systems whose electronic

excitations possess well-defined momentum in these materials' Brillioun zones. This presumption conforms with more recent results from 2-dimensional electronic spectroscopic studies of the dynamics of cavity polariton samples formed from aggregates of a cynanine dye, which show UP population relaxes to the LP state via an interpolaritonic relaxation channel with the same efficiency as localization into the dark states (DS)[86].

Under these conditions we expect the total polaritonic decay rate becomes $\Gamma_{LP,UP} = |X_{ph}|^2\Gamma_{ph} + |X_{ex}|^2\Gamma_{inhom} + \Gamma_{pol}$, where $\Gamma_{pol}$ represents the relaxation rate stemming from processes like phonon-mediated interpolaritonic scattering considered by Tassone *et al*. By determining $\Gamma_{ph}$ and $\Gamma_{inhom}$ from model calculations and steady-state absorption measurements in the solution phase, one can then subtract these values from the total width of the Lorentzian peak in the polariton transmission spectrum to estimate $\Gamma_{pol}$. This approach provides a means to constrain unknown rates in the complex relaxation dynamics of strongly coupled molecules and better understand the overall dynamics of metalloporphyrin cavity polaritons, which we use below.

## 2.5 ZnTPP Cavity Polariton Localization Dynamics

To help determine the mechanism by which the rate of polaritons relax into the localized states of cavity-embedded ZnTPP molecules changes as a function of $\hbar\Omega_R$, we modeled the dynamics of the state populations most likely to contribute to the results we found experimentally. Figure 2.6 shows the excited states involved and the defines the different rates of relaxation between them. Using these definitions, we find the populations obey

the following rate equations,

$$\frac{dN_Q}{dt} = \Gamma_{IC}^{LP} N_{LP} + \Gamma_{IC}^{DS} N_{DS}, \tag{2.3a}$$

$$\frac{dN_{LP}}{dt} = G_{LP}(\mathrm{t}) + \Gamma_{LP}^{DS} N_{DS} + \Gamma_{UP}^{UP} N_{UP} - \left[\Gamma_{IC}^{LP} + \alpha\Gamma_{ph}^{LP}\right] N_{LP}, \tag{2.3b}$$

$$\frac{dN_{DS}}{dt} = G_{DS}(\mathrm{t}) + \Gamma_{DS} N_{UP} - \left[\Gamma_{IC}^{DS} + \Gamma_{LP}^{DS}\right] N_{DS}, \tag{2.3c}$$

$$\frac{dN_{UP}}{dt} = G_{UP}(\mathrm{t}) - \left[\Gamma_{DS} + \Gamma_{LP}^{UP} + \alpha\Gamma_{ph}^{UP}\right] N_{UP}, \tag{2.3d}$$

where the factors $G_i$(t) correspond to photoexcitation of the ith state of the model by a 100 fs-wide Gaussian pulse weighted by the probability different states will absorb the pump pulse. In this model we neglect the radiative and non-radiative decay rates of the Q state since the time constant corresponding to these rates is at least $10^2$ longer than the temporal window we consider experimentally in Figure 2.4. The term $\alpha$ represents the square of the Hopfield coefficient characterizing the photonic contribution to each polaritonic state[87], $|X_{ph}|^2$, which we set to 0.5 given our undertaking the ultrafast measurements at resonant cavity-molecule conditions.

Previous studies use similar, simple rate equations to model the dynamics of polaritonic systems and determine how population flows from the UP states into its lower lying counterparts[34,88,89]. In particular, we use the approach of Tassone *et al.* and explicitly consider a possible role for the direct relaxation between the UP and LP states[78], as described above. Since we know the total decay rate of the UP state imprints itself on the width of corresponding peak in the steady-state transmission spectrum, we justify our consideration of a direct interpolaritonic decay channel by noting the width of the UP peak in Figure

2.4 increases significantly and becomes very asymmetric as we increase the concentration of cavity-embedded ZnTPP molecules. Furthermore, we expect only small changes in the polariton decay rates due to photonic losses and the localization rate $\Gamma_{DS}$, which should increase as dictated by the associated increase in the density of dark states caused by the additional chromophores we embed in each cavity structure.

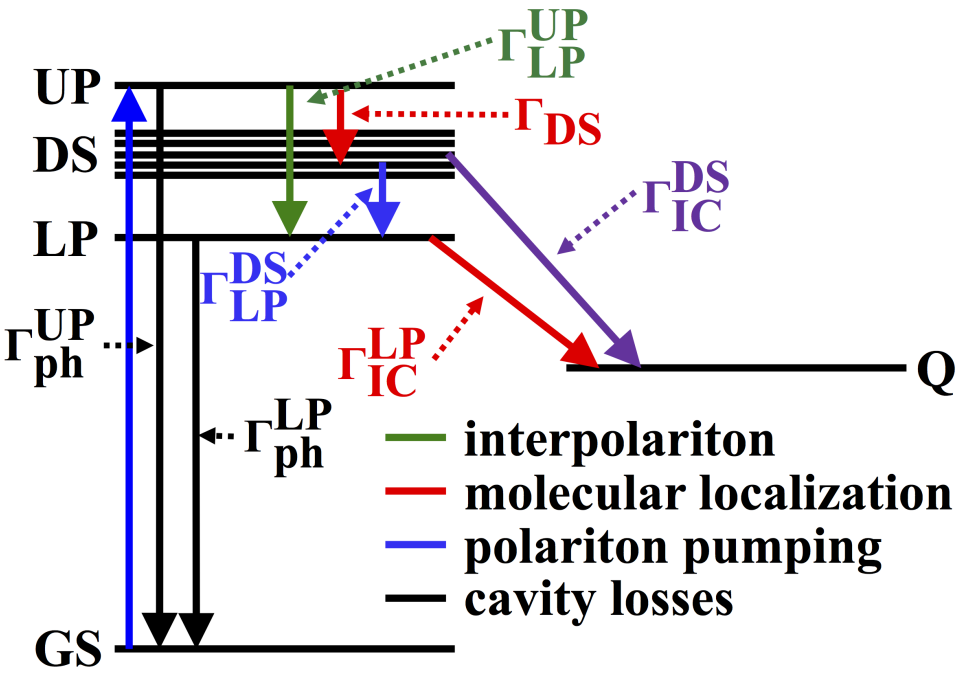


Figure 2.6: Schematic representation of the states and relaxation rates pertinent to model the dynamics of ZnTPP cavity polaritons shown in Figure 2.4. GS is the global ground state, UP is the upper polariton, LP is the lower polariton, DS are the B states of localized ZnTPP molecules uncoupled from cavity photons, Q is the $S_1$ state of localized ZnTPP molecules within the cavity structure, $\Gamma_{ph}^{UP}$ is the photonic loss from the UP state, $\Gamma_{ph}^{LP}$ is the photonic loss from the LP state, $\Gamma_{LP}^{UP}$ is the relaxation rate from UP to LP, $\Gamma_{DS}$ is the relaxation rate from UP to DS, $\Gamma_{LP}^{DS}$ is the relaxation rate from DS to LP, $\Gamma_{IC}^{DS}$ is the internal conversion rate from DS to Q, and $\Gamma_{IC}^{LP}$ is the internal conversion rate from LP to Q.

In addition, we use our proposed relations between the polariton decay rates and those of the cavity photons and molecular excitons to estimate $\Gamma_{IC}^{LP}$. Specifically, we equate $\Gamma_{LP} = |X_{ph}|^2\Gamma_{ph} + |X_{ex}|^2\Gamma_{inhom} = |X_{ph}|^2\Gamma_{ph} + \Gamma_{IC}^{LP}$, which allows us to estimate $\Gamma_{IC}^{LP} =$

$\Gamma_{LP} - |X_{ph}|^2\Gamma_{ph}$ using the values of $\Gamma_{LP}$ we measure experimentally and $\Gamma_{ph}$ we find from our transfer matrix model calculations.

While we can accurately estimate the values of $\Gamma_{IC}^{DS}$, $\Gamma_{ph}^{UP}$, $\Gamma_{ph}^{LP}$, and $\Gamma_{IC}^{LP}$ in Eqs. 2.3a-2.3b from Table 2.3, we must motivate values of the remaining rate constants from calculations that depend on the value of $\hbar\Omega_R$ we estimate from the spectra in Figure 2.4. Specifically, we computed the potential energy surfaces (PESs) of the UP and LP along a 1330 cm$^{-1}$ vibrational mode. While our previous analysis suggests the B state of ZnTPP reorganizes along a vibrational mode near 1190 cm$^{-1}$, which we show as an inset in Figure 2.1, Raman spectroscopy studies undertaken in resonance with the Soret transitions of other metalloporphyrins find substantial activity of totally symmetric ring stretching modes in the region between 1300 cm$^{-1}$ and 1550 cm$^{-1}$ [90,91]. These studies indicate the B states of these molecules also reorganize along such modes. Furthermore, our DFT calculations predict the most intense Raman active vibration of ZnTPP corresponds to a totally symmetric ring distortion mode whose harmonic frequency we find at 1400 cm$^{-1}$ [5]. After multiplying by established anharmonic factors, we find this harmonic frequency shifts to nearly 1330 cm$^{-1}$. By varying $\hbar\Omega_R$ in the computation of the polaritonic PESs, we find specific values of the vacuum Rabi splitting energy drive resonances between vibrational sub-levels on different polaritonic PESs. In particular, by changing $\hbar\Omega_R$ from 75 meV to 110 meV to 160 meV we reduce the energy gap between the $\nu = 0$ sub-level of the UP state and the $\nu' = 1$ sub-level of the LP state when we consider PESs along the 1330 cm$^{-1}$ mode, as shown in the panels of Figure 2.7. Previously, we proposed similar resonances cause interference in the Raman scattering excitation spectra of molecular cavity polaritons [5].

Given the dependence of the transition probability on the energy gap between the

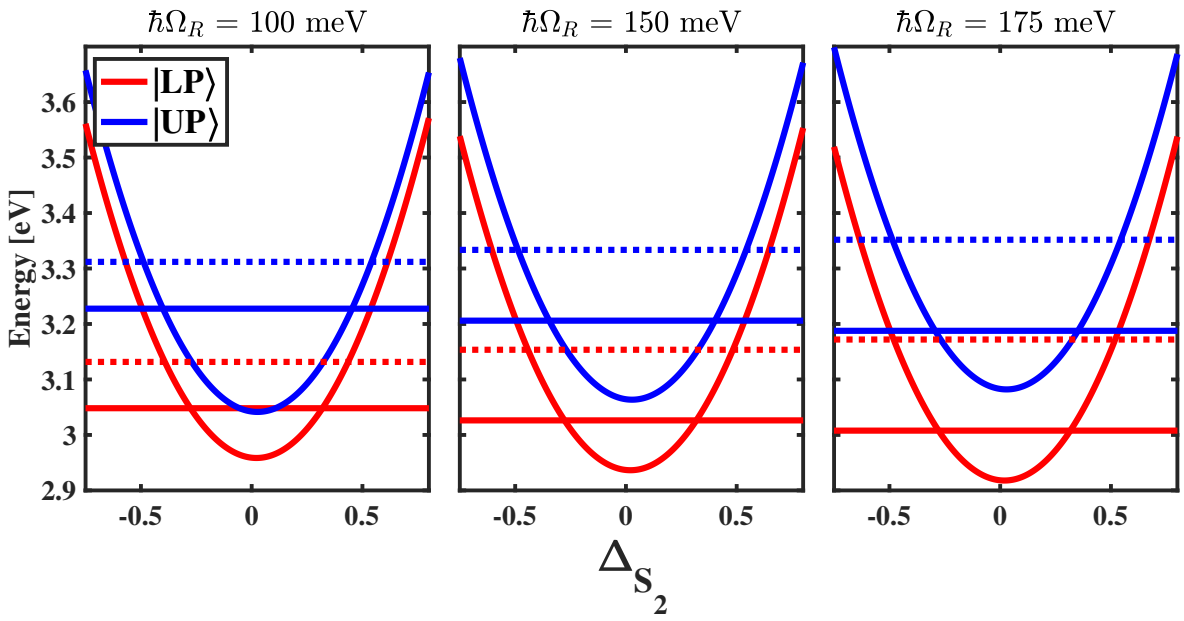


Figure 2.7: Comparison between the harmonic potential energy surfaces of the upper (blue) and lower (red) polariton states along a 1330 $cm^{-1}$ reorganization mode for vacuum Rabi splitting energy values of 75 meV (left panel), 110 meV (middle panel), and 160 meV (right panel). The $\nu = 0$ and $\nu = 1$ vibrational states on each PES are shown as solid and dashed lines, respectively.

states involved in the transition, we use a simple time-dependent perturbation calculation to conservatively estimate how much the probability of making a non-radiative transition from the UP to LP, $P_{UP\rightarrow LP}$, changes as a function of polariton vibronic resonance conditions we depict in the panels of Figure 2.7. Given the finite lifetime of the UP due to decay to the DS and free space photons, we expect $P_{UP\rightarrow LP} \propto |c_{LP}|^2$ where,

$$c_{LP} = \frac{\imath}{\hbar}\int_0^t dt' V_{UP\nu,LP\nu'} \mathrm{e}^{[\imath(\omega_{LP\nu'}-\omega_{UP\nu})t']} \mathrm{e}^{(-\Gamma_{UP}t')}, \tag{2.4}$$

the interaction matrix is,

$$V_{UP\nu,LP\nu'} = \hbar^2 \mathrm{J}_{UP,LP} \int dq \chi^*_{UP\nu}(q) \frac{\partial}{\partial q} \chi_{LP\nu'}(q), \tag{2.5}$$

for an interpolaritonic coupling $J_{UP,LP}$ caused by the kinetic energy of the molecule's nuclei as defined by Bixon and Jortner[92], and $\Gamma_{UP}$ is the sum of the rates of population loss from the UP caused by photonic decay and localization into the dark states, which we assume is $\sim$11.2 ps$^{-1}$ based on the width we find in the polariton transmission spectra and detail in Table 2.3 for the 0.498 mM ZnTPP polariton sample. We presume the UP$\rightarrow$LP relaxation process adds a factor of 0.5 ps$^{-1}$ to the overall decay rate to produce the 11.7 ps$^{-1}$ rate we report in Table 2.3. Furthermore, we presume the normal coordinate $q$ corresponds to the 1330 cm$^{-1}$ vibrational mode along which we calculate the polaritonic PESs. More elaborate theoretical descriptions of the coupling between the polaritonic states may better estimate the value of these interactions[50], but are beyond our capabilities currently.

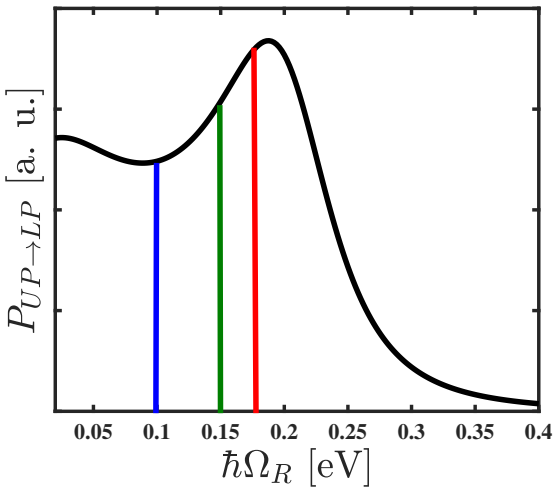


Figure 2.8: The dependence of the probability of making a non-radiative transition between the upper and lower polaritons due to the interactions caused by the nuclear momentum on the vacuum Rabi splitting energy, $\hbar\Omega_R$, between the polaritonic potential energy surfaces. Vertical blue, green, and red lines correspond to the values of $\hbar\Omega_R$ used to assess the PES in Figure 2.7 and qualitatively resemble the values observed experimentally.

Figure 2.8 shows how $P_{UP\rightarrow LP}$ depends on the value of the Rabi splitting energy separating the manifold of states in each respective polaritonic state. In Figure 2.8, we show

Table 2.5: Comparison between the values of $\hbar\Omega_R$ found from models of the dispersion of ZnTPP cavity polaritons to the energies and intensities of local molecular vibrations found from DFT calculations.

| **Chromophore** | **Conc. [mM]** | $\hbar\Omega_R$ [meV] | $\hbar\omega_\nu^{(1)}$ [meV] | $I^{(1)}$ [a. u.] | $\hbar\omega_\nu^{(1/2)}$ [meV] | $I^{(1/2)}$ [a. u.] |
|---|---|---|---|---|---|---|
| ZnTPP | 0.498 | 77 | 79 | 10.14 | 40 | 2.1 |
| | 0.996 | 108 | 107 | 51.6 | 56 | 0.4 |
| | 1.991 | 160 | 165 | 1371 | 81 | 71.7 |

the values of $\hbar\Omega_R$ used to form the PESs in Figure 2.7 as color-coded, vertical lines. Inspecting Figure 2.8, we find two important facets of the calculated transition probability. First, we find relatively large transition probabilities for small values of $\hbar\Omega_R$. At these small vacuum Rabi splitting energies the two polaritons states remain in close energetic proximity and can more easily couple to one another, as expected from previous theoretical treatments of the non-radiative polaritonic relaxation rate[93]. In addition, one anticipates a lower density of dark states for these values of $\hbar\Omega_R$, which would reduce the magnitude of $\Gamma_{DS}$ in these molecule-cavity systems. As a second point of importance shown in Figure 2.8, we highlight the increase in $P_{UP\rightarrow LP}$ as $\hbar\Omega_R$ approaches the energy of the vibrational mode along which the polaritons reorganize. We find the probability at these vacuum Rabi splitting energies nearly doubles relative to the small values of $\hbar\Omega_R$. This finding can also help explain the substantial broadening of the peak corresponding to the UP state in the transmission spectra of Figure 2.4 for the largest concentration of ZnTPP we consider. In the presence of an increasing interpolaritonic relaxation rate, the width of the transmission peak should also increase due to the lifetime broadening caused by the introduction of an additional channel through which the UP state can decay. We use these qualitative trends in the transition probability to estimate the dependence of the interpolaritonic rate $\Gamma_{LP}^{UP}$ on the intracavity ZnTPP concentration.

While we observe a vibronic overtone in the absorption spectrum of ZnTPP we assign to structural re-organization of this molecule's B state along the normal coordinate corresponding to a totally symmetric vibration at 1190 $cm^{-1}$, there is no fundamental reason this vibration should dominate the non-radiative relaxation of the UP state in strongly coupled photon-ZnTPP samples. As shown by Eq. (2.5), we expect those vibrational modes most able to couple the UP and LP via the constant $J_{UP,LP}$, to dominate the non-radiative relaxation, which will correspond to the vibrations possessing the largest Raman intensity. The results of Somaschi *et al.* support this physical picture[88]. In their study, these authors find resonance conditions between the DS reservoir and vibronically excited sub-levels of the LP state induce large rates of incoherent pumping of the polariton state following resonant excitation of bare excitons. However, one only observes these enhanced pumping rates when the detuning of the cavity photon energy from that of the molecular exciton transition matched the frequency of intense peaks in the vibrational Raman spectrum of the molecule of interest.

To further motivate the manner in which we expect the quantitative values of non-radiative decay rates to vary with changes to the collective vacuum Rabi splitting energy, we consider the intensity of Raman-active vibrations found from our DFT calculations whose energies lie close to both $\hbar\Omega_R$ and $\hbar\Omega_R/2$ for each ZnTPP cavity polariton, as we compare in Table 2.5. These comparisons reveal two important implications for understanding the ultrafast dynamics of ZnTPP cavity polaritons. First, since the 1330 $cm^{-1}$ (165 meV) vibration possesses such a dramatically larger intensity than the vibrations maintaining interpolaritonic resonances in lower concentration polariton samples, we expect the 1330 $cm^{-1}$ mode will dominate the non-radiative relaxation of the UP state in all

the samples, as we discussed above.

Second, not only do we expect vibrational resonances to enhance a coupling between the UP and LP states as we increase the value of $\hbar\Omega_R$ near 160 meV, but we also anticipate enhancement of the relaxation rates $\Gamma_{DS}$ and $\Gamma_{LP}^{DS}$. This anticipation stems from the fact that we drive a resonance between the UP state and DS reservoir and a resonance between the DS reservoir and the LP state along a Raman-active vibration possessing a scaled energy of 81 meV whose intensity is an order of magnitude larger than those of the vibrations that maintain similar resonances for $\hbar\Omega_R$ values of 77 meV and 108 meV. The large increase in the Raman activity of the vibration capable of mediating a resonant relaxation channel between the relevant states of increasingly strongly coupled ZnTPP cavity polariton samples indicates those relaxation processes should also become progressively more probable as we increase $\hbar\Omega_R$.

We propose to understand the role of interpolaritonic conversion on the localization of strongly cavity-coupled ZnTPP molecules into their Q states by modeling the dynamics of the excited state populations shown in Figure 2.5 using solutions to Eq. (2.3) with rates estimated from the following equations,

$$\Gamma_{UP} = \alpha\Gamma_{ph}^{UP} + \alpha\Gamma_{ZnTPP} + \Gamma_{DS} + \Gamma_{LP}^{UP}, \tag{2.6a}$$

$$\Gamma_{LP} = \alpha\Gamma_{ph}^{UP} + \alpha\Gamma_{ZnTPP} + k_{IC}^{LP}, \tag{2.6b}$$

where we set $\alpha$ = 0.5. We find the rate $\Gamma_{IC}^{LP}$ by quantifying the rate $\Gamma_{ph}^{LP}$ from Table 2.1 and $\Gamma_{IC}^{DS}$ from experimental solution phase transient absorption signal of ZnTPP and sub-

tracted these rates from the overall width of the LP peak in each steady-state spectrum of the ZnTPP cavity polaritons shown in the lefthand panels of Figure 2.4. Furthermore, we estimate the rates $\Gamma_{DS}$ and $\Gamma_{LP}^{UP}$ by subtracting the rate $\Gamma_{ph}^{UP}$ in Table 2.1 and $\Gamma_{IC}^{DS}$ established by modeling the resonator structure and measuring the solution phase transient absorption signal of ZnTPP, respectively, and subtracting these rates from the overall width of the UP peaks. Moreover, we estimated the rate $\Gamma_{LP}^{DS}$ from previous experimental studies of ultrafast polariton dynamics.[34] Based on the values we report in Table 2.5 for vibrations mostly likely to participate in the non-radiative relaxation of ZnTPP cavity polaritons, we propose the rates $\Gamma_{LP}^{UP}$, $\Gamma_{DS}$, and $\Gamma_{LP}^{DS}$ will increase by factors of 2 and 10 as we increase $\hbar\Omega_R$ from 77 meV to 110 meV and 160 meV, respectively. While one cannot use these values to quantitatively reproduce $\Gamma_{UP}$ for the two more concentrated samples reported in Table 2.3, they provide conservative estimate to enable our probing how the probability of these dynamical processes impacts the overall localization rate. To estimate a total conversion rate, we invert the time at which the Q state population reaches $1 - \exp(-1)$ of the initial population excited into the UP state, $N_{UP}(0)$. We report the values of each rate used in the model defined by Eq. (2.3) in Table 2.6. We mark those values we found from our experiments with an asterisk in Table 2.6.

The panels of Figure 2.9 shows the results of the model simulations using these parameters. We use $N_{UP}(0)$ values of 1, 4, and 9 for the dynamical simulations of the $\hbar\Omega_R$ values of 77 meV, 110 meV, and 160 meV, respectively. Using these models we find as we increase ZnTPP concentration, we observe a corresponding increase in the localization rate of the Q state population. Quantitatively, we find $\Gamma_{IC}$ increases from 0.87 ps$^{-1}$ to 1.20 ps$^{-1}$ to 2.34 ps$^{-1}$ as we increase [ZnTPP] from 0.5 mM to 1 mM to 2 mM, respectively. These

Table 2.6: Relaxation rates of pertinent decay channels in a ZnTPP cavity polariton at Rabi splitting energies of 70, 110, and 160 meV. All model parameters found from experimental measurements are denoted with an asterisk.

| rate [ps$^{-1}$]Conc. [mM] | 0.498 | 0.996 | 1.991 |
|---|---|---|---|
| $\Gamma_{LP}^{UP}$ | 0.5 | 1 | 5 |
| $\Gamma_{DS}$ | 5.3* | 10 | 50 |
| $\Gamma_{ph}^{UP}$ | 11.8* | 11.8* | 11.8* |
| $\Gamma_{IC}^{DS}$ | 0.67* | 0.67* | 0.67* |
| $\Gamma_{LP}^{DS}$ | 0.2 | 0.4 | 2 |
| $\Gamma_{IC}^{LP}$ | 2.71* | 3.22* | 2.90* |
| $\Gamma_{ph}^{LP}$ | 11.8* | 11.8* | 11.8* |

values agree qualitatively with the experimental results reported in Table 2.4. Deviations between the results of our model dynamics and the experimental kinetic traces shown in the top panel of Figure 2.5 stem from the coherent interaction between the pump and probe pulses, which make it impossible to resolve the polariton dynamics at the shortest pump-probe times.

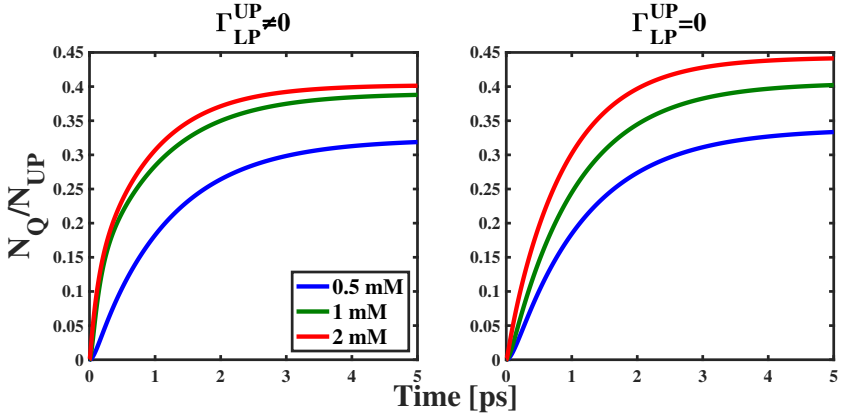


Figure 2.9: Left panel: ultrafast dynamics of the electronic population in the Q states of cavity-embedded ZnTPP molecules for interpolaritonic relaxation rates of $k_{LP}^{UP}$ = 0.5 ps$^{-1}$, 1.0 ps$^{-1}$, and 6 ps$^{-1}$ modeled to occur for polariton samples formed from 0.5 mM (blue), 1 mM (green), and 2 mM (red) ZnTPP precursor solutions using the decay rate values detailed in Table 2.4. Right panel: same ultrafast dynamics we model when $k_{LP}^{UP}$ = 0 ps$^{-1}$ for polariton samples formed from 0.5 mM (blue), 1 mM (green), and 2 mM (red) ZnTPP precursor solutions.

We also carried out model simulations in which we neglected the interpolaritonic re-

laxation channel for comparison to our experimental results, as shown in the right hand panel of Figure 2.9. In these cases, we left all the other model parameters unchanged. For those cases we find the total conversion rates become 0.81 ps$^{-1}$ to 0.95 ps$^{-1}$ to 1.25 ps$^{-1}$ as we increase [ZnTPP] from 0.498 mM to 0.996 mM to 1.991 mM, respectively. Unlike the case where we explicitly consider non-zero values of $\Gamma_{LP}^{UP}$ the values we find in the absence of the interpolaritonic relaxation channel do not agree with the rates we measure experimentally for the samples possessing the two largest values of the collective vacuum Rabi splitting energy.

In addition to changes in the dynamics of ZnTPP cavity parameters we expect to observe as a function of $\hbar\Omega_R$ stemming from the physical arguments we made above, we expect vibrationally mediated relaxation channels should depend sensitively on the relative detuning between the cavity photon and Soret transition of ZnTPP molecules, which can be controlled using the dispersion of the interpolaritonic energy shown in the panels of Figure 2.2. In the case that vibrationally mediated interpolaritonic relaxation depends on resonance conditions like those shown in Figure 2.7, we expect to observe an increase in the width of the UP state peak in the transmission spectrum of the ZnTPP cavity polariton sample for those incident angles of a probe light beam, $\theta_{inc}$, that force the dispersive interpolaritonic energy to match that of the 1330 cm$^{-1}$ vibration. Figure 2.10 shows we observe this behavior for the ZnTPP cavity polariton sample we formed from the 1.991 mM polymer precursor solution. We find UP widths nearly equal to the cavity photon lifetime for $\theta_{inc}$ values below 50°, but then observe a significant increase in $\Gamma_{UP}$ as we increase $\theta_{inc}$ towards those values at which the cavity photon energy matches that of the molecule's Soret transition. Further increasing $\theta_{inc}$ causes a decrease in $\Gamma_{UP}$ and results in a peak-like

shape to the overall dispersion of the UP decay rate. Given neither the cavity photon lifetime nor the inhomogeneous broadening of the exciton energies depend so sensitively on the value of $\theta_{inc}$, we propose the peak in the dispersion of $\Gamma_{UP}$ stems from changes in the values of the interpolaritonic relaxation rate as we change the energy difference between the LP and UP states with $\theta_{inc}$, which would conform with the qualitative features of the dependence of $P_{UP\rightarrow LP}$ on $\hbar\Omega_R$ shown in Figure 2.8.

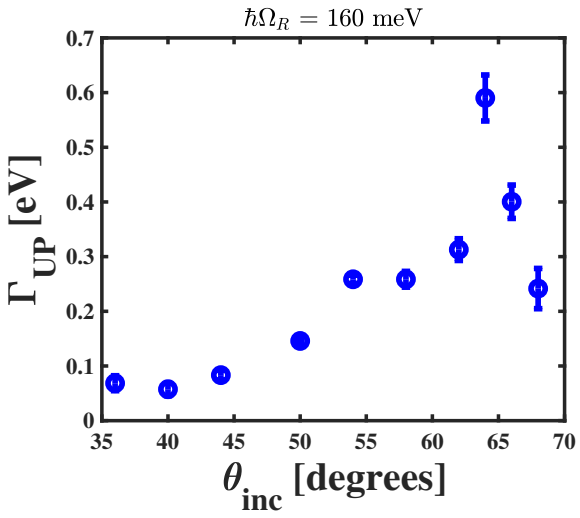


Figure 2.10: Dispersion of the UP peak width, $\Gamma_U P$, as a function of the incident angles of a probe light beam, $\theta_{inc}$, found using the phenomenological model described by Eq. (2.2)

## 2.6 CuTPP Cavity Polariton Localization Dynamics

While a kinetic model suggests increased collective coupling between ZnTPP and cavity photons creates new relaxation pathways capable of affecting the localization of polaritons onto individual molecules, the ultrafast TA results from our CuTPP cavity polariton samples suggest polariton formation fundamentally changes existing relaxation pathways. In particular, we find the initial decay imprinted onto our TA signals measured from three separate CuTPP polariton samples does not change substantially or systematically as we change the concentration of this chromophore within the cavity structures. We find inter-

nal conversion rates near 1.3 $ps^{-1}$ for all the samples. These decay rates are nearly half of that we find for CuTPP photo-excited at 400 nm when we solvate this chromophore in toluene. However, the appearance of the TA signal does change systematically relative to measurements done on solution-phase samples. This difference creates ambiguity in assigning those states participating in the ultrafast localization dynamics of polaritons formed from CuTPP.

To ameliorate this uncertainty, we measured the steady-state photoluminescence spectra of cavity polariton samples formed from CuTPP and control samples in which we maintain the same spin processing parameters and Al capping layer, but do not deposit a DBR structure on the fused silica substrate. A comparison of the PL spectra emitted by these samples should provide clear insights into only those excited-state processes affected by polariton formation while holding constant any effects that stem from loading chromophores into a solid, polymer matrix under ultra high vacuum (UHV) conditions.

Figure 2.11 shows the PL spectra from these samples possess two prominent features when we make the measurements at 80 K. First, we find a relatively smaller peak centered near 1.9 eV, which we assign as the fluorescence emitted by the $^2$Q state of CuTPP. Second, we find a significantly more intense feature near 1.6 eV, which we assign as the phosphorescence from the $^2T_1$ and $^4T_1$ states of localized CuTPP molecules, which have been characterized thoroughly in previous studies[94]. Analysis of these spectra shows the integrated intensity of the fluorescence signal doubles when we embed the CuTPP-doped polymer layer in the cavity and form polaritons relative to the non-cavity sample. The low temperature at which we undertake these measurements suggests the difference in the fluorescence signal does not stem from processes such as thermally activated delayed

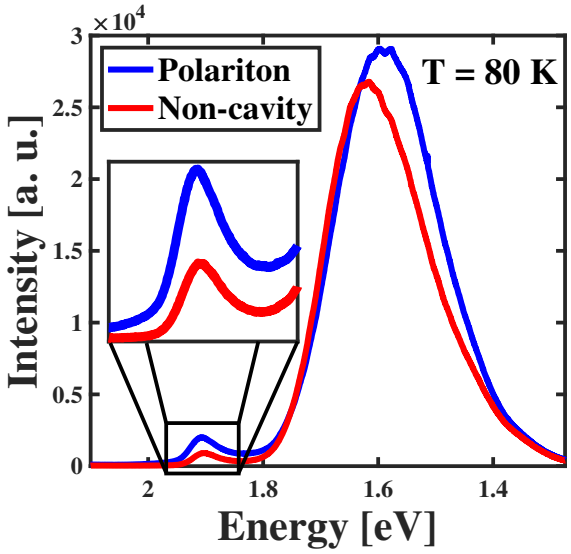


Figure 2.11: Comparison between the steady-state photoluminescence spectrum of CuTPP molecules strongly coupled to the photons of a Fabry-Pérot cavity formed from a ∼2 mM precursor solution (blue) to the same spectrum of CuTPP embedded in a metal-capped film formed in the absence of a cavity structure (red). Inset: close comparison between the fluorescence emitted by the Q states of CuTPP in each sample showing the factor of 2 increase in this signal we observe in the presence of strong cavity coupling.

fluorescence, which would need to overcome a 30 meV difference in energy manifest in the spacing between the features shown in Figure 2.11. Recent studies indicate thermally activated delayed fluorescence (TADF) can be enhanced by polariton formation[53].

While some previous studies have used comparisons of the optical power stored in resonators used to form cavity polaritons to the power incident on non-cavity samples to better quantify changes in the overall efficiency of light-mediated process[95], we do not believe such a treatment is necessary in the case of examining the PL efficiency of our CuTPP cavity polariton samples. In particular, we excite both our polariton and control samples at an energy significantly below that of the cavity photon mode. Furthermore, the ∼140 nm intracavity polymers drive formation of resonators incapable of sustaining standing modes at energies below 2.5 eV. The large gap between this energy and those

of the excitation or emission sources implies such photonic structures do not store energy from the incident laser or the radiating molecules.

Based on the fact that a factor of 2 increase in the fluorescence emitted by the Q state of CuTPP molecules strongly coupled to cavity photons coincides with our observations of an initial transient signal whose decay rate is nearly half of that we find for solution phase molecules, we propose cavity polariton formation causes an increase in the lifetime of the $^2$Q state in CuTPP. While the $^2$Q state does not directly couple to the cavity photons due to the fact that its resonant transition from the molecule's ground state lies nearly 0.6 eV below that of the Soret resonance, the complex interplay between nuclear and electronic structure in this chromophore could enable a novel mechanism to control the excited state dynamics of states not strongly coupled to the cavity photons.

Distortions to the PES of the CuTPP $^2$B excited state driven by polariton formation could explain at least two facets of our steady-state PL and TA measurements. First, changes to the position at which the molecular excited states achieve a minimum energy could reduce the ability of the central Cu atom to exchange its unshared $d$ electron with the surrounding porphyrin macrocycle. Since the $^2T_1$ and $^4T_1$ states of CuTPP split due to this exchange interaction, any changes to its value will manifest as shifts in the phosphorescence spectra of this chromophore. As seen in Figure 2.9, the phosphorescence of the cavity-coupled CuTPP sample appears at a lower energy than its non-cavity counterpart, which indicates a smaller energy splitting between the $^2T_1$ and $^4T_1$ states. Second, distortions to the excited state PESs of CuTPP would change the Franck-Condon factors central to the oscillator strengths of absorptive transitions of CuTPP excited states. The appearance of a prompt absorptive feature in the TA measurements may indicate the presence of newly allowed excited state

absorption transitions whose decay indicates relaxation of the polariton states into the $^2$Q states of localized CuTPP molecules. The ability polariton formation to affect excited state absorption processes has been proposed to affect the time-resolved spectroscopic signatures of vibrational polaritons[96], but there have been few experimental investigations of similar effects in molecular exciton cavity polaritons. We will need further work to decipher the mechanism explaining the differences in the TA signals of solvated and strongly cavity-coupled CuTPP molecules.

Establishing the role of polariton formation in amending the dynamics of molecular excited state not directly coupled to cavity photons necessitates further experimental investigation. In particular, since we propose distortions to those PESs involved in excited state reorganization drive the changes in excited state photophysics we observe, coherent vibrational spectroscopic techniques could be well suited to assess our proposals. In these approaches, one excites a coherent wavepacket using impulsive stimulated Raman processes and spectrally resolves the transmission or reflection of a probe pulse whose energy matches that of the polaritonic transitions[97–100]. One can then use known models to determine if the position at which the PES reaches it minimum energy changes as a function polariton formation and properties of the cavity mode such as resonant detuning and photon lifetime. We intend to undertake such measurements in future studies.

## 2.7 Conclusions

In this study, we examine ultrafast polariton localization into the excited states of cavity embedded metalloporphyrin molecules. Using a simple kinetic model, we find we can reproduce the change in the rate of polariton localization into the Q states of strongly

cavity-coupled ZnTPP molecules as a function of collective vacuum Rabi splitting energy found from experimental ultrafast pump-probe measurements. To achieve this qualitative agreement we find we need to introduce a direct channel of interpolaritonic relaxation neglected in the previous models of ultrafast polariton dynamics in $J$-aggregate systems. We justify this proposal using simple perturbation methods with vibrational energy states determined from models of polaritonic potential energy surfaces. These models suggest vibronic resonances between the polariton states could help interpolaritonic relaxation dynamics outcompete ultrafast relaxation into the band of states stemming from molecular chromophores decoupled from cavity photons. One could test this proposal by maintaining the same $\hbar\Omega_R$ values across several polariton samples in which isotopically different ZnTPP species strongly couple to the cavity photons. The differences in the isotopic substitution of different molecules would affect the energies of the vibrations along which the polaritons reorganize and cause changes to the resonance conditions necessary to induce ultrafast interpolaritonic relaxation prior to internal conversion to the Q state.

In addition, we find the structure of the ultrafast transient absorption signal we measure in resonance with the trip-doublet excited state absorption feature of CuTPP molecules changes qualitatively under strong light-matter conditions relative to the signals reported in solution-phase samples. By comparing the steady-state light emission spectra of CuTPP polariton and thin film control samples, we found the rate of internal conversion between the $^2$Q and manifold of trip-doublet states in CuTPP changes when an ensemble of this molecular species strongly couples to cavity photons. However, the changes to this non-radiative relaxation rate do not correlate with the value of $\hbar\Omega$ or the concentration of CuTPP we add to each cavity sample. These results indicate the complexity of molecular

electronic structure enables a mechanism through which cavity polariton formation affects the dynamics of molecular orbitals not coupled to the cavity photons directly. Overall, the results of this study indicate local molecular probes provide novel insights into the ultrafast dynamics of strongly coupled molecule-photon systems and allow researchers to more completely assess how polariton formation enables future photochemical and opto-electronic technologies.

# CHAPTER 3 LIGHT EMISSION FROM VIBRONIC POLARITONS IN COUPLED METALLOPORPHYRIN-MULTIMODE CAVITY SYSTEMS



## 3.1 Introduction

The strong coupling of molecular electrons and cavity photons leads to the formation of hybrid light-matter states known as cavity polaritons[2,49,101]. Several studies suggest cavity polariton formation enables control over processes ranging from singlet fission[50] and triplet harvesting[11] to the rates of non-radiative relaxation[4,102], including energy transfer[40,51], and certain photochemical reactions[44,45,103]. Despite growing interest in how polariton formation can leverage photonic coherence to create novel properties, there have been few studies examining how inherently molecular properties and processes affect states formed through strong light-matter coupling. The ability to control photonic coherence using molecular structure and dynamics would create additional means through which hybrid light-matter platforms could positively affect light harvesting, light emission, and energy transduction technologies. This ability would be prominent for highly symmetric molecules whose electronic structure is most susceptible to degeneracies that induce complex coupling between electrons and nuclear motions, i.e. vibrations.

For example, the significant interaction between degenerate electronic excited state configurations of porphyrin molecules drives the formation of B and Q excited singlet states whose energies split by $\sim$0.5 eV. Goutermann described the B and Q states as equally weighted symmetric and antisymmetric linear superpositions of the two configura-

tions $e_g(1)a_{1u}(1)$ and $e_g(1)a_{2u}(1)$, respectively[60]. Since the transitions between the ground state and each respective excited state configuration possess similar dipole moment magnitudes, one expects the B state would participate in a strongly allowed electronic transition while the intensity of the electronic transition involving the Q state would be negligible. This physical situation resembles that of $J$-aggregates where intermolecular coupling between two chromophores results in the formation of one bright aggregate state and one dark aggregate state[104]. While dozens of studies find the appearance of a prominent Soret peak corresponding to an electronic transition between the ground and B states of metalloporphyrins, these studies also find a larger than expected $\alpha$ resonance corresponding to the transition between the ground and Q states of these molecules[91]. Given the large oscillator strengths of their Soret transitions near 400 nm, several studies examine cavity polariton formation using metalloporphyrin molecules[4,59,61,102]. However, only few studies have considered how cavity polariton formation affects the Q states of these molecules[105].

## 3.2 Vibronic coupling mechanism

The appearance of a sizable $\alpha$ peak in the absorption spectra of metalloporphyrins stems from a non-Condon, vibronic coupling mechanism between the B and Q states of these molecules, which accounts for their optical properties, including resonance Raman excitation spectra[5,106]. This electronic coupling allows one to write out the wavefunction of the Q state as[107]

$$|Q\rangle = |Q\rangle_0 + \sum_i \frac{\langle i|\hat{V}_{HT}|Q\rangle_0}{E_i - E_Q}|i\rangle, \tag{3.1}$$

where $\hat{V}_{HT} = (\partial \hat{H}_{el}/\partial q)_0 q$ is the Herzberg-Teller (HT) coupling between states $|Q\rangle$ and $|i\rangle$ mediated by atomic motions along the normal coordinate $q$. $|Q\rangle_0$ represents the Q state in the equilibrium geometry of molecule's ground state. The dominance of this non-Condon vibronic coupling in the $\alpha$ transitions of metalloporphyrins manifests itself as significantly more intense 0-1 fluorescence signals than one observes for their 0-0 counterparts, which occurs due to the presence of $q$ in the interaction Hamiltonian matrix elements of Eq.(3.1)[62]. Many researchers propose these effects also drive visible light absorption and intermolecular energy transfer in natural and artificial photosynthetic systems based on chlorophyll[108–120]. Despite the important role this HT vibronic coupling process plays in controlling the optical properties of metalloporphyrins and its possible role in photosynthetic systems, it remains unclear how this coupling mechanism manifests itself under strong light-matter coupling within an optical cavity.

In this study, we examine theoretical and experimental assessments of vibronic coupling between the Q states of copper (II) tetraphenyl porphyrin (CuTPP) molecules and the polariton states formed by strongly coupling the Soret transitions of a disordered ensemble of this chromophore to photons in different cavity structures. CuTPP serves not only as an important model system for our study, but this molecule has been proposed as a unit in molecular assemblies useful for quantum information processing and computing[121]. Our theoretical predictions indicate the presence of feasible amounts of HT vibronic coupling can transfer the photonic contribution from the polariton states to the Q states of these molecules. Furthermore, we use a model of an energetically disordered ensemble of molecules to show the energy of this HT vibronic polariton always lies below those of dark states corresponding to molecules decoupled from the cavity photons. We test these theo-

retical predictions by measuring the light emission spectra of several different Fabry-Pérot cavity structures loaded with CuTPP molecules. Our experimental tests show at least two pieces of evidence that HT polaritons exist in these samples. First, we find the existence of a cavity mode located 1 vibrational quantum above the HT polariton energy enhances the light emission from the HT polariton state. Second, the enhanced light emission from the HT polariton state possesses an energy that disperses in the same way as a cavity photon mode. We propose this dispersive behavior results from the radiative relaxation of the HT polariton state into cavity photonic states dressed by collective molecular vibrations, which can only form through cavity polariton formation. Our results indicate the rich array of physical mechanisms through which researchers can use cavity polariton formation to control coherent and collective light-matter interactions.

We consider a HT-active molecule comprised of two excited electronic states, $|B\rangle$ and $|Q\rangle$, which couple via the interaction described by Eq. (3.1). We show this interaction schematically in the top right panel of Figure 3.1. We assume the higher energy of these two states, $|B\rangle$, interacts with cavity photons at a strength $V_{LM}$. We estimate the energetics of this system using a three-level Hamiltonian, which we write in matrix form as,

$$\hat{H} = \begin{bmatrix} \hbar\omega_B & V_{HT} & V_{LM} \\ V_{HT} & \hbar\omega_Q & 0 \\ V_{LM} & 0 & \hbar\omega_c \end{bmatrix}, \tag{3.2}$$

where the energies $\hbar\omega_B$, $\hbar\omega_Q$, and $\hbar\omega_c$ correspond to electronic states $|B\rangle$ and $|Q\rangle$ and the 1-photon cavity state, $|1\rangle_c$, respectively. We model the angular dependence of the cavity photon energy using the equation $\hbar\omega_c = E_{cutoff}\left[1 - \frac{sin^2(\theta)}{n_{eff}^2}\right]^{-1/2}$, where the cutoff

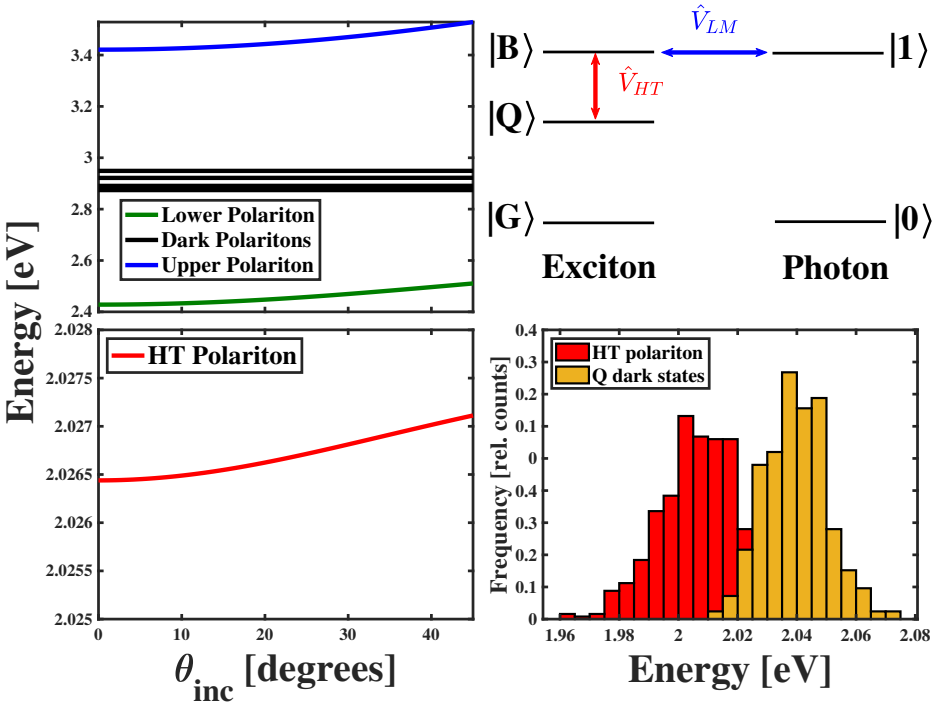


Figure 3.1: Top left panel: predicted dispersion of the upper polariton (blue), dark polariton (black), and lower polariton (green) states of a strongly coupled molecule-cavity photon system found by diagonalizing Eq. (3.2) for 5 molecules and a light-matter coupling constant of 0.5 eV. Bottom left panel: predicted dispersion of a Herzberg-Teller (HT) vibronic polariton state found by diagonalizing Eq. (3.2) for 5 molecules and a light-matter coupling constant of 0.5 eV and HT vibronic coupling strength, $\hat{V}_{HT}$ = 0.1 eV. Top right panel: schematic representation of cavity polariton formation in the presence of HT vibronic coupling. A model metalloporphyrin molecule possesses a ground state, $|S_0\rangle$, and two singlet excited states,$|Q\rangle$ and $|B\rangle$, which become coupled by the HT vibronic interaction Hamiltonian, $\hat{V}_{HT}$. The N=1 photon state of a cavity mode couples to the $|S_0\rangle \rightarrow |B\rangle$ transition via the light-matter coupling interaction, $\hat{V}_{LM}$. Bottom right panel: relative distributions of energies corresponding to HT polariton states (red) and dark Q states (yellow) found by diagonalizing Eq. (3.2) for 5 molecules possessing disordered energies and a light-matter coupling constant of 0.5 eV and HT vibronic coupling strength of 0.1 eV.

energy, $E_{cutoff}$, stems from the finite length of the resonator and $n_{eff}$ varies from a real, constant value due to light absorption by the cavity-embedded molecules. Diagonalization of the Hamiltonian in Eq. (3.2) leads to formation of the upper polariton (UP) and lower polariton (LP) states, which delocalize through the cavity due to their photonic content, and a lower lying state that mixes $|Q\rangle$ with the polariton states via $\hat{V}_{HT}$.

To understand how these energetics vary with the number of molecules one embeds within the cavity, we extend the Hamiltonian in Eq. (3.2) to the case of 5 molecules, which leads to our writing $\hat{H}$ as the 11-dimensional, square matrix we report in Appendix C. This extension causes the formation of four dark polariton states found at energies between those of the two polaritons, which we show in the top left panel of Figure 3.1. In addition, we find four, non-dispersive states appear at energies near that of the lower lying electronic state $|Q\rangle$, which we shown in the bottom panel of Figure C1. For light-matter coupling strengths sufficient to produce well-separated polaritons, the lowest lying state becomes dispersive, as shown in the bottom left panel of Figure 3.1. The dispersive nature of this state implies polariton formation drives photonic mixing with a state not coupled to the cavity directly. We refer to this dispersive state as the HT polariton.

In addition to its mixing with the cavity photons via the HT interaction described by Eq. (3.1), we find the HT polariton always lies at an energy below those of the dark Q states. We make this conclusion following calculation of the HT polariton energies when we distribute the molecular transition frequencies $\omega_B$ and $\omega_Q$ normally around central values consistent with the UV-vis spectrum of CuTPP, which is shown in Figure 3.2. We generate this distribution by repeating the diagonalization of the five-molecule Hamiltonian 500 times and recording the randomly produced energies for states in the bright and dark manifolds. We compare the results of these calculations in bottom right panel of Figure 3.1 in the case of a collective light-matter coupling strength of $V_{LM}$ = 0.5 eV and HT coupling strength $V_{HT}$ = 0.1 eV, which is consistent with estimates of vibronic coupling strength in CuTPP as established from absorption and resonance Raman spectroscopic studies[122,123]. This comparison shows that even in the case of a molecular ensemble with disordered

energies, the energies of the HT polaritons distribute around a central value a few 10s of meV below that of the dark Q states. Based on this finding, we predict the presence of HT polaritons would manifest itself as the appearance of spectroscopic signatures at energies below those that the states of a vibronically active molecule would possess in free space. One can equate the width of the HT polariton energy distribution in the bottom right panel of Figure 3.1 as the uncertainty in this state's energy, which results from the inhomogeneous broadening of the molecular state energy due to disorder.

We note that the HT polaritons we predict differ from vibronic polaritons anticipated to participate in light emission processes due to the Frank-Condon overlap of vibrational wavefunctions in the ground and excited electronic states of molecules coupled to cavity photons. Those excitations result from the relative geometric rearrangements of molecular excited states and produce light emission features in the spectral vicinity of the $|UP\rangle$ and $|LP\rangle$ states, which confound simple interpretation of their emission spectra[124,125]. In contrast, the left panels of Figure 3.1 show the HT polariton appears at an energy nearly 1 eV below that of the $|UP\rangle$ and $|LP\rangle$ states and will not cause light emission in their spectral vicinity. Despite this difference, the formalism used to explain vibronic polariton photoluminescence spectra can help one understand light emission from HT polaritons, as we explain below.

## 3.3 Experimental results

To test the predictions of the model detailed above, we chose to form cavity polaritons with copper (II) tetraphenyl porphyrin (CuTPP), which we have used in previous studies to understand the effects of molecular chromophore spectral properties on polariton dynam-

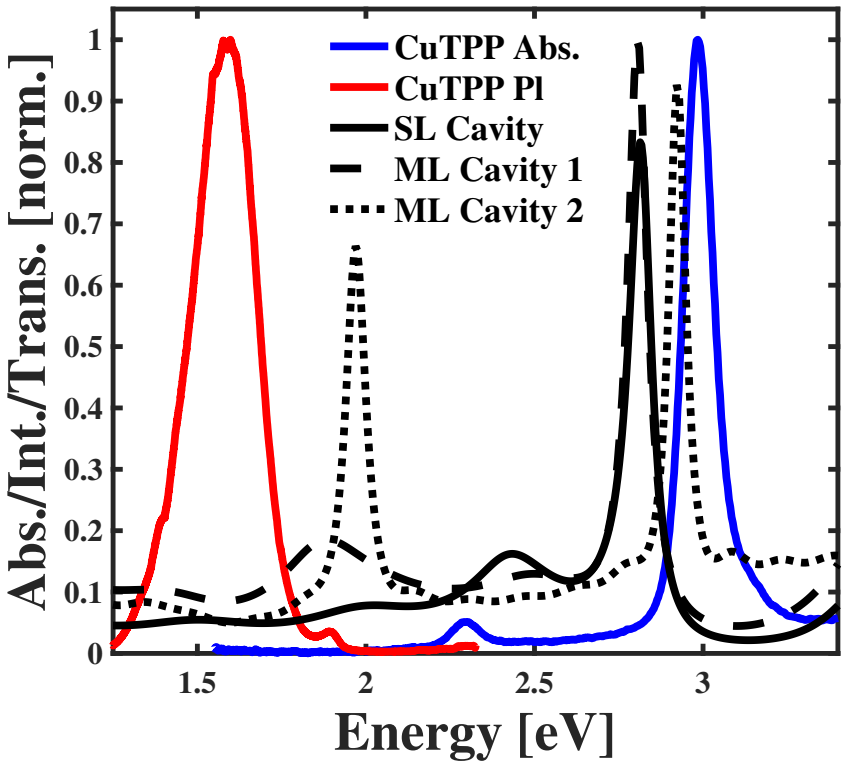


Figure 3.2: Comparison between the absorption (blue) and photoluminescence (red) spectra of 1.95 mM of copper (II) tetraphenylporphyrin in a 145 nm polymethyl methacrylate (PMMA) film to model transmission spectra corresponding to a single layer cavity (solid black), a multi-layer cavity formed from a distributed Bragg reflector (DBR) mirror possessing a single photonic stopband (dashed black), and a multi-layer cavity formed from a distributed Bragg reflector (DBR) mirror possessing a three photonic stopbands (dotted black).

ics[102]. Studies show vibronic coupling strengths on the order of 100 meV are necessary to adequately model the UV-vis and resonance Raman spectra of CuTPP[106,122,123]. Based on our model results, we expect cavity polariton samples formed with CuTPP could possess HT polariton states consistent with the energetics in left panels of Figure 3.1.

In addition to our choice of CuTPP as the molecular constituent of our cavity polariton states, we designed different multi-layer resonator structures in an attempt to understand the properties of the HT polariton states more completely, which we detail in the Methods

section of Appendix C. Figures C2-C4 compare the schematic designs of the single and multi-layer resonator structures we fabricated and the predominant, standing cavity mode we intend to use for polariton formation in each respective resonator. This comparison shows that while we use the $\lambda/2$ mode of the single layer structure for polariton formation, we use our cavity design to drive polariton formation in two distinct, three-layer resonators using their $3\lambda/2$ modes. Furthermore, we fabricated these multi-layer cavity polariton samples using two distinct distributed Bragg reflector (DBR) designs. In one structure, we use alternating layers of $SiO_2$ and $Si_3N_4$ possessing thicknesses of 58.9 nm to produce a single photonic stopband centered at 425 nm (2.92 eV) when a light beam impinges on the DBR at normal incidence. In contrast, we used alternating layers $SiO_2$ and $Si_3N_4$ possessing thicknesses of 178.5 nm to produce three photonic stopbands centered near 1285 nm (0.96 eV), 640 nm (1.94 eV), and 430 nm (2.88 eV) at normal incidence in other structures. By capping the multi-layer structures with thin Al films, we anticipate forming multiple cavity modes using each DBR design. However, we expect the quality factor ($Q_c = \omega_c/\Delta\omega_c$) of the cavity mode near the energy of the light emission from the $^2$Q state of CuTPP, as shown in Figure 3.2, will be higher for the resonator structure whose DBR possesses a photonic stopband at the corresponding wavelength. We denote the single layer cavity, multilayer cavity possessing one photonic stopband, and the multilayer cavity possessing three photonic stopbands as SL cavity, ML cavity 1, and ML cavity 2 samples, respectively. The full description of the procedures we used to fabricate our resonator structures can be found in the Experimental Methods section of Appendix C.

In Figure 3.2, we show the light absorption and emission spectra of CuTPP molecules embedded in a 145 nm film of PMMA that has been capped with a 12 nm thin film of

polycrystalline Al. The absorption spectrum of CuTPP shows the strong Soret transition between the $^2S_0$ and $^2B$ states of this molecule, which possess an overall doublet spin multiplicity due to unpaired electron in the $d$ shell of the $Cu^{2+}$ cation[94]. In addition, we find the appearance of only a single absorption peak at 2.3 eV assigned as the 0-1 vibronic $^2S_0 \rightarrow ^2Q$ transition, which occurs due to $\hat{V}_{HT}$.

The light emission spectrum of CuTPP shown in Figure 3.2 contains two separate features. A higher energy, but relatively less intense peak appears at 1.9 eV due to light emission from the vibrationally relaxed $^2Q$ state. In addition, a more intense peak appears at 1.6 eV with a shoulder at lower energy due light emission from the $^2T_1$ and $^4T_1$ states, respectively, which gain some intensity through exchange mixing with the $^2B$ state of CuTPP[94]. The large difference in the intensities of the distinct features in the PL spectrum of CuTPP stems from the $\sim$300 fs relaxation of the $^2Q$ state into the triplet state manifold[65,66], which limits the overall quantum efficiency of light emission from the $^2Q$ state dramatically.

We also show the normal incidence transmission spectra of the SL cavity, ML cavity 1, and ML cavity 2 samples in Figure 3.2. We estimate these spectra from transfer matrix models of unloaded cavities to appreciate their spectral alignment with the resonances of CuTPP[16]. Comparing these transmission spectra to the light absorption and emission spectra of CuTPP shows each cavity structure possesses a distinct mode capable of coupling to the Soret transition of CuTPP when one angles the cavity structure appropriately. In contrast, only the ML cavity 1 and ML cavity 2 samples possess modes that overlap energetically with the light emission from the $^2Q$ state of CuTPP. Moreover, the transmission spectra of the ML cavity 1 and ML cavity 2 samples in Figure 3.2 confirm we can deter-

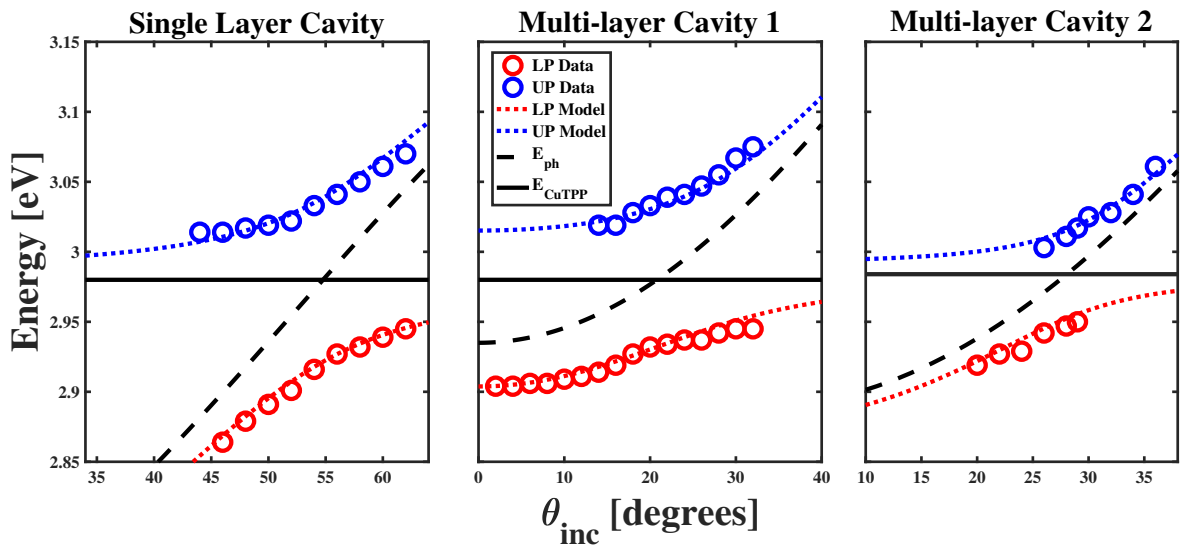


Figure 3.3: Comparison between the measured dispersion of cavity polariton peaks (circles) to models found from Eq. (3.3) (dotted lines) for the SL cavity sample (left panel), the ML Cavity 1 sample (middle panel), and the ML cavity 2 sample (right panel), which are described in the main text. We show the dispersive photon energy found from Eq. (3.3) and the exciton Soret transition energy as dashed and solid black lines, respectively, in each panel.

ministically control the quality factors of cavity modes that overlap with specific features in the light emission spectrum of CuTPP. Overall, this comparison confirms our multi-layer resonator structures allow us to couple photons in distinct cavity modes to the B and Q electronic states of CuTPP on separate footing, even under strong light-matter coupling conditions.

The panels of Figure 3.3 show we find the characteristic dispersive behavior of cavity polariton states in the transmission spectra of all our loaded resonator structures when changing the angle of an incident probe field. We describe our experimental approach for measuring cavity polariton peaks in the Experimental Methods section of Appendix C. For simplicity, we model the dispersive peak positions using solutions to a 2x2 Hamiltonian describing the coupling of cavity photons with dispersive energies $E_{ph}(\theta) = \hbar\omega_c$ to the

Table 3.1: Quantitative comparison between the collective vacuum Rabi splitting energies, cavity photon energy cutoff, and effective index of refraction found from models of the polariton dispersion curves shown in the panels of Figure 3.3

| **Sample** | $\hbar\omega_R$ **[meV]** | $E_{cutoff}$ **[eV]** | $n_{eff}$ |
|---|---|---|---|
| Single Layer Cavity | 117 | 2.66 | 1.82 |
| Multi-layer Cavity 1 | 100 | 2.94 | 2.05 |
| Multi-layer Cavity 2 | 90.4 | 2.89 | 1.88 |

excitonic Soret transition of CuTPP, which has a non-dispersive energy $E_{ex}$. Diagonalizing these matrices produces the equations[7,73],

$$E_{LP}(\theta) = \frac{E_{ph}(\theta) + E_{ex}}{2} - \frac{1}{2}\sqrt{[E_{ph}(\theta) - E_{ex}]^2 + 4V_{LM}^2}, \tag{3.3a}$$

$$E_{UP}(\theta) = \frac{E_{ph}(\theta) + E_{ex}}{2} + \frac{1}{2}\sqrt{[E_{ph}(\theta) - E_{ex}]^2 + 4V_{LM}^2}, \tag{3.3b}$$

where $\theta$ is the angle the incident probe field makes with the surface normal of the Fabry-Pérot cavity structure and $V_{LM}$ is the light-matter strength. We compare the dispersive properties of polaritons, photons, and excitons found from Eq. (3.3) to the measured polariton peak energies in each respective panel of Figure 3.3 and report the model results for each respective cavity in Table I. The models suggest each one of the cavity samples possesses polariton states separated by a collective vacuum Rabi splitting energy near 100 meV, which allows us to compare the light emission spectra of these samples on equal footing with respect to this polariton property. Figures C5 and C6 show representative transmission spectra of the SL cavity, ML cavity 1, and ML cavity 2 samples demonstrating the presence of distinct peaks we assign as cavity polaritons. Additionally, Figure C7 shows the dispersion of the lower lying cavity mode of the ML cavity 2 sample, which we observe just above 2 eV for all the incident angles used in our measurements.

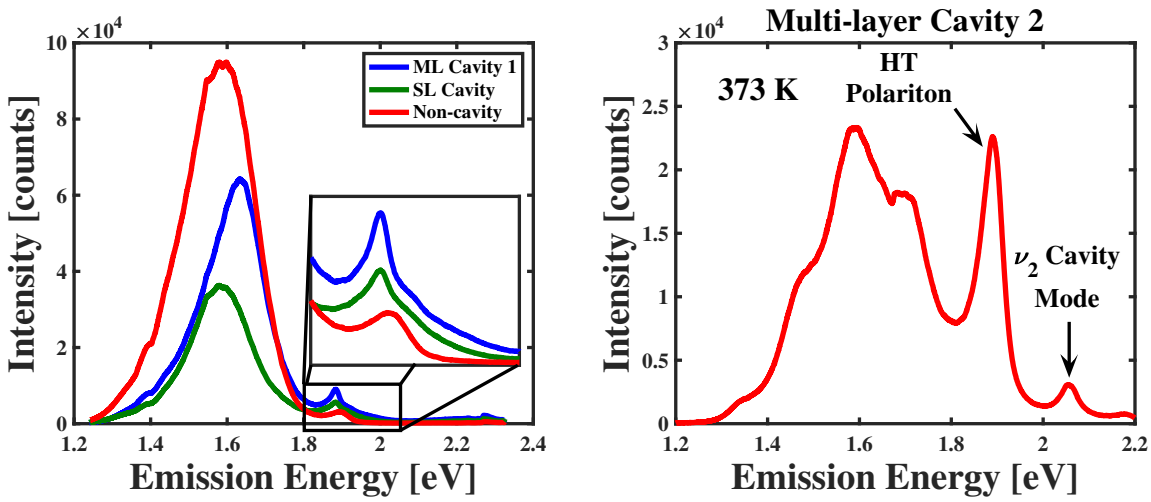


Figure 3.4: Left panel: comparison between the low temperature (80 K) photoluminescence (PL) spectra of CuTPP molecules in the ML cavity 1 sample (blue), the SL cavity sample (green), and embedded in an Al-capped polymer film (red) following excitation with a 2.33 eV laser. Inset: zoomed comparison of CuTPP PL of each sample in the region we assign as emission from the molecule's $^2$Q state. Right panel: comparison of the temperature-dependent PL emitted by the ML cavity 2 sample at 373 K following excitation with a 2.33 eV laser showing the near equality of the $^2T_1$ and $^2$Q peak intensities, in contrast to the spectra in the left panel.

We assess the ability of our optical resonator structures to sustain HT cavity polaritons by measuring their light emission spectra following laser excitation at 2.33 eV, as detailed in the Experimental Methods section of Appendix C. While this laser energy is not resonant with the polariton states shown in the panels of Figure 3.3, we do excite the $^2$Q states cavity-embedded CuTPP molecules resonantly at this energy, as shown in Figure 3.2. We then compare those spectra to that of a control sample in which we have spun a 145 nm PMMA film from a 1.98 mM CuTPP-polymer precursor solution on a glass substrate without a DBR structure and capped the film with a 12 nm layer of aluminum, as detailed in our previous study[102]. We compare these spectra in the panels of Figure 3.4.

The left panel of Figure 3.4 shows the expected PL spectra emitted by the film-embedded CuTPP molecules as a solid red line. Light emission from the $^2$Q state of CuTPP appears as

Table 3.2: Quantitative comparison between the energies, widths, and models used to understand the light emission peaks in the vicinity of that of the $^2$Q state of CuTPP. *indicates assumed value based on measurements made on control samples.

| **Sample** | **$E_1$ [eV]** | **$\Delta E_1$ [meV]** | **Model 1** | **$E_2$ [eV]** | **$\Delta E_2$ [meV]** | **Model 2** |
|---|---|---|---|---|---|---|
| Non-cavity | 1.9 | 33 | Gaussian | - | - | - |
| SL Cavity | 1.9* | 43 | Gaussian | 1.88 | 20 | Lorentzian |
| ML Cavity 1 | 1.91 | 43 | Gaussian | 1.88 | 16 | Lorentzian |
| ML Cavity 2 | - | - | - | 1.89 | 24 | Lorentzian |

the relatively weak, Gaussian peak centered at 1.9 eV while the light emission stemming from the manifold of triplet states of the molecule appears as a broader peak and shoulder at 1.6 eV possessing significantly more intensity[94,102]. In contrast to the single, Gaussian peak we find corresponding to light emission from the $^2$Q state of CuTPP in the non-cavity sample, we find the light emission spectra of SL cavity and ML cavity 1 samples possess two distinct peaks that lie at similar energies, as shown in the inset of the left panel of Figure 3.4. The less intense of the two peaks resembles that of the non-cavity sample while the other, more intense peak appears at 1.88 eV in both cavity polariton samples. This energy lies 10 meV below the $^2$Q emission of the non-cavity sample. In addition, we find the peaks in the PL spectra of the SL cavity and ML cavity 1 samples possess widths of 22 meV and 17 meV, respectively, which are approximately half of the width of the peak we assign to the $^2$Q state of CuTPP we measure in the PL spectrum of the non-cavity sample. In Table II we report the energies of the peaks in each of the spectra in Figure 3.4.

The red-shift in the energy of these additional peaks relative to that of the single Gaussian peak in PL spectrum of the non-cavity sample resembles the difference in energy between the HT vibronic polaritons and dark Q states predicted by Eq. (3.2) and shown in the bottom right panel of Figure 3.1. Despite this resemblance, we find these peaks appear in samples possessing light-matter coupling strengths nearly a factor of 10 smaller

than those we considered in our model. Moreover, we find we need to use a Lorentzian shape to fit the PL spectra of the SL cavity and ML cavity 1 samples adequately, as shown in Figure C8. This Lorentzian shapes suggests the light emission stems from a state of a homogeneously broadened system, like a cavity polariton. However, the left panel of Figure 3.4 shows we still find that the light emission we measure at 1.88 eV for the SL cavity and ML cavity 1 samples remains significantly less intense than the feature corresponding to radiative relaxation of the CuTPP triplet states.

To further characterize possible light emission from HT vibronic polaritons formed by strongly coupling the electrons of CuTPP to cavity photons, we measured the PL spectrum of our ML cavity 2 sample, as shown in the right panel of Figure 3.4 for a sample temperature of 373 K. This spectrum shows two important features consistent with the presence of HT polaritons. First, we find the appearance of a narrow peak at 1.89 eV whose intensity matches that of the broad feature at lower energies. The slight red-shift of this peak with respect to the $^2$Q fluorescence we find in the non-cavity sample resembles the value we expect from our model results, shown in Figure 3.1. For the sake of brevity, we denote this peak as HT polariton in the right panel of Figure 3.4. Second, the spectrum features a low intensity peak centered at 2.06 eV. The energy of this peak matches that of a dispersive feature we find in angle-resolved steady-state transmission measurements of the ML cavity 2 sample, as shown in Figure C7. Based on this coincidence, we denote this peak as $\nu_2$ cavity mode in the right panel of Figure 3.4. We propose its appearance in the PL spectrum of the ML cavity 2 sample stems from the CuTPP 0-0 fluorescence transition enhanced by the cavity mode.

We also measured the temperature dependent PL spectra of the ML cavity 2 sample.

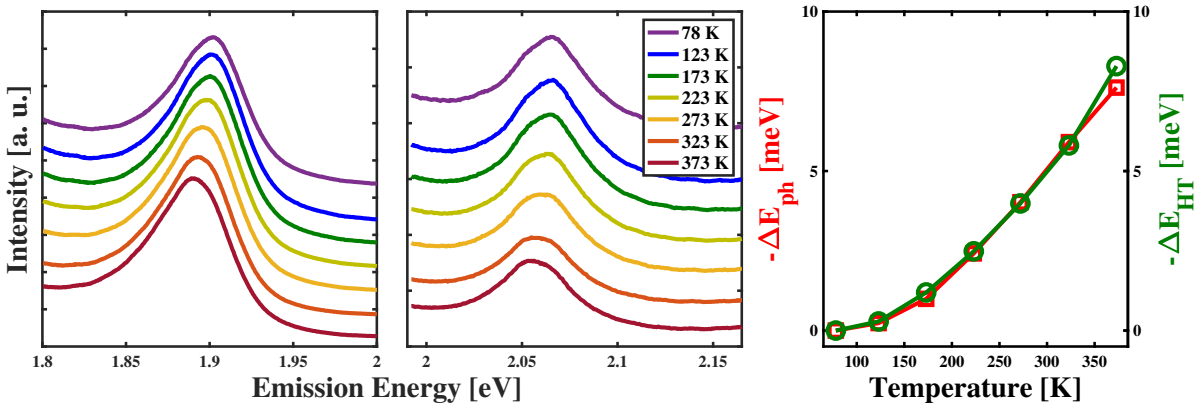


Figure 3.5: Left panel: temperature dependent light emission from the HT polariton of the multi-layer cavity 2 sample, as assigned in the text. Middle panel: temperature dependent light emission from the $\nu_2$ cavity mode of the multi-layer cavity 2 sample, as assigned in the text. Right panel: comparison between the temperature-dependent shift of the HT polariton peak position (green circles) to that of the $\nu_2$ cavity mode peak (red square).

Due to the finite thermal expansion coefficients of the materials comprising the ML cavity 2 sample, we anticipate changing this sample's temperature will affect the overall length of the intracavity region. These changes in the cavity length will then cause temperature-dependent differences in the lowest energy photonic mode allowed within the resonator, $E_{cuttoff}$ as defined above, which qualitatively resembles the dispersive behavior of the cavity polaritons shown in Figures 3.1 and 3.3 of the main manuscript and Figures C4-C6 of Appendix C. Based on this physical picture, we expect the PL peak we assign to the $\nu_2$ cavity mode in the right panel of Figure 3.4 to shift its spectral position as a function of temperature, which we extract using a spectral model explained in Appendix C. Comparisons between our experimental results and this model, as shown in Figure C9, demonstrates its utility.

The middle panel of Figure 3.5 shows the expected, temperature-dependent shift of the $\nu_2$ cavity mode peak. In addition to the expected shift we find for the peak whose energy

overlaps with a well-defined cavity mode within the ML cavity 2 sample, the left panel of Figure 3.5 shows the position of the HT polariton peak in the PL spectrum of the ML cavity 2 sample also shifts to higher energy energies as we reduce its temperature.

Figure 3.5 shows the temperature dependent shifts of each PL peak relative to the spectral location we find at 78 K. Most interestingly, this comparison shows the peaks we assign to both the HT polariton and the $\nu_2$ cavity mode shift in nearly the same manner as we change the ML cavity 2 sample temperature. This result indicates the states involved in the radiative relaxation process giving rise to the peak we assign to the HT polariton possess substantial photonic content despite the fact that the photons emitted from the HT polariton state at 1.89 eV do not overlap directly with the energy of the $\nu_2$ cavity mode. Figure C10 shows the energy of the CuTPP $^2$Q state light emission in the non-cavity sample does change slightly as a function of sample temperature, but in a qualitatively different way than the trends shown in the right panel of Figure 3.5. We propose the results in Figure 3.5 stem from the fact that the difference between the energies of the HT polariton and the $\nu_2$ cavity mode peaks in Figures 3.4 and 3.5 nearly matches that of the vibration known to mediate $\hat{V}_{HT}$ in metalloporphyrins, which appears in previously published resonance Raman excitation spectra of CuTPP[122].

## 3.4 Discussion

LaRocca and Spano have presented results from analytical models capable of describing the role of vibronic coupling in cavity polaritonic samples in which molecular chromophores couple strongly to resonator photons[43,124–126]. In particular, Spano and coworkers show cavity photon states dressed by collective vibrational excitations play an

important role in explaining the structure of photoluminescence spectra of polariton samples formed from cyanine dyes capable of forming $J$-aggregates[124,125]. For an ensemble of $N$ molecules possessing ground and excited electronic states, $|g\rangle$ and $|e\rangle$, respectively, the vibrationally dressed photon states can be represented in a two-particle excited-state basis of the form,

$$|\beta, \tilde{\nu}, 1_c\rangle = \sum_{n}^{N} c_{\beta_n} |g_1 0_1, ...., g_n \tilde{\nu}_n, ...., g_N 0_N, 1_c\rangle, \tag{3.4}$$

where $\beta$ represents the permutation quantum number of the wavefunction, $\tilde{\nu}$ in the number of vibrational excitations on the $n^{th}$ molecule of the ensemble, and $1_c$ indicates the cavity mode becomes loaded with a single photon. Physically, we interpret Eq. (3.4) as the coherent superposition of vibrational excitations on a set of $N$ distinct molecules in the presence of a cavity photon that persists when those molecules couple strongly to cavity photons via the excited state $|e\rangle$. These photon states dressed with the collective vibrations described by Eq. (3.4) can provide final states in photoluminescence from the polariton states.

To help explain the increased intensity of the HT polariton peak in the PL spectrum of the ML cavity 2 sample relative to 1.89 eV peaks we measure in the PL spectra of the SL cavity and ML cavity 1 samples, we presume the two states $|1\rangle_{HT}|\beta, 0, 0_c\rangle$ and $|0\rangle_{HT}|\beta, 1, 1_c\rangle$ become weakly coupled through the cavity enhanced light-matter interaction due to the presence of the $\nu_2$ cavity mode in the ML cavity 2 sample. In the interaction picture, the

evolution of this system's wavefunction $|\Psi(t)\rangle$ becomes[127],

$$|\Psi(t,T)\rangle = C_1(t,T)e^{-\imath\delta(T)/2}|1\rangle_{HT}|0\rangle_{ph} + C_2(t,T)e^{\imath\delta(T)/2}|0\rangle_{HT}|1\rangle_{ph}, \tag{3.5}$$

where $\delta(T) = \omega_{HT}(T) - \omega_c(T) + \omega_{\tilde{\nu}}$ represents the frequency detuning between the HT polariton and the vibrationally dressed cavity mode, which we presume is a function of sample temperature, $T$, due to the thermal expansion coefficients of the materials comprising the resonator structure, as described above. We expect the evolution of the excitation in the HT polariton state will follow that of the coefficient $C_1(t)$ according to the equation[127],

$$\frac{dC_1(t,T)}{dt} = -\left[(\Gamma'/2) + \frac{g^2\left\{\kappa/2 + \imath\delta(T)\right\}}{\delta^2(T) + \kappa^2/4}\right] C_1(t,T), \tag{3.6}$$

where $\Gamma'$ and $\kappa$ are the temperature-independent rates of cavity photon losses from emission into nonconfined photonic modes and finite mirror reflectivities, respectively. In addition, $g$ represents the light-matter coupling strength between the HT polariton and the vibrationally dressed cavity photon states, which differs from the light-matter coupling $V_{LM}$ we used to model cavity polariton formation in Eq. (3.2). Integrating Eq. (3.5) and squaring the result shows the state $|1\rangle_{HT}|\beta,0,0_c\rangle$ will decay with a rate that is the sum of $\Gamma'$ and the cavity-enhanced light emission rate, $\Gamma_c = \left[\frac{2g^2}{\kappa}\right]\frac{1}{1+[2\delta(T)/\kappa]^2}$. When the difference between the energies of the HT polariton and cavity mode matches that of the HT-active vibrational mode, then $\delta(T)$ minimizes and the radiative decay rate of the HT polariton increases by $\frac{2g^2}{\kappa}$, which we estimate has an upper limit 47.8 meV (11.6 ps$^{-1}$) by fitting the HT polariton peak of Figure 3.4 to a Lorentzian shape. Given the low rate of radiative

relaxation in metalloporphyrins (0.1 $ns^{-1}$), our Lorentzian model suggests the HT polariton formation could increase radiative relaxation by orders of magnitude such that light emission competes effectively with the sub-300 fs internal conversion of the $^2$Q state of CuTPP into the manifold of molecular triplet states. We propose this dramatic change in the radiative rate drives the substantial change in the intensity of the 1.89 eV peak in the PL spectrum of the ML cavity 2 sample relative to the same peaks we measure in the SL cavity and ML cavity 1 samples.

Based on the work of Herrera and Spano, we can also model the nearly coincident shift of the peaks we assign to the HT polariton and $\nu_2$ cavity mode in the PL spectrum of the ML cavity 2 sample. According their study, the spectrum describing the radiative decay $|HT\rangle \rightarrow |\beta, \nu, 1_c\rangle$ should take the form[125],

$$S_{PL}^{(HT)}(\omega) = \rho_{HT}|\langle 1_{HT}|\langle\beta, 0, 0_c|\hat{a}|0_{HT}\rangle|\beta, 1, 1_c\rangle|^2 \frac{\Gamma/2}{\left[\omega - (\omega_{HT}(T) - \omega_c(T) + \omega_{\tilde{\nu}})\right]^2 + (\Gamma/2)^2}, \tag{3.7}$$

where $\rho_{HT}$ is the laser-driven population of the HT polaritons and $\Gamma = \Gamma' + \left[\frac{2g^2}{\kappa}\right] \frac{1}{1+[2\delta(T)/\kappa]^2}$, as described above. The form of Eq. (3.7) shows the peak we assign as light emission from the HT polariton into the vibrationally dressed photon state will shift according to the temperature dependence of the detuning $\omega - [\omega_{HT}(T) - \omega_c(T) + \omega_{\tilde{\nu}}]$. Thus, if the cavity mode energy shifts as the resonator expands or contracts with temperature, then Eq. (3.7) shows the energy of the HT polariton PL peak should also shift when this state relaxes radiatively into the cavity photon states dressed by the collective molecular vibrations. We find the experimental results in the left and right panels of Figure 3.5 reproduce this temperature-

dependent peak shift and propose the peak we measure at 1.89 eV in the ML cavity 1 and ML cavity 2 samples stems from HT polaritons formed through the presence of both strong light-matter and non-Condon vibronic coupling.

Eq. (3.7) also shows the large shift in the position of the HT polariton PL peak results from changes in the cavity photon energy predominantly. However, small differences between the shifts of each peak should result from the temperature dependence of the HT polariton energy, $\omega_{HT}$, which also appears in Eq. (3.7) but should not appear in the spectrum describing the $\nu_2$ cavity mode PL peak. By subtracting these shifts, one should be able to estimate the dispersion of the HT polariton as a function of temperature and compare that dispersion to our predictions in the bottom left panel of Figure 3.1. Despite this physical picture, the $\sim$1 meV uncertainty in our determination of the temperature-dependent HT peak positions inhibits a quantitative estimate of the HT polariton dispersion in the ML cavity 2 sample. Further studies on cavity polaritons formed from Co and Ni-centered porphyrins may help to resolve the HT polariton dispersion more directly.

In addition to indicating that one can utilize molecular properties to form new types of cavity polaritons, our results also show a resonator's structure can enhance the light emission from HT polaritons in ways that differ from the standard Purcell effect. With appropriate cavity design, one could create higher $Q_c$ modes capable of more strongly increasing the radiative rate of the HT polaritons such that this process outcompetes ultrafast non-radiative relaxation to lower lying states. Furthermore, one can envision coupling macromolecular species built from porphyrin macrocycles such as dimers, trimers, tetramers, and covalent organic frameworks whose optical properties would be controlled through cavity polariton formation. These changes in both resonator and molecular struc-

ture provide a large phase space to search for optimal properties in light harvesting, energy transfer, and photo-catalytic capacity.

While we excited our loaded resonator samples at laser energies distinct from those of the cavity polariton states, one envisions using direct excitation of the hybrid light-matter states formed through strong coupling between the cavity photons and the Soret transition of metalloporphyrins to control the coherence of the HT vibronic polariton states. The coupling of these states could be probed through fluorescence-detected multidimensional spectroscopic studies as a way to understand inter-mode photon-photon interactions[128–132], which could be useful for some quantum information processing methods[133–136].

## 3.5 Conclusion

In conclusion, we have used qualitative theory to predict the presence and characteristics of HT cavity polaritons whose existence stems from simultaneous strong light-matter coupling and non-Condon vibronic coupling between the B and Q states present in metalloporphyrins. At sufficiently large values of $\hat{V}_{LM}$ and $\hat{V}_{HT}$, we find one can imprint the photonic content of cavity polaritons formed through strong light-matter coupling between cavity photons and the molecule's Soret transition onto the Q state of a metalloporphyrin. In particular, we find these HT polaritons should possess energies below those of dark states and uncoupled molecules. Using several different test and control samples, we find evidence of HT polaritons in the light emission spectra of strongly coupled CuTPP-cavity systems. Additionally, we find the presence of a lower energy cavity mode in resonance with HT polariton light emission in deterministically designed resonator structures results

in enhanced and dispersive photoluminescence intensity. We propose the dispersion and increased intensity of the light emission stems from an increased radiative relaxation rate from the HT polariton state to photons in the cavity mode dressed by collective molecular vibrations. Our results show how one can leverage the complex coupling of electronic and nuclear degrees of freedom in molecular systems to enable coherent properties in hybrid light-matter systems, which may find use in optoelectronics, information processing, and photo-catalysis.

# CHAPTER 4 POLARITON-MEDIATED COUPLING OF QUASI-DEGENERATE PORPHYRIN EXCITONS.

Reproduced (or reproduced in part) from (A. G. Avramenko and A. S. Rury, "Polariton-mediated coupling of quasi-degenerate porphyrin excitons," in Frontiers in Optics, pp. JTh5A–107, Optical Society of America, 2021.), with permission of Optica Publishing Group.

## 4.1 Introduction

As discussed in Chapter 1, a polariton is formed from the interaction of a cavity photon and a molecule exchanging energy faster than the decay rate of either state. Moreover, the cavity photon and molecular exciton must have a similar energy[2,10]. The molecular exciton possesses negligible dispersivity which can be ignored[2]. However, the cavity photon's dispersivity is quite notable over the range of angles we measure and must be accounted for in our work. Because of their hybrid nature cavity polaritons will inherit some of the dispersive characteristics of the cavity photon. The fractional contributions of the cavity photon and exciton to the UP and LP are described by the Hopfield coefficients[12,13,137]. The Hopfield coefficients are found by solving for the eigenvectors of a Hamiltonian of the interacting system. A two level system in which a single cavity photon couples to a group of molecules embedded in a Fabry-Pérot cavity can be described by the following Hamiltonian[12,13],

$$\begin{bmatrix} E_{ph} - i\sigma_{ph} & V \\ V & E_{ex} - i\sigma_{ex} \end{bmatrix} \begin{bmatrix} \alpha \\ \beta \end{bmatrix} = \epsilon \begin{bmatrix} \alpha \\ \beta \end{bmatrix} \tag{4.1}$$

where the Hopfield coefficients are represented by the variables $\alpha$ and $\beta$. The polariton energy is represented by $\epsilon$. Meanwhile, V is the interaction between the cavity and exciton, which can be described as $\frac{\hbar\Omega}{2}$. Solving Eq. (4.1) results in the following eigenvector and eigenvalues[8,12],

$$\epsilon = E_{UP/LP}(\theta) = \frac{E_{ph}(\theta) + E_{ex}}{2} \pm \frac{1}{2}\sqrt{(E_{ph}(\theta) - E_{ex})^2 + 4V^2} \tag{4.2}$$

$$|\alpha_{UP/LP}|^2 = \frac{V^2}{V^2 + (E_{UP/LP}(\theta) - E_{ph}(\theta))^2} \tag{4.3}$$

$$|\beta_{UP/LP}|^2 = \frac{V^2}{V^2 + (E_{UP/LP}(\theta) - E_{ex})^2} \tag{4.4}$$

The photonic fraction of a polariton branch is described in Eq. (4.3) while the excitonic fraction is described in Eq. (4.4). While the photonic and excitonic nature of each branch will vary, the combined contributions from each state are consistent; $|\alpha|^2$+$|\beta|^2$=1. Recall from Chapter 1 that the photon energy is dispersive and is defined as $E_{ph}(\theta) = E_{cutoff}\left(1 - \frac{sin^2\theta}{n_{eff}}\right)^{-1/2}$[7,8]. Because $\epsilon$ has a photon component the energy of the polariton will be dispersive, or angle dependent. The Hopfield coefficients are the eigenvectors of Eq. (4.1). The eigenvectors are calculated using the eigenvalue ($\epsilon$). Because $\epsilon$ is dispersive it follows that the resulting $|\alpha|^2$ and $|\beta|^2$ will also depend on angle. There can also exist an angle at which $|\alpha|^2 = |\beta|^2 = 0.5$, this occurs in cavities that can trap cavity photons lower in energy than the energy of the exciton. Moreover, the angle at which the two Hopfield coefficients are equal is often referred to as the resonance angle and represents the point of maximum coupling, with the polariton state being described as a 50/50 mixture of the cavity photon and exciton. Finally, in Eq. (4.1), the factor $\sigma$ represents the decay rate of the cavity and exciton. The cavity losses, or the FWHM, of the system is imprinted in the imaginary part of Eq. (4.1).

So far, discussions in Chapters 2 and 3 have involved the formation of cavity polaritons

in which a cavity photon couples to a specific chromophore, either ZnTPP or CuTPP. However, if we extend the molecular orbital analogy to polariton formation, multiple p orbitals can interact together with an s orbital. Similarly, it is possible to embed multiple excitons into a Fabry-Pérot cavity to interact with a cavity photon. Previous studies have proposed polaritons formed from nearly degenerate Frenkel and Wannier-Mott excitons stemming from materials in different layers of a Fabry-Pérot cavity drives a photon-mediated entanglement of spatially separated material excitations across all light-matter coupling conditions[7,8]. However, it still remains unclear in what limit of near degeneracy these results exist and how to characterize similar entanglement for excitons stemming from highly disordered molecular ensembles. One parameter to characterize polaritons is the Hopfield coefficient, described in Eqs (4.3) and (4.4). In this chapter we will form a cavity polariton by coupling two nearly degenerate Soret states of a porphyrin molecule to a cavity photon.

The Hopfield coefficients determine the photonic and excitonic character of a polariton branch. Near the resonance angle the photonic and excitonic parts are equal. The LP is expected to be more photonic at lower angles, becoming more excitonic as the angle is increased. The UP will have the opposite behavior. Due to the presence of two excitons a middle polariton is expected to form as well, this polariton branch should have an equal mix of both excitons at resonance. The dynamics of a polariton are expected to be related to how the exciton and photon fractions are distributed along a polariton branch[138]. Therefore, in order to understand processes such as nonradiative energy transfer it is important to establish the fractional contributions the photon and excitons will make to the polariton states.

We design a tri-layer Fabry-Pérot cavity which includes layers embedded with CuTPP

and $H_2$TPP molecules spaced by a layer of $SiO_2$, as seen in Figure 4.1. We use a three oscillator Hamiltonian to find the energies and Hopfield coefficients of the polaritons formed using this multi-mode cavity. Our calculations indicate that the despite the quasi-degeneracy of the excitons involved in forming the polariton states each polariton branch inherits a different excitonic character.

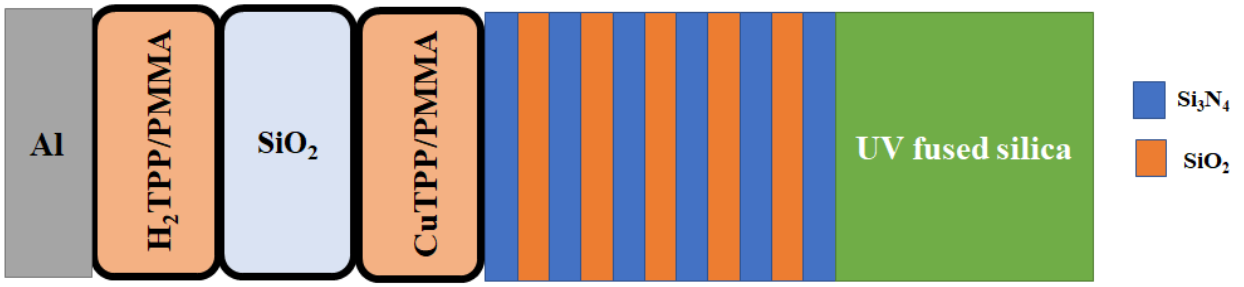


Figure 4.1: A schematic of the multi-mode cavity used to form the quasi-degenerate cavity polaritons. The nodes of the cavity photon were set at the antinode locations of a $3\lambda/2$ cavity separated by a spacer layer of length $\sim\lambda/2$.

## 4.2 Methods

Table 4.1: Comparison of the refractive index, cutoff energy, detuning, and photon-exciton interaction used to model the energy and Hopfield coefficients of our samples. A list of the cavity samples which includes the cavity composition is provided in Appendix B.

| **Sample** | **$V_1/V_2$ [meV]** | $E_{cutoff}$ **[eV]** | Detuning [meV] | $n_{eff}$ |
|---|---|---|---|---|
| Cavity 4 | 101 | 2.787 | -184 | 1.7427 |
| Cavity 15 | 108 | 2.975 | +4 | 1.8447 |
| Cavity 30 | 109 | 3.045 | +74 | 1.7447 |
| Cavity 2x | 93 | 2.885 | -86 | 1.8427 |

Distributed Bragg reflectors were fabricated using an established chemical vapor deposition method, with the details of our deposition techniques being described in Appendix A.[4,102]. 11 alternating layers of $SiO_2$ and $Si_3N_4$ were deposited on a UV fused silica substrate obtained from MTI corp. Using the wave-transfer matrix model we designed the DBR so that the stop band is centered near 718 THz, which is the average maximum absorption

of the Soret band of CuTPP and $H_2$TPP. The CuTPP was dissolved in PMMA at a concentration of $\sim$1mM and spun coated on top of the DBR structure. To form the spacer layer, we used physical vapor deposition to deposit a layer of $SiO_2$ unto the spun coated layer of doped polymer. The newly deposited $SiO_2$ layer was cured under vacuum at 70°F for 10 hours and then allowed to relax for 48 hours at room temperature. Next, $H_2$TPP was dissolved in PMMA at a concentration of $\sim$1mM and spun coated unto the structure. Finally, a layer of aluminum was deposited to cap the structure using physical vapor deposition, forming the Fabry-Pérot cavity. The final structure was designed to have a detuning of -184 meV from the Soret band of the excitons. To achieve this detuning the cavity required a thickness of 447 nm, with the thickness of each layer being equal. Two more structures with thicknesses of 412.8 nm and 408 nm, or detunings of +4 meV and +74 meV, were constructed. We also construct a cavity in which the CuTPP and $H_2$TPP doped layers are flipped, dubbin this structure as "Cavity 2x." The cavity detunings with respect to the Soret band can be found in Table 4.1. Finally, we construct a single layer CuTPP cavity with a thickness of $\sim$ 154 nm from a solution with a concentration of $\sim$ 1mM CuTPP. This cavity had a photon-exciton coupling constant of 0.117 meV and a $n_{eff}$ of 1.8227. The Polariton dispersion was measured using an Ocean FX spectrometer and a Thorlabs SLS204 lamp.

We use a three oscillator Hamiltonian to model the energies and Hopfield coefficients of the polariton samples. This three oscillator Hamiltonian has been shown to establish these quantities accurately in a quantum-well micro-cavity[138]. By expanding Eq. (4.1) to include a second exciton the new matrix becomes[7,8,138],

$$\begin{bmatrix} E_{ph} - i\sigma_{ph} & V_1 & V_2 \\ V_1 & E_{ex1} - i\sigma_{ex1} & 0 \\ V_2 & 0 & E_{ex2} - i\sigma_{ex2} \end{bmatrix} \tag{4.5}$$

where $V_1$ and $V_2$ is the interaction between the excitons and cavity photon. In the calculation we set $V_1$=$V_2$ since the thickness and concentration of the CuTPP and $H_2$TPP molecules were designed to be equal in the cavity. The peak absorption of the Soret peak of CuTPP spun coated at 4000 rpm was measured to be 0.1319 OD, while the absorption of the $H_2$TPP Soret peak was measured at 0.1113 OD. The similar intensity of the Soret peaks indicates that the oscilator strength of the $S_2$ transition in both chromophores is comparable. We use Eq. (4.5) to calculate the energy and Hopfield coefficients of the multi-mode cavity described in Figure 4.1. Table 4.1 shows the parameters used we used in our 3x3 Hamiltonian. In the Hamiltonian $\sigma_{ex1}$ and $\sigma_{ex2}$ are expected to stay contstant as the angle changes. However, the FWHM of the photon may change as the reflectivity of the DBR is angle dependent. I measured the FWHM of an empty cavity at various angles and used a Lorentzian function to fit its FWHM. I then used a polynomial to model the change in the FWHM of the cavity mode with respect to angle. This polynomial function serves to model the behavior of $\sigma_{ph}$ in Eq. (4.5). The cavity linewidth function can be found in Appendix B.2.

## 4.3 Results

The dispersion of cavity 4, which is the cavity most negatively detuned from the average Soret band of $H_2$TPP and CuTPP is shown in Figure 4.2. From Figure 4.2 we observe the near degeneracy of the Soret bands of the CuTPP and $H_2$TPP molecules as they are

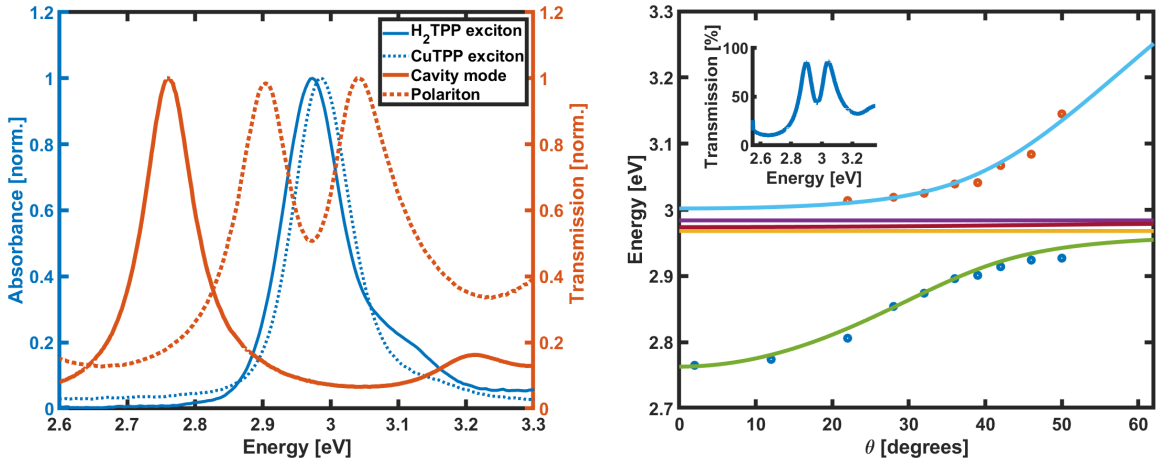


(a) (b)

Figure 4.2: a) UV-Vis spectra of the CuTPP and $H_2$TPP excitons showing their quasi degeneracy in comparison to the photon mode of a bare cavity at 0 degrees. As the cavity photon is tuned closer to the Soret band of the molecules we observe the formation of an upper an lower polariton (red dashed line). b) The dispersion curve of a multi porphyrin cavity with a detuning of -184 meV. The insert shows the transmission spectra near the resonance angle of 39 $^\circ$

.

seporated by approximatley 20 meV, or less than 1% of the energy of Soret band. The cavity photon has an energy of around 2.78 eV. As we change the angle of the cavity the energy of the photon comes closer to that of the Soret bands of the $H_2$TPP and CuTPP molecules and clear formation of an upper and lower polariton state is observed, with an observed Rabi splitting of 140 meV. Figure 4.2 depicts the dispersion curve for the cavity. Because this cavity system involves the coupling between 3 states, 2 molecular excitons and 1 photon, we expect to observe 3 final states; and upper a middle, and a lower polariton. However, as seen on the left side of Figure 4.2, there is no observable middle polariton.

We proceed to calculate the excitonic and photonic fraction of each polariton branch using the 3x3 matrix described earlier. We find the photon fraction in the lower polariton is high at low angles and proceeds to decrease as the cavity is tuned to higher angles, which

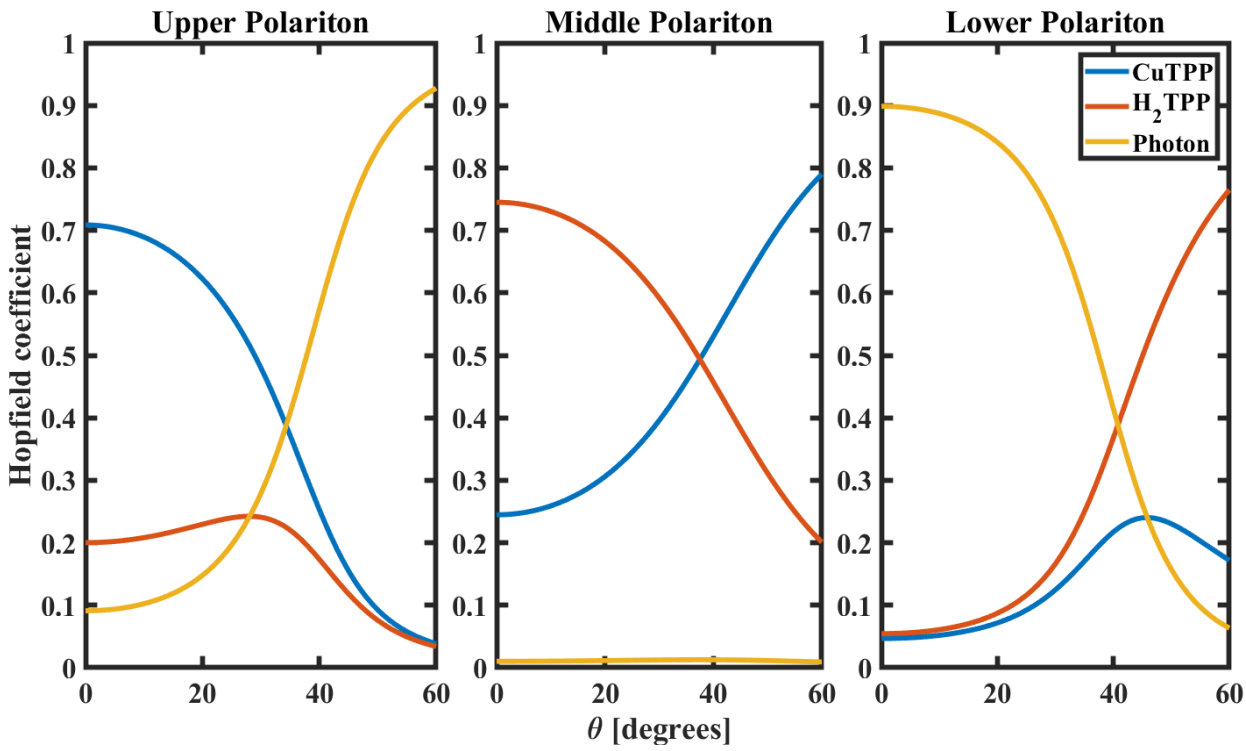


Figure 4.3: Hopfield coefficients showing the photonic (yellow), CuTPP exciton (blue) and $H_2$TPP fraction (red) of the Upper, Middle, and Lower polaritons formed from a cavity with a detuning of approximately -184 meV.

we expect[2]. However, in contrast to previous studies, we find the LP fraction of CuTPP and $H_2$TPP excitons differ substantially[7]. The CuTPP fraction of the LP state remains low, peaks near the resonance angle, and then proceeds to decrease along with the photon fraction. The $H_2$TPP fraction on the other hand steadily increases with angle. We find the reverse trend when examining the Hopfield coefficients of the upper polariton. Most interestingly, we find the photon fraction of the middle polariton remains low at all angles, suggesting that the middle polariton is highly excitonic and predominantly localized on the different molecules. This low photon content likely explains our inability to resolve the middle polariton when measuring the dispersion of the cavity structure in Figure 4.2a[139].

We repeat the measurement for cavity 15, which has minimal detuning. Figure 4.4

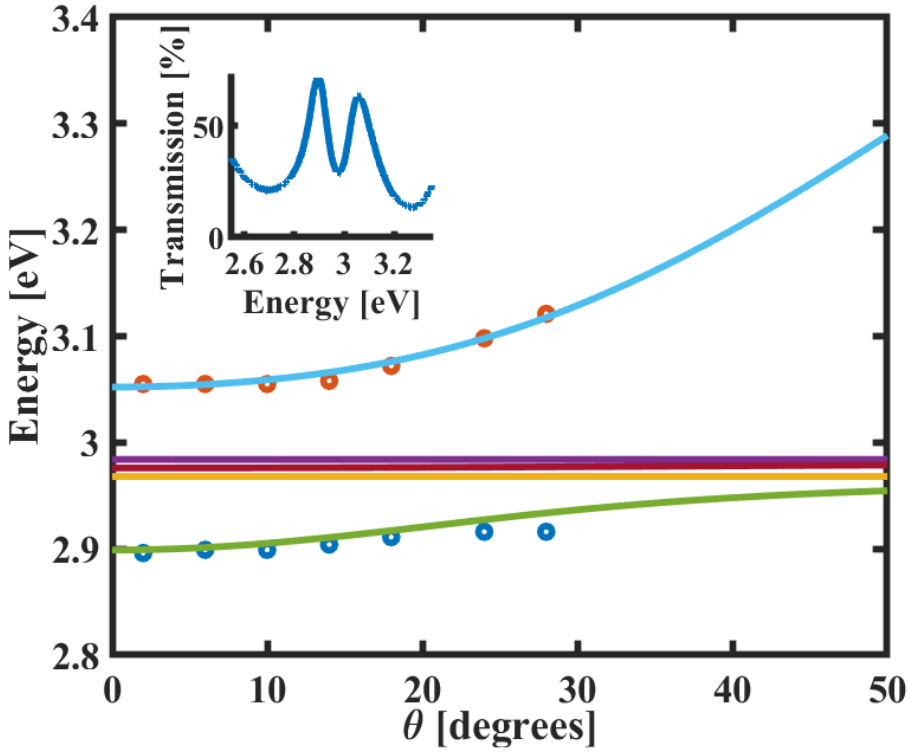


Figure 4.4: The dispersion curve for the multi porphyrin cavity with a detuning of +4 meV. The insert shows the transmission spectra near the resonance angle of 2°.

shows the dispersion curve for a cavity 15, which was designed so that the cavity mode is near resonance at an incidence angle of 0°. As the cavity thickness changes to trap higher energy photons the resulting lower polariton becomes less dispersive. This is reflected in the Hopfield coefficients by a decrease in the photonic character of the lower polariton mode, as seen in Figure 4.5. The upper polariton is affected in the opposite manner. The photon content of the UP increases and the exciton content decreases. Finally, the photonic content of the middle polariton remains negligible.

Next, we perform the measurement on a cavity 30, which is positively detuned when compared to the energy of the Soret bands of CuTPP an $H_2$TPP. The trend of the lower polariton branch becoming less dispersive continues, as seen in Figure 4.6. Moreover, we

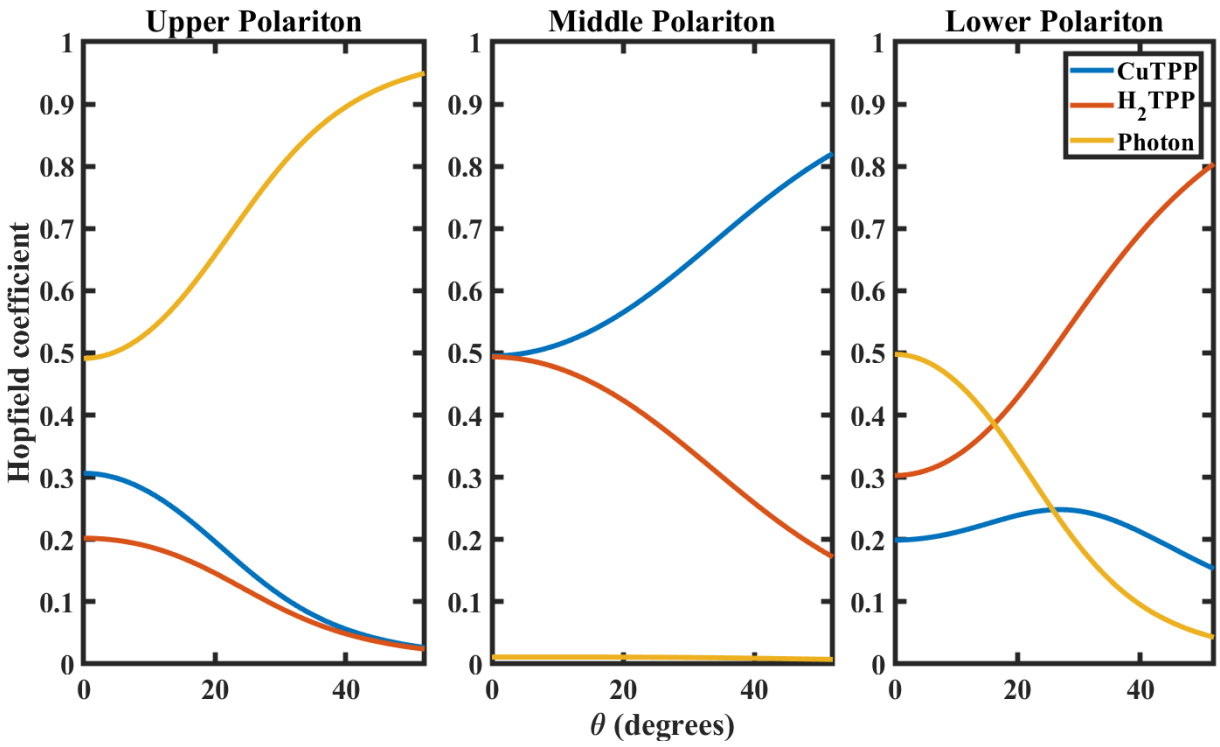


Figure 4.5: Hopfield coefficients showing the photonic (yellow), CuTPP exciton (blue) and $H_2$TPP fraction (red) of the Upper, Middle, and Lower polaritons formed from a cavity with a detuning of approximately +4 meV.

still do not observe a middle polariton branch. From the calculated Hopfield coefficients we see that the LP has a mostly $H_2$TPP-like characteristic through all angles. The UP on the other hand is largely photonic at all angles. The middle polariton continues to have a very small photonic contribution. From the calculations we observe that as the cavity is made to trap higher energy photons the middle polariton takes on a more CuTPP-like characteristic.

In the cavity design the CuTPP layer is spun coated unto the DBR while the $H_2$TPP layer is spun coated unto the $SiO_2$ spacer layer, as seen in Figure 4.1. To test if the position of the chromophores inside the cavity impacts the nature of the formed polaritons we formed a negatively detuned cavity in which the CuTPP and $H_2$TPP layer were flipped. Figure

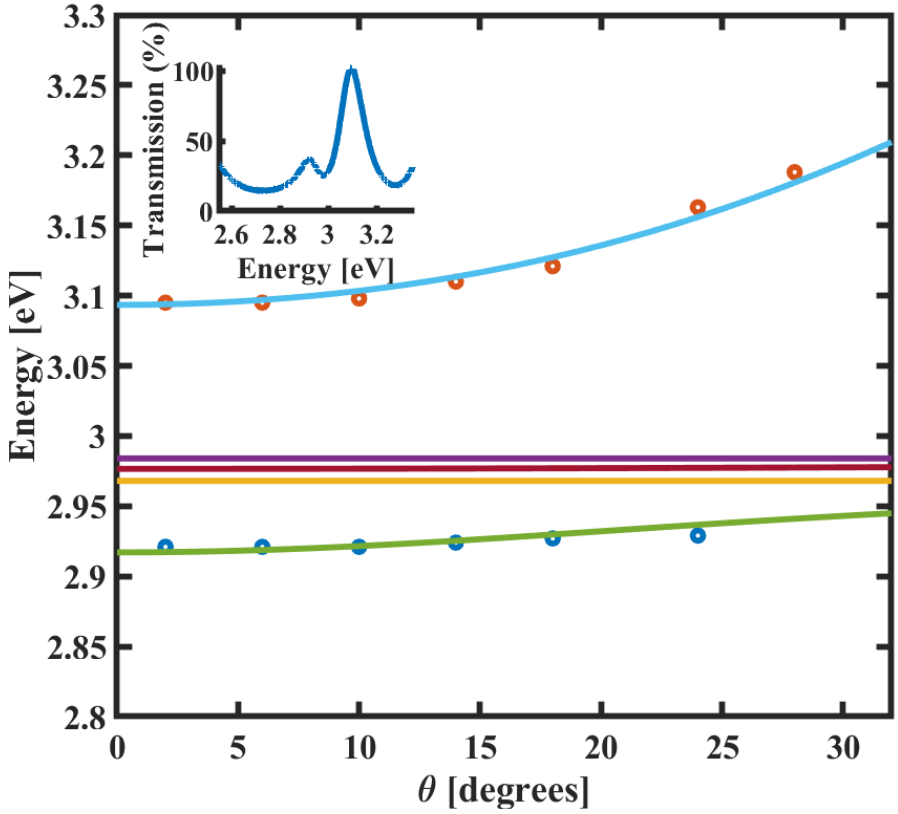


Figure 4.6: The dispersion curve for the multi porphyrin cavity with a detuning of +74 meV. The insert shows the transmission spectra near the resonance angle of 2°.

4.8 show the dispersion of this -86 meV cavity. As was the case previously, no middle polariton is observed. Calculating the Hopfield coefficients in Figure 4.9 we observe a similar behavior as the -184 meV detuned cavity 4. The CuTPP exciton fraction is dominant in the UP at low angles, with the photon fraction becoming more dominant at higher angles. The LP follows an opposite trend, having a high photon fraction at low angles and an increasingly high $H_2$TPP fraction at higher angles. Similarly to the previous calculations the photon fraction of the middle polariton is negligible.

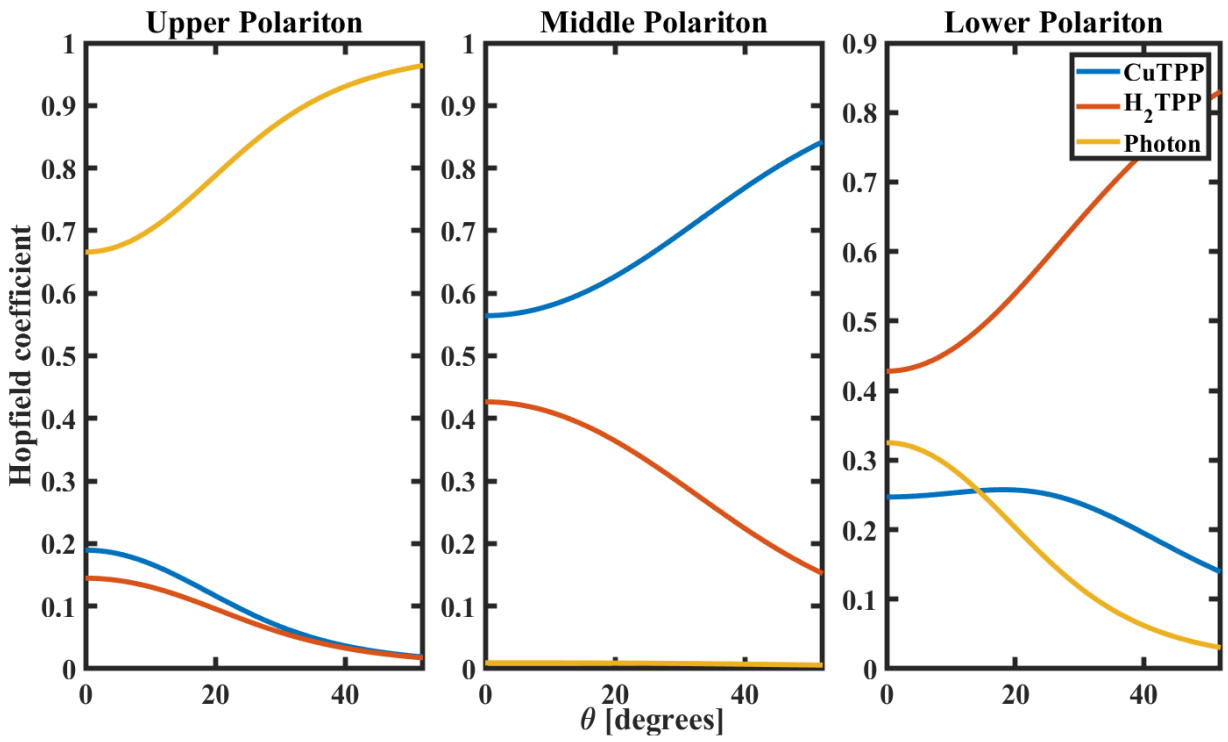


Figure 4.7: Hopfield coefficients showing the photonic (yellow), CuTPP exciton (blue) and $H_2$TPP fraction (red) of the Upper, Middle, and Lower polaritons formed from a cavity with a detuning of approximately +74 meV.

## 4.4 Hopfield coefficients of a CuTPP/$H_2$TPP multimode cavity

We observe that strong light-matter coupling of nearly degenerate Soret excitations to a single photon does not result in constant entanglement of the molecular excitons. Despite their quasi-degeneracy the UP branch inherits a more Copper-like nature, as shown by its higher CuTPP exciton fraction. As the detuning is increased the dynamic range of the Hopfield coefficients changes substantially. The UP becomes photon-like at all angles, while for the LP the $H_2$TPP exitonic fraction becomes dominant.

From the data in Figure 4.3 we notice that the exciton fractions of the UP converge at higher angles, while for the LP this convergence occurs at lower angles. This convergence of exciton fractions can be understood by examining the dispersion curve of the

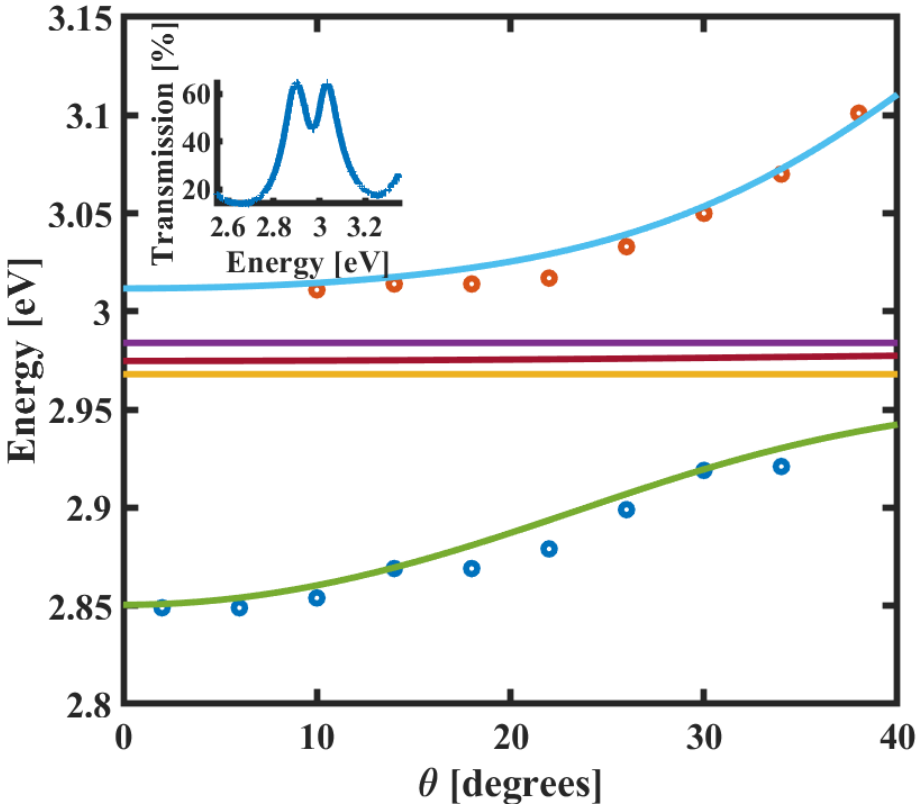


Figure 4.8: The dispersion curve of a flipped mult-imode cavity with a detuning of -86 meV. The insert shows the transmission spectra near the resonance angle of 26°.

multi-mode cavity. The maximum photon fraction of the LP will always be near angle 0 while the maximum exiton fraction will be at 90°. The combined contribution from the photonic an exitonic parts must remain constant, $|\alpha|^2+|\beta|^2+|\gamma|^2=1$. The increase in the photonic fraction around angle 0 must be accompanied by an decrease in the exitonic CuTPP an $H_2$TPP fractions, leading to a convergence of the photon an exciton fractions at low angles. The UP experiences an opposite phenomenon. As the cavity angle increases the excitonic fraction decreases, leading to a convergence of CuTPP and $H_2$TPP fractions at higher angles. We also observe maximum $H_2$TPP contribution to the UP when the cavity photon is overlapped with the energy of the $H_2$TPP band. Similarly, maximum contribu-

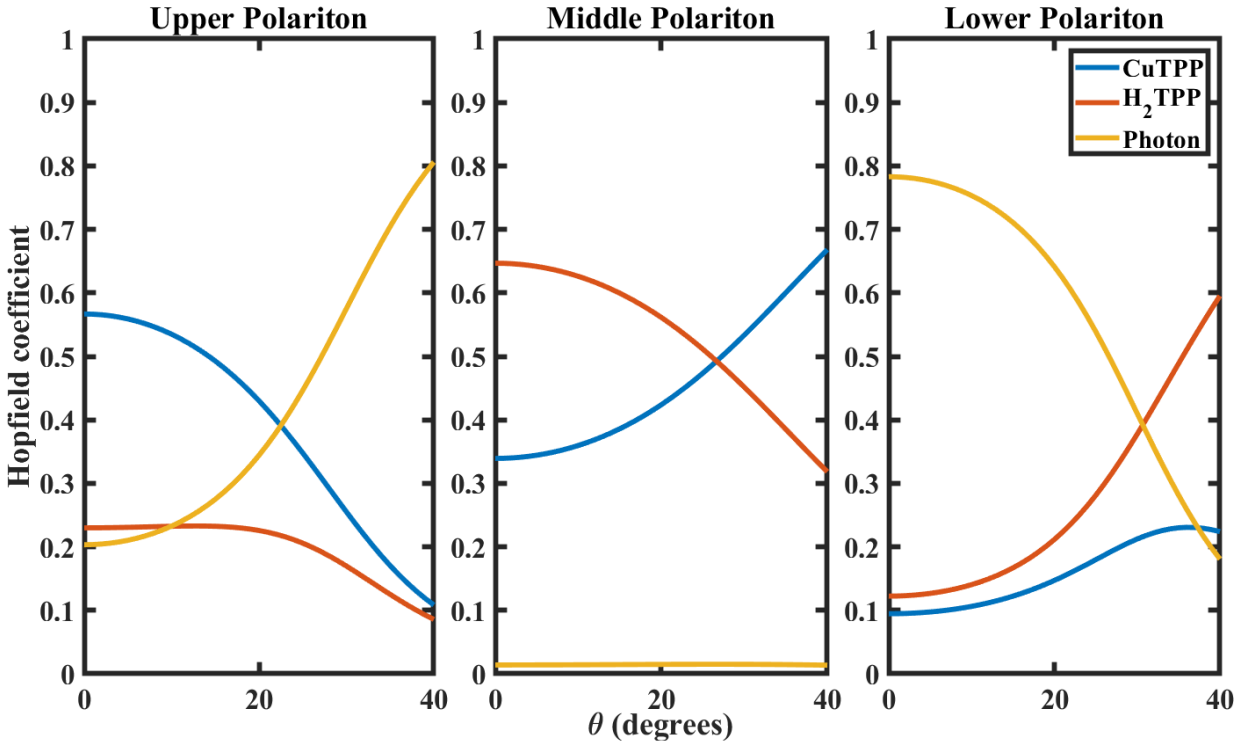


Figure 4.9: Hopfield coefficients of a flipped multimode cavity showing the photonic (yellow), CuTPP exciton (blue) and $H_2$TPP fraction (red) of the Upper, Middle, and Lower polaritons formed from a cavity with a detuning of approximately -86 meV.

tion of the CuTPP to the LP occurs when the cavity mode is tuned to the resonance of the CuTPP Soret band. A polariton state near resonance is expected to have equal contribution from the photonic and excitonic parts. As the angle is increased the energy of the cavity photon will increase. The photon fraction of the LP will decrease and the photon fraction of the UP will increase. Because the $H_2$TPP exciton is lower in energy the cavity photon will interact with it first. As the angle is tuned higher the energy of the photon will increase and the cavity photon will more closely interact with the CuTPP exciton.

Photon-mediated energy transfer processes have been sought after by physical chemists and optical engineers for a number of years[7,18,38]. The Förster resonance energy transfer (FRET) process requires an overlap in the absorption and emission spectra of two chro-

mophores. Moreover, its rate is proportional to $1/R^6$, where R is the distance between the two chormophores, which limits applications to distances of $<$ 100 Angstroms[1,18]. The Dexter energy transfer process requires wave function overlap between two chromophores, also requiring two choromophores to be in close proximity[1]. A photon-mediated energy transfer process may address these limitations. In particular, coupling both, the donor, and acceptor molecules in a quasi-degenerate system could result in the creation of delocalized polariton states that would mediate energy transfer across distances impossible for traditional processes such as FRET. To interrogate an energy transfer process the higher energy state would have to be pumped while the lower energy state is probed to observe signs of an energy transfer process between the two sates. However, the energy and nature of a polariton state is highly dependent on angle. This necessitates a calculation of its dispersion and Hopfield coefficients. Because the CuTPP and $H_2$TPP excitons are not simultaneously coupled at all angles the UP is expected to inherit the dynamics of the CuTPP at low angles, while the LP is expected to inherit the dynamics of the $H_2$TPP at higher angles. Using this information the most efficient pump energies would be at angles lower than the resonance, where the UP is mostly exciton-like, while the pump angle should be tuned to higher angles, where the LP is mostly exciton-like.

The middle polariton was found to have a negligible photonic component at all angles. The small photonic content of the middle polariton is likely the reason for our inability to observe it. This follows with previous observations conducted by Lidzey, Bradley, Skolnick and co-workers in which they concluded that the visibility of a polariton branch is proportional to the square root of its photon component[140]. The middle polariton was mostly CuTPP-like at higher angles and $H_2$TPP-like at lower angles. At the resonance angle the

middle polariton possesses an equal contribution from both excitons. This suggests that at resonance the potential energy surface of the middle polariton is an equal mixture of the CuTPP and $H_2$TPP potential energy surfaces. The ability to use light to hybridize two molecular potential energy surfaces together could suggest the potential for new photophysical and photochemical processes.

## 4.5 Dynamics of a CuTPP/$H_2$TPP multimode cavity

The Hopfield coefficients play an important role in determining the dynamics of a polariton system. As described earlier, it would be expected that a lower polariton would behave very much like a photon when tuned far below resonance, while inherting mostly the properties of an the exciton when far above rosonance. The upper polariton would be expected to have the opposite behavior. By plotting the imaginary values of the Hamiltonian described in Eq. (4.5) it is possible to calculate how the linewidth of each polariton branch is impacted by cavity detuning, as seen in Figure 4.10.

The dispersion of the photon mode was modeled by experimentally measuring the dispersion of an empty cavity and fitting the resulting FWHM to a polynomial function. The polariton spectra was modeled using the method described in Chapter 2. The UP was modeled using the asymmetric lineshape described in Eq. (2.2), while the LP was modeled using a standard Lorentzian. As seen in Figure 4.10, we observe a relatively poor fit between the experimental and predicted values. This is likely due to the model's inability to account for motional narrowing caused by polariton formation[10,30,39].

Before describing motional narrowing it is first necessary to discuss the sources of broadening within a cavity system. A polariton is a hybridization of a cavity photon and

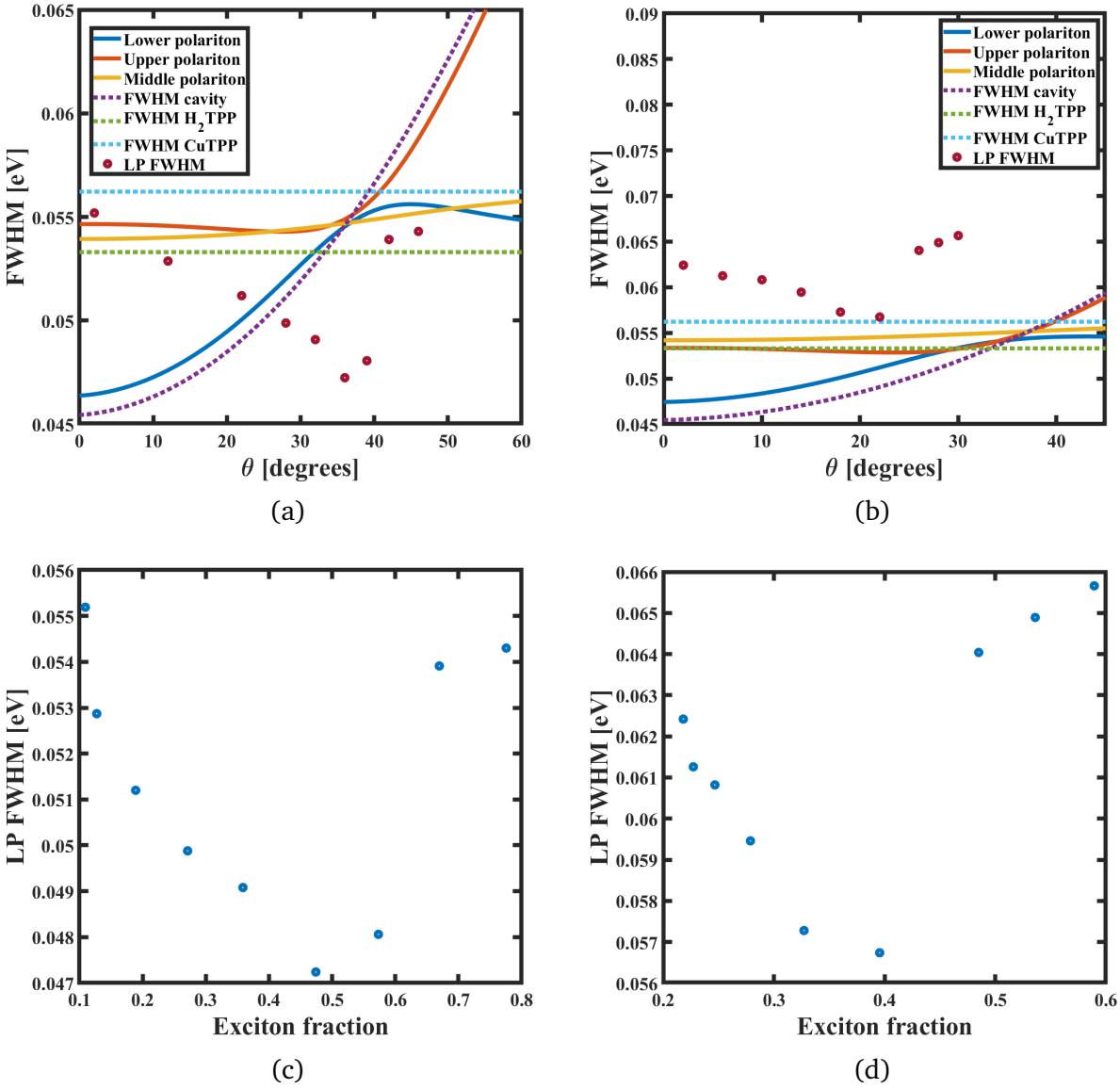


Figure 4.10: a) The calculated linewidths of a -184 meV detuned multilayer cavity sample with the experimental LP linewidths overlayed b) The calculated linewidths of a -86 meV detuned multilayer cavity sample with the experimental LP linewidths overlayed c) The experimental LP linewidths for the -184 meV detuned sample as a function of exciton fraction d) The experimental linewidths of the -86 meV detuned sample as a function of exciton fraction

.

an exciton. In this study we use the Soret excitation of the CuTPP and $H_2$TPP molecules to form the polariton structures. The cavity photon will have a lifetime largely governed by the mirror reflectivity, giving it a Lorentzian profile[141]. The excitons will have a finite

lifetime as well, which will be partly determined by the surrounding environment. The exciton will experience inhomogeneous (Guassian) broadening as porphyrin molecules located within different environments inside the cavity sample will interact differently with the incoming electromagnetic field, resulting in each exciton absorbing slightly different wavelength of light[138]. The resulting spectrum is a superposition of a collection of molecules each in a slightly different environments absorbing a slightly different energy of light. The excitons will largely interact with the environment within their De Broglie wavelength, which is orders of magnitude smaller than the size of the cavity. During strong light-matter coupling the excitons interact with the cavity photon to form delocalized polariton states. Because of the delocalized nature of the polariton, the local environmental effects which would be exerted on an exciton are now averaged over the size of the cavity, resulting in the polariton lineshape being narrower than that of the uncoupled exciton. This is particularly noticeable for the LP, as the interpolariton decay channels discussed in Chapter 2 have a profound impact on the UP[102,142].

Using this simple description, when looking at an UP branch far away from resonance it should resemble the Lorentzian lineshape of a cavity mode, while far away from resonance, the LP is expected to resemble the Gaussian lineshape of an exciton. However, a problem appears when near resonance. To properly describe the lineshape of a polariton near resonance it is insufficient to simply convolve the two functions, it also necessary to account for the motional narrowing effect. The motional narrowing effect was first explained by Whittacker *et al.*[30]. We can write a Hamiltonian to describe the kinetic and potential energy of a particle as,

$$H = \frac{\hbar^2 \nabla^2}{2M} + V \tag{4.6}$$

where the kinetic energy component is dependent on mass while the potential energy is dependent on position. The lineshape of a fully localized particle will reflect the probability distribution of the potential of the particle. If we treat the porphyrin chromophores as fully localized, the Soret bands of uncoupled molecules seen in Figure 4.2 will represent the probability distribution of the exciton potentials. During polariton formation the exciton couples to the cavity photon, forming a polariton. This polariton state has a "light-like" characteristic, which would impact the mass and position factors of the Hamiltonian in Eq. (4.6). If we wish to continue to relate the lineshape of the polariton to the disorder potential then we must account for the photonic character of the polariton state. The polariton lineshape as described by Whittacker *et al.* is $\Gamma_{lp} = \Gamma_{ex} \frac{|c_{ex}|^4}{|c_{ph}|^2}$, where $|c_{ex}|^2$ and $|c_{ph}|^2$ are the Hopfield coefficients representing the exciton and photon fractions respectively[39]. This suggests the linewidth will vary depending on the weight of the exciton and photonic components. We see that the lineshape becomes undefined when $|c_{ph}|^2 = 0$. However, this problem would only become relevant when $\theta$ would approach 90°, an angle we are not capable of observing.

While the model introduced by Whittacker *et al.* was designed to describe the behavior of a InGaAs quantum well polariton system we also observe a similar motional narrowing effect in our multi-layer porphyrin system, as seen in Figure 4.10. Most notably we observe the smallest linewidths when the exciton fraction is ∼0.5, as predicted by the Whittacker model. Another notable difference in our cavity design is that we use a multi-layer cav-

ity embedded with two nearly degenerate excitons, despite this we still observe lineshape narrowing near the resonant angle. Therefore, the delocalization of both excitons contributes to the lineshape of the LP. Delocalization of both excitons would provide for an efficient energy transfer system. DelPo, Scholes and coworkers concluded that while coupling a donor molecule to a cavity photon allows for efficient donor-acceptor interaction, the energy transfer rate is slowed due to the poor wave-function overlap between the localized acceptor and the delocalized polariton state[38]. Therefore, this limitation could be addressed by forming polaritons by using both, the donor and acceptor molecules. Interestingly, when examining the lower polariton lineshapes of a single layer cavity with a similar CuTPP concentration we do not observe narrowing of the lower polariton around the resonance angle, as seen in Figure 4.11. The motional narrowing model assumes a layered quantum well structure. However, in Figure 4.11 we analyzed a single layer micro-cavity. Therefore, the alternating layers of doped and undoped polymer within our cavity may be acting analogously to a quantum well micro-cavity, which is typically composed of layers of semiconductors with alternating band gaps.

## 4.6 Conclusion

In this study, we examined how the the hybridization of two quasi degenerate porphyrin excitons depends on their collective coupling to the photonic fluctuations in a single cavity mode. We find that despite their near degeneracy, the strong light-matter coupling of CuTPP and $H_2$TPP excitons does not lead to constant entanglement of these excitons[139]. We use a three oscillator Hamiltonian to model the energies and Hopfield coefficients of our samples. The model predicts the near absence of a photonic component in the middle

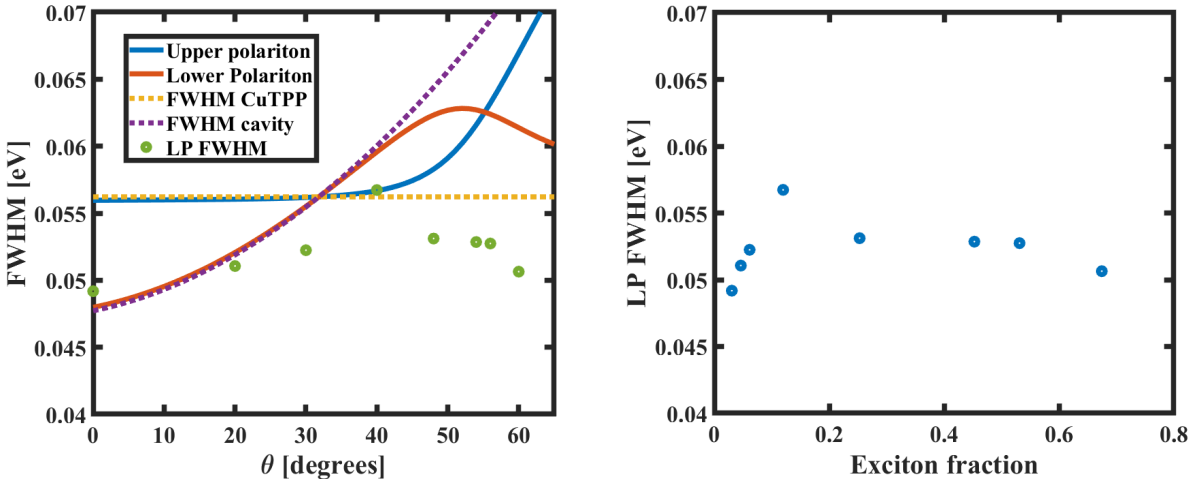


(a) (b)

Figure 4.11: a) Calculated and experimental linewidths of a single-layer micro-cavity doped with $\sim$ 1mM CuTPP. The cavity resonance angle is $\sim 55^{\circ}$. No noticeable narrowing near the resonance angle is observe. b) The experimentally measured lineshapes of a $\sim$ 1mM CuTPP cavity single layer cavity as a function of exciton fraction.

polariton, which may explain our inability to observe this polariton state. We also observe that the exciton fractions are maximally mixed near resonance, suggesting the potential energy surface of the middle polariton is a mixture of the two exciton states. Moreover, constructing a more positively tuned cavity appears to increase the CuTPP fraction of the middle polariton, this would suggest at large detunings the dynamics of the middle polariton would be very similar to that of a free space CuTPP molecule. Moreover, we predict that the excitonic portion of the lower polariton will be mostly $H_2$TPP. On the contrary, the upper polariton inherits the excitonic portion of the CuTPP. This contrasts with previous studies involving quasi-degenerate Frenkel-Wannier-Mott in which the excitonic fraction of the upper polariton was not distinguished between the two excitons[7].

We also examined the lineshapes of highly detuned multi-layer cavity samples. With the detuning from the Soret band being -184 meV and -86 meV. We found that the observed

lineshapes showed a minimum near the resonant angle and fit poorly with those predicted by the three oscillator Hamiltonian. This is likely because of the motional narrowing effect, described by Whittacker *et al*. Exciton lineshapes are subject to inhomogeneous broadening due to the individual molecules being embedded in a slightly different environment. The resulting transmission spectra would be an average of these individually embedded molecules, creating a broadening effect. However, during strong light-matter coupling polariton formation occurs. Unlike the excitons, polaritons are highly delocalized and are no longer "fixed" within the PMMA film. This delocalization decreases the importance the local environment has on the lineshape, causing a narrowing in the spectrum. In conclusion, this study indicates the need to carefully examine how the weight of the Hopfield coefficients in any experimentation. Even when forming polaritons from two nearly degenerate excitons the UP and LP inherit different excitonic characteristics. This must be accounted for if conducting an experiment to detect energy transfer between the polariton branches. Moreover, this study shows that while the simple three oscilator model is sufficient to describe the energy of the system, it fails to adequately predict the dynamics, which requires the motional narrowing model.

# CHAPTER 5 CONCLUDING REMARKS

## 5.1 Introduction

In my dissertation I address several gaps in the established literature. First, I address the apparent discrepancy between the so-called gap law and the observed internal conversion rate in a molecular polariton system. Second, I discuss the importance of the vibronic coupling mechanism in the photophysics of a polariton system. Lastly, I find that the coupling of two quasi-degenerate states does not lead to constant photon mediated entanglement of the two excitons. I will discuss future projects which can be undertaken to further expand on these conclusions.

## 5.2 Future work

Theoretical studies have predicted that polariton energy levels possess their own PES[27,28]. While we have shown evidence of this in Chapter 2, scientists have not yet mapped out the shape of a polariton PES. This may be possible with the use of vibrational coherence spectroscopy[143]. In summary a IR laser pulse is directed at the sample. This pulse creates a coherent ground state wave packet which will move along the ground state PES. Probing the ground state at different times as this wave packet evolves will, therefore, result in an energy map of the excited state PES. By using a probe which is centered around the energy of each polariton it would be possible to determine the shape of each polariton PES. Moreover, it was determined that the middle polariton of a quasi-degenerate state that is an equal mixture of both, CuTPP and $H_2$TPP at resonance. By using such a technique it would be possible to experimentally verify if the PES of this middle polariton is truly a mixture of the two excitons. The excitonic fraction of the middle polariton is also only expected to be

near equal when at the resonance angle. Probing such a sample at different angles could reveal how the exciton fraction impacts the shape of the PES.

While we have observed motional narrowing in or multi-layer cavity samples containing CuTPP and $H_2$TPP we did not observe a similar phenomenon in the single layer cavity containing only CuTPP. It may be that just as a InGaAs quantum well cavity requires multiple layers to observe the motional narrowing phenomenon, so does our multi-mode cavity. This hypothesis may be tested by using PVD to deposit thin layers of porphyrin/$SiO_2$ in order to form a quantum well cavity. If the properties of a polartion state depend on the number of layers coupling to the cavity photon it could be another variable to control the optical and chemical properties of a hybridized state.

Through this work we have relied on various porphyrin molecules to form the polariton states. Porphyrins serve as an excellent system for studying cavity polaritons due to both, their application as a model light harvesting molecule, and their large transition dipole moment which can easily couple to a cavity mode. Clearly however, porphyrins are not the only possible class of molecules from which cavity polaritons can be made. As long as a molecular transition has a sufficiently strong oscillator strength, and a photon of appropriate strength can be trapped within a cavity, the two components have a chance to form polariton states. Over the past decade scientists have made efforts to create more efficient light sources. In particular studies have been conducted to determine if polariton formation can increase the rate of reverse intersystem crossing (RISC) in order to enhance the efficiency of light emitting diodes[11,35]. These results have been ambiguous, with Stranius, Hertzog and Börjesson reporting an increase in the RISC rate. However, Cohen, Eizen and co-workers concluded that the RISC rate to the dark states will always dominate, negat-

ing any benefit of polariton formation. Manipulating RISC rates is not the only way to manipulate light emission. Recent studies using two dimensional hybrid perovskites have shown that they can be used as sources of white light[144,145]. The emission of the white light can be manipulated by changing the ratio of the halide within the sample, which in turn changes the energy of the free exciton[145]. Coupling the free exciton to a cavity photon may result in the ability to manipulate the photoluminescence of hybrid perovskites with more precision than with synthesis alone.

Lastly, efficient artificial photosynthesis has been perhaps one of the most sought after goals in the photochemical and photophyisics community[146]. We discussed the impacts of polariton formation on internal conversion in Chapter 2, which is an important step in the photosynthesis pathway. However, the photosynthesis process also involves electron transfer across numerous molecules. Therefore, there exists a need to understand how polariton formation impacts through-bond electron transfer. Porphyrin dimers would be an ideal model system to study such a process as the porphyrin macrocycle is central to the structure of the chlorophyll molecule.

## 5.3 Conclusion

Expressing rational control over photochemical and photophysical processes such as nonradiative relaxation remains an unfulfilled goal among the physical chemistry community. The ability to form cavity polaritons is one tool chemists can use to address this challenge. However, just as with any tool, it is first necessary to understand how to properly use it. Through this thesis I have discussed the importance of various factors such as interpolariton decay channels, the Hopfield coefficients, and Herzberg-Teller coupling

play in impacting the photophysics of a polariton system. The unique properties of these systems may lead to the development of artificial photosynthesis systems, improvements in current electron energy transfer mechanisms, as well as advancement in light emitting technologies.

APPENDIX A

## A.1 MATLAB code used to model cavity photon and DBR transmittance/reflectance

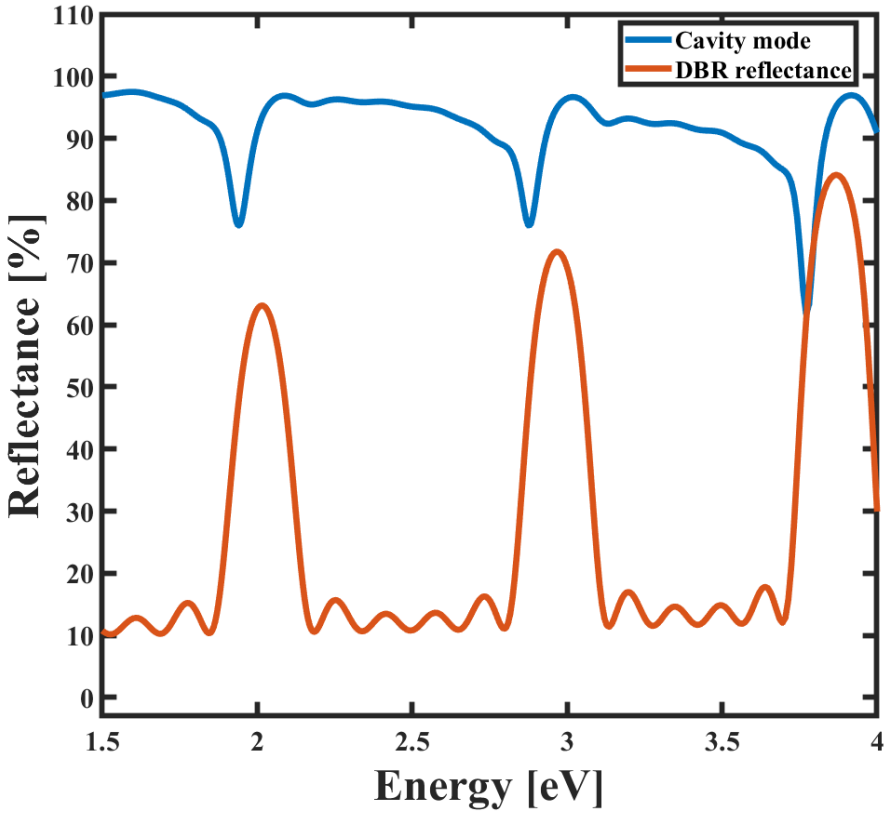


Figure A1: A model of the cavity mode and DBR reflectance produced from running the code presented in Appendix A.

Below is the code I used to model the behavior of a cavity photon in a Fabry-Perot cavity. This code is designed to model the behavior of a tri-layer cavity structure with two PMMA interfaces spaced by a layer of $SiO_2$. The two mirrors that are used in the model are a thin layer of aluminum and a DBR. To use the code the complex refractive index of aluminum must be imported in line 7. The information about the Al index was obtained from Rakic $et.al$[19]. The refractive index of $SiO_2$, $Si_3N_4$ and PMMA was accounted for in

lines 8-51 by using the Sellmeier equations[147–149]. To perform basic calculations using the model enter the thickness of the aluminum mirror in line 53. Enter the number of segments inside the DBR in line 72. Enter the thickness of the each DBR layer in lines 77 and 78. The cavity is designed to account for an odd number of DBR layers. To account for this odd layer enter its refractive index in line 83 and distance in line 86. Enter the estimated distance of the PMMA spacer layers in lines 87 and 88. Through my studies I noticed that the thickness of the layer closest to the aluminum was consistently $\sim$25 nm thicker than expected. This discrepancy is accounted for in the code. If desired, enter the angle of incidence in line 100. This code was designed to calculate the behavior of a cavity for TM polarization. Running the code will produce a result similar to figure A.1 from which the reflective behavior of the cavity mode and the DBR can be estimated. This input data was used to design the tri-layer CuTPP cavity in Chapter 3. Setting the parameters in lines 88 and 90 to zero will result in this code modeling the behavior of a single layer cavity.

```
1  %%%Generating code for cavity reflectance
2  %Design overview:
3  %[air-substrate Rn1]-[substrate-Si3N4 of DBR Rn2]-[First Si3N4 layer-DBR
4  %Rn3]-[DBR reflectance Rn4]-[mirror-coating Rn5]-[coating-spacer
5  %Rn6]-[spacer-coating %Rn7]-[Aluminum Rn8];
6  %%
7  load('Al_out')
8  %% Sellmeier for SiO2
9  B=0.6961663;
10 C=(0.0684043)^2;
```

```
11  B1=0.4079426;
12  C1=(0.1162414)^2;
13  B2=0.8974794;
14  C2=(9.896161)^2;
15  v1= (Alindex{:,1})';
16  v=v1*(10^12);
17  yy=((2.99*10^8)./(v*10^-6));
18  %yy=(.1:0.001:1);
19  %convert=2.99*10^8./(v);
20  %yy1=yy*10^12;
21  yy2=(yy).^2;
22  nn1=((B*yy2)./((yy2)-C));
23  nn1a=nn1+((B1*yy2)./((yy2)-C1));
24  nn1b=nn1a+((yy2*B2)./((yy2)-C2));
25  nindex1=sqrt(nn1b+1);
26  scale1=((2.99*10^8)./(v))*10^9;
27  % figure
28  % plot(scale1,nindex1);
29  %%
30  %%Sellmeier for Si3N4
31  D=3.0249;
32  E=(0.1353406)^2;
33  D1=40314;
34  E1=(1239.842)^2;
35  nn2=((D*yy2)./((yy2)-E));
36  nn2a=nn2+((D1*yy2)./((yy2)-E1));
37  %n3=n2+((x5*(y1.^2))./((y1.^2)-x6));
```

```
38  nindex2=sqrt(nn2a+1);
39  %%% Sellmeier for PMMA
40  F=0.99654;
41  G=(0.00787);
42  F1=0.18964;
43  G1=(0.02191);
44  F2=0.00411;
45  G2=(3.85727);
46  yy=((2.99*10^8)./(v*10^-6));
47  yy2=(yy).^2;
48  nn3=((F*yy2)./((yy2)-G));
49  nn3a=nn3+((F1*yy2)./((yy2)-G1));
50  nn3b=nn3a+((yy2*F2)/((yy2)-G2));
51  nindex3=(sqrt((nn3b+1)));
52
53  Al_d=(13*10^-9);
54
55  %Input the index of medium and substrate
56  nair=1;
57  ns=nindex1;
58
59  %Input the distance in meters light travels through each layer
60  dair=1;
61  ds=(1.1*10^-3);
62
63  %Input the speed of light and frequency range
64  c=(2.99*10^8);
```

```
65  lambdascale=(c./v)*10^9;
66  evscale=1240./lambdascale;
67  %Input the number of air/substrate interfaces.
68  N=1;
69  %
70  Ns=1; %Number of Si3N4/Bragg interfaces
71  %Input the number of segments used in the Bragg mirror
72  Nx=6;
73  %Input the index of refraction of each layer in the Bragg structure
74  n1=nindex1; %index SiO2
75  n2=nindex2; %index Si3N4
76  %Input the distance in meters light will travel through each layer
77  d1=(58.67*10^-9)*3; % thickness SiO2 (distance=lambda/4n)
78  d2=(58.67*10^-9)*3; %thickness Si3N4
79  %Input the number of coating/mirror interfaces
80  Nc=1;
81  %Input the index of refraction of the coating on top of the mirror and
        the
82  %mirror layer.
83  Na=n2;
84  npmma=nindex3;
85  %Input the distance in meters light will travel though each layer
86  dd=(58.67*10^-9)*3; % Thickness of first SiO2 layer, thickness calculated
        from FSR equation FSR=c/2nl, where n is the average index at 424nm
       and FSR is set at 707 THz.
87  dpmma=(147.7*10^-9); %Thickness of PMMA closest to DBR
88  dpmma2=(122.7*10^-9)+(25*10^-9); %Thickness of PMMA closest to Al
```

```
89 % Input thickness of spacer layer
90 di=(147.7*10^-9);
91 %% calcualte required length
92 FSR=2.971; % input the FSR in eV; (CuTPP abs=2.984 eV, TPP abs=2.958 eV);
93 plank=6.626*10^-34; %plank constant in Js
94 freq=(FSR*1.602*10^-19)./(plank);
95 avg_index=((npmma+n1+npmma)./3);
96 length=(c./(freq*2.*(avg_index))).*(1*10^9);
97 figure
98 plot(evscale,length)
99 %% angle
100 angle=0;
101 theta_1=(asind((nair*sind(angle))./ns)); %angle inside substrate (SiO2)
102 theta_2=(asind((ns.*sind(theta_1))./n2)); %angle inside n2 (Si3N4)
103 theta_3=(asind((n2.*sind(theta_2))./n1)); %angle inside n1 (SiO2)
104 theta_4=(asind((n1.*sind(theta_3))./n2)); %angle inside DBR
105 theta_5=(asind((n2.*sind(theta_4))./npmma)); %angle inside first PMMA
       layer
106 theta_6=(asind((npmma.*sind(theta_5))./n1)); %angle inside SiO2 spacer
107 theta_7=(asind((n1.*sind(theta_6))./npmma));%angle inside second PMMA
       layer
108 theta_1s=secd(theta_1);
109 theta_2s=secd(theta_2);
110 theta_3s=secd(theta_3);
111 theta_4s=secd(theta_4);
112 theta_5s=secd(theta_4);
113 theta_6s=secd(theta_5);
```

```
114 theta_7s=secd(theta_6);
115 theta_8s=secd(theta_7);
116 %%
117 %%Solving for the reflection of the air substrate intreface:
118 k=(2*pi)./(c./v);
119 f1xangle=nair.*k.*dair.*cosd(angle);
120 f2xangle=ns.*k.*ds.*cosd(theta_1);
121 f1angle=f1xangle+f2xangle;
122 f2angle=f1xangle-f2xangle;
123
124 na=(((nair.*secd(angle))+(ns.*theta_1s)).^2)./(4.*(nair.*secd(angle)).*(
        ns.*theta_1s));
125 na1=(((ns.*theta_1s)-(nair.*secd(angle)).^2)./(4.*(nair.*secd(angle)).*(
        ns.*theta_1s)));
126
127 t1=(na.*cos(f1angle))-(na1.*cos(f2angle));
128 p=(acos(t1));
129 er=(sin(N.*p))./(sin(p));
130
131 %One segment reflection from Fresnel used to compute R: n2-n1/n2+n1
132 R1=(((nair.*secd(angle))-(ns.*theta_1s))./((nair.*secd(angle))+(nair.*
        theta_1s))).^2;
133 Rn1=((er.*conj(er).*R1))./((1-R1)+(er.*conj(er).*R1));
134 %figure
135 %plot (v,Rn1)
136 %%
137 %Solving for the reflection of the subtrate and the first Si3N4 layer of
```

```
138 %Bragg mirror
139 k=(2*pi)./(c./v);
140 f3xangle=ns.*k.*ds.*cosd(theta_1); %incidance angle inside SiO2 substrate
141 f4xangle=n2.*k.*d2.*cosd(theta_2); %angle inside Si3N4 layer
142 f3angle=f3xangle+f3xangle;
143 f4angle=f3xangle-f4xangle;
144
145 na2=(((ns.*theta_1s)+(n2.*theta_2s)).^2)./(4.*(ns.*theta_1s).*(n2.*
        theta_2s));
146 na3=(((ns.*theta_1s)-(n2.*theta_2s)).^2)/(4.*(ns.*theta_1s).*(n2.*
        theta_2s));
147 t10=(na2.*cos(f3angle))-(na3.*cos(f4angle));
148 p10=(acos(t10));
149 er10=(sin(Ns.*p10))./(sin(p10));
150
151 %One segment reflection from Fresnel used to compute R: n2-n1/n2+n1
152 R2=(((ns.*theta_1s)-(n2.*theta_2s))./((ns.*theta_1s)+(n2.*theta_2s))).^2;
153 Rn2=((er10.*conj(er10).*R2))./((1-R2)+(er10.*conj(er10).*R2));
154 %%
155 %Solving for the reflection between the first Si3n4 layer and Bragg
156 %structure
157 f5xangle=n2.*k.*d2.*cosd(theta_2);%angle inside Si3N4
158 f6xangle=n1.*k.*d1.*cosd(theta_3);% angle inside SiO2
159 f5angle=f5xangle+f6xangle;
160 f6angle=f5xangle-f6xangle;
161
162 nh=(((n2.*theta_2s)+(n1.*theta_3s)).^2)/(4*((n1.*theta_3s).*(n2.*theta_2s
```

```
    )));
163 nh1=(((n2.*theta_2s)-(n1.*theta_3s)).^2)/(4*((n1.*theta_3s).*(n2.*
    theta_2s)));
164
165 t7=(nh.*cos(f5angle))-(nh1.*cos(f6angle));
166 p7=acos(t7);
167 erh=(sin(Nc*p7))./(sin(p7));
168 %Reflection of a single segment from Fresnel:
169 R3=(((n2.*theta_2s)-(n1.*theta_3s))./((n2.*theta_2s)+(n1.*theta_3s))).^2;
170 Rn3=((erh.*conj(erh).*R3))./((1-R3)+(erh.*conj(erh).*R3));
171 %%
172 %%Solving for the reflection of the bragg structure
173 f7xangle=n1.*k.*d1.*cosd(theta_3);
174 f8xangle=n2.*k.*d2.*cosd(theta_4);
175 f7angle=f7xangle+f8xangle;
176 f8angle=f7xangle-f8xangle;
177
178 nb=(((n1.*theta_3s)+(n2.*theta_4s)).^2)./(4*(n1.*theta_3s).*(n2.*theta_4s
    ));
179 nb1=(((n2.*theta_4s)-(n1.*theta_3s)).^2)./(4*(n1.*theta_3s).*(n2.*
    theta_4s));
180
181 t2=(nb.*cos(f7angle))-(nb1.*cos(f8angle));
182 p2=acos(t2);
183 erb=((sin(Nx*p2)))./((sin(p2)));
184 %One segment reflection from Fresnel:
185 R4=(((n2.*theta_4s)-(n1.*theta_3s))./((n2.*theta_4s)+(n1.*theta_3s))).^2;
```

```
186 Rn4=((erb.*conj(erb).*R4))./((1-R4)+(erb.*conj(erb).*R4));
187 %%
188 %Solving for the mirror-coating interface
189 f9xangle=Na.*k.*dd.*cosd(theta_4);
190 f10xangle=npmma.*k.*dpmma.*cosd(theta_5);
191 f9angle=f9xangle+f10xangle;
192 f10angle=f9xangle-f10xangle;
193
194 nc=(((Na.*theta_4s)+(npmma.*theta_5s)).^2)./(4*(npmma.*theta_5s).*(Na.*
        theta_4s));
195 nc1=(((Na.*theta_4s)-(npmma.*theta_5s)).^2)./(4*(npmma.*theta_5s).* (Na.*
        theta_4s));
196
197 t3=(nc.*cos(f9angle))-(nc1.*cos(f10angle));
198 p3=acos(t3);
199 erx=(sin(Nc*p3))./(sin(p3));
200 %One segment reflection from Fresnel:
201 R5=(((npmma.*theta_5s)-(Na.*theta_4s))./((npmma.*theta_5s)+(Na.*theta_4s)
        )).^2;
202 Rn5=((erx.*conj(erx).*R5))./((1-R5)+(erx.*conj(erx).*R5));
203 %figure
204 %plot (v,Rn3)
205 %%
206 %Solving for coating SiO2 spacer interface
207 f11xangle=npmma.*k.*dpmma2.*cosd(theta_5);
208 f12xangle=n1.*k.*di.*cosd(theta_6);
209 f11angle=f11xangle+f12xangle;
```

```
210 f12angle=f11xangle-f12xangle;
211
212 nc3=(((n1.*theta_6s)+(npmma.*theta_5s)).^2)./(4*(npmma.*theta_5s).*(n1.*
        theta_6s));
213 nc4=(((n1.*theta_6s)-(npmma.*theta_5s)).^2)./(4*(npmma.*theta_5s).* (n1.*
        theta_6s));
214
215 t4=(nc3.*cos(f11angle))-(nc4.*cos(f12angle));
216 p4=acos(t4);
217 tt1=sin(Nc*p4);
218 tt2=sin(p4);
219 era=sin(Nc.*p4)./(sin(p4));
220 %One segment reflection from Fresnel:
221 R6=(((npmma.*theta_5s)-(n1.*theta_6s))./((npmma.*theta_5s)+(n1.*theta_6s)
        )).^2;
222 Rn6=((era.*conj(era).*R6))./((1-R6)+(era.*conj(era).*R6));
223 %%
224 %Solving for SiO2 coating interface;
225 f13xangle=n1.*k.*di.*cosd(theta_6);
226 f14xangle=npmma.*k.*dpmma2.*cosd(theta_7);
227 f13angle=f13xangle+f13xangle;
228 f14angle=f14xangle-f14xangle;
229
230 nc5=(((n1.*theta_6s)+(npmma.*theta_7s)).^2)./(4*(npmma.*theta_7s).*(n1.*
        theta_6s));
231 nc6=(((n1.*theta_6s)-(npmma.*theta_7s)).^2)./(4*(npmma.*theta_7s).*(n1.*
        theta_6s));
```

```
232
233 t5=(nc5.*cos(f13angle))-(nc6.*cos(f14angle));
234 p5=acos(t5);
235 erc=(sin(Nc*p5))./(sin(p5));
236 %One segment reflection from Fresnel:
237 R7=(((npmma.*theta_7s)-(n1.*theta_6s))./((npmma.*theta_7s)+(n1.*theta_6s)
        )).^2;
238 Rn7=((erc.*conj(erc).*R7))./((1-R7)+(erc.*conj(erc).*R7));
239 %%
240 xi=100:1:1000; %NOTE: RANGE IS NOW 100:1000
241 yi0=spline(Alindex{:,1},Alindex{:,2},xi);
242 yi1=spline(Alindex{:,1},Alindex{:,3},xi);
243
244 scale2=((2.99*10^8)./(v));
245
246 nindex_Al_nn=(Alindex{:,2}); %n of Al;
247 nindex_Al=(Alindex{:,3}); %k of Al;
248 n_Al=nindex_Al_nn';
249 k_Al=nindex_Al';
250 nf_Al=n_Al+1i*k_Al;
251 theta_8=(asind((npmma.*sind(theta_7))./nf_Al)); %angle inside Al
252 theta_8s=secd(theta_8);
253 Al_df=Al_d.*theta_8s;
254 tAl=4*(n_Al-1i*k_Al).*1.*exp(-1i*(n_Al-1i*k_Al)*(2*pi).*Al_df./scale2)
        ./((1+(n_Al-1i*k_Al)).^2-((1-(n_Al-1i*k_Al)).^2).*exp(-2*1i*(n_Al-1i*
        k_Al)*(2*pi).*Al_df./scale2));
255 alpha=(4*pi*nindex_Al')./(lambdascale*10^-9);
```

```
256  testx=(Alindex{:,1})';
257  testy=exp(-alpha.*Al_d);
258
259  Rn8c=1-testy;
260
261  T_4=tAl.*conj(tAl);
262  Rn8=1-T_4;
263  %%
264  %Total reflectance
265  R1t=(1-Rn1).*(1-Rn2);
266
267  R1r=(1-R1t);
268  R2t=(1-R1r).*(1-Rn3);
269
270  R2r=(1-R2t);
271  R3t=(1-R2r).*(1-Rn4);
272
273  R3r=(1-R3t);
274  R4t=(1-R3r).*(1-Rn5);
275
276  R4r=(1-R4t);
277  R5t=(1-R4r).*(1-Rn6);
278
279  R5r=(1-R5t);
280  R6t=(1-R5r).*(1-Rn7);
281
282  R6r=(1-R6t);
```

```
283  R7t=(1-R6r).*(1-Rn8);
284
285  Rfinal=(1-R7t);
286 %% Fabry Perot intensity
287  Io=1;
288  c1=(2.99*10^8)./(((npmma+npmma+nindex1)./3));
289  r1=(R3r);
290  r2=(Rn8);
291  lossF=(1./(2*((npmma+n1+npmma)/3).*(dpmma+dpmma2+di))).*log(1./(r2.*r1));
292  F=(2*pi)./(log(1./(r1.*r2))); %Finesse
293  ra=exp(-2.*lossF.*(dpmma+dpmma2+di));
294  vm1=npmma.*dpmma.*cosd(theta_5);
295  vm2=n1.*di.*cosd(theta_6);
296  vm3=npmma.*dpmma2.*cosd(theta_7);
297  vm=c./(2.*(vm1+vm2+vm3));
298  tmax1=1;
299  tmax2=((tmax1))./((1-ra).^2);%max intensity
300 M=max(tmax2);
301  Mx=(1-Rfinal);
302  M2=1-(min(Mx));
303  Rfinalc=Rfinal(1:1,700:901);
304  v1c=v1(1:1,700:901);
305  Rfinalcc=Rfinal(1:1,870:899);
306  v1cc=v1(1:1,870:899);
307
308  Tfinal=(M2.*(tmax2)./(1+((2*F/pi).^2.*sin(pi*v./vm).^2))./M);
309
```

```
310 NormR=Rfinalc./max(Rfinalc);
311 minT=min(Tfinal);
312 NormT=Tfinal./max(Tfinal)-minT;
313 df=Rfinal-(NormT.*max(Rfinalc));
314
315 dft=df+abs(min(df));
316 dfc=(dft-max(dft))+1;
317 %% reflectance of DBR and pulse intensity
318 Qfactor=(2*pi*freq)./(c.*lossF);
319
320 x=(100:1:1000);
321 x1=x*(10^12);
322 x0=(180*10^12);
323 time=(35*10^-15);
324 S1=-1*((2*pi^2)*(time^2)*(x0-v).^2);
325 S2=(exp(S1));
326 figure
327 yyaxis left
328 plot (v1,S2)
329 yyaxis right
330 plot (v1,R3r)
331 yyaxis right
332 ylabel ('Reflectance')
333 yyaxis left
334 ylabel ('Spectral intensity')
335 xlim([100 1000])
336 yyaxis left
```

```
337 ylim([0,1.3])
338 yyaxis right
339 ylim([0,1.3])
340 title ('Reflectance of mirror and intensity of pulse')
341 xlabel ('Frequency (Thz)')
342 legend('Intensity of pump pulse','Reflectance of DBR')
343 %%
344 figure
345 box on
346 hold on
347 plot(evscale,dfc*100)
348 plot(evscale,R3r*100)
349 xlabel ('Energy (eV)')
350 ylabel ('Reflectance (%)')
351 xlim([0.9 3.7])
352 ylim([-3 110])
353 legend('Cavity mode','DBR reflectance')
```

## A.2 Preparation, storage, and transportation of polymer/chromophore solutions

The Fabry-Perot cavity structures were manufactured at the University of Michigan's Lurie Nanofabrication Facility (LNF). Prior to manufacturing the samples must be properly prepared and characterized. First, porphyrns were dissolved in PMMA-A4 solution to give proper concentration. Typical concentrations ranged from 0.5-2 mM. In order to ensure the porphyrin dissolved in the PMMA solution they were submerged in a water bath at $\sim$70 °C

for 10 minutes and sonicated for 2 minutes. In order to determine the thickness of the DBR and PMMA layers approximately ten 1.5x1.5 cm pieces of silicone wafer are needed. These were obtained from MTI corporation and cut using a diamond pen. The 1x1 inch fused silica substrates which serve as the base of the cavity structures were also obtained from MTI corporation. Once the silicone wafers are cut and the PMMA/chromophore solution is mixed, they are transported to the LNF using a secondary container lined with aluminum foil. The fused silica substrates are transported in their factory packaging and only opened inside the clean room. Manufacturing the cavities will require one pair of metallic tweezers in order to work with hot plates, and one pair of plastic tweezers to handle the finished cavity. When the solutions are not in use they were stored in the laboratory refrigerator.

## A.3 Steps in fabrication of DBR structures

The DBR structures were fabricated with plasma enhanced chemical vapor deposition available on the Plasmatherm 790 tool at the LNF. After ensuring the instrument is in the CVD mode (right chamber) select the `L_OX200` process and run it on an empty chamber for 3 minutes. Vent the chamber and load the silicone substrate. Pump the chamber down and select the `L_OX200` process again. Select a deposition time in order to deposit a specific $SiO_2$ thickness based on the MATLAB code above. The deposition rates for each process will be listed near the instrument. After the process has completed vent the chamber and retrieve the sample in order to measure the new thickness. The chamber must be pumped down if unattended for a prolonged period of time. Using the Woollam-2000 ellipsometer measure the thickness of your sample. If the thickness is undesirable calculate the deposition rate based on the measured thickness and deposition time, and repeat the process with a new

piece of silicone wafer. When the required time to deposit the correct thickness of $SiO_2$ is determined select the `L_NIT200` process. Repeat the procedure in order to determine the time required to deposit the correct thickness of $Si_3N_4$. Once the deposition time that gives the desired $SiO_2$ and $Si_3N_4$ thickness is obtained using the silicone wafers begin the deposition process using the fused silica substrates. The number of DBR segments to achieve a specific reflectance is set in line 72 of the MATLAB code. Alternate the `L_OX200` and `L_NIT200` processes to deposit the required number of layers to construct the DBR structure.

## A.4 Steps in fabricating the spacer layers

The Fabry-Perot structure is spaced by two spun coated layers of PMMA and a layer of $SiO_2$. While creating the cavities ensure to leave one blank DBR sample which was not spun coated to serve as a backrgound sample. I used the E-Beam spinner/Hot plate bench located in the LNF to spin coat a layer of PMMA on top of the DBR structures. The thickness of the coating determines the detuning of the cavity structure. To estimate the needed thickness I first determine the energy of the Soret band and set it as the FSR. I calculated the required thickness using the relation $FSR = \frac{c}{2nd}$[16]. A plot of thickness to energy is generated in line 98 of the MATLAB code. A reference PMMA spin curve is provided in the LNF. Using this reference set the spin speed to give the desired thickness. I begin the spin process by first cleaning my silicone wafer by running the spin process with isopropyl alcohol. The wafer is then dried using the provided $N_2$ gas. This cleans the wafer and ensures the spin process works correctly. I deposit $\sim$ 400 microleters of PMMA solution and spin coat the wafer. The sample is then cured at 180 °C for 3 minutes. I

use the Woollam-2000 ellipsometer to check the thickness of the spun coated sample. The speed is adjusted higher if it is too thick, and lower if it is too thin. Once I determine that the thickness of the PMMA on the silicone wafer is correct I proceed to spin coat the DBR substrates using the same procedure.

The next step is to use the Angstrom Engineering Evaporator to deposit a layer of $SiO_2$ on top of the spun coated PMMA. Secure the samples to the instrument holder using double sided tape. Vent the chamber and ensure the correct deposition material is inserted. Pump the chamber to 4 $\mu$Torr. Select pocket 8 ($SiO_2$) in the deposition software. Set the desired thickness and deposition rate and press start. After deposition is completed allow the instrument to cool for 2 minutes before venting. Once vented, check the crystal life prior and replace any crystals whose life is below 75$\%$. Before spin coating the final PMMA layer it is necessary to allow the sample at least 2 days to properly cure after completing the $SiO_2$ deposition. I use the vacuum oven to store the samples while heating at 100 °F for 10 hours, the sample is then allowed to sit for at room temperature for an additional 48 hours. After the samples have been allowed to cure the top layer of PMMA is spun coated as described before. Through experimental measurements the layer closest to the aluminum has been found to be consistently $\sim$ 25 nm thicker than expected, this discrepancy must be accounted for while spin coating. Lastly, a layer of aluminum is deposited using the Enerjet Evaporator. To use the Enerjet, vent the instrument chamber and check the crystal life. Replace the crystal if the life is over 20$\%$. Secure the samples to the sample holder with double sided tape and pump down to 200 mTorr. Use the ION button to turn on the cryopump and pump down to 2 $\mu$Torr. Program the desired thickness using the XTC control. Press the PROG key, scroll through the program menu with the PROCESS key

until Film Thickness is displayed. Enter the desired number. Scroll to Film Number to select film 5 (Aluminum) and ensure no other films are selected. Set the Dep Rate to 4 Angstroms/second. When the correct chamber pressure has been reached press start to begin deposition. Wait 5 minutes after deposition for the instrument to cool and vent the chamber.

## A.5 Characterization of transmission spectra

To ensure polaritons are successfully formed I use angle resolved transmission spectroscopy. The collection optics of the spectrometer are custom built to fit experimental needs. The distance required to collimate a light beam is estimated with the thin lens equation[21]. A Thorlabs PBS251 beamsplitter is used to separate horizontal and vertical polarizations. To begin taking data insert a DBR sample into the holder attached to the Thorlabs rotation mount. This sample will serve as the background measurement. Turn on the Thorlabs SLS204 deuterium lamp and allow it to warm up. Open the OceanView software on the computer and select "create new application" in the file menu. Select transmission and set the integration time to 20 ms and number of scans to 250. Select next and acquire the reference spectrum. Select next again and block the lamp to acquire the background spectrum. Click finish and unblock the lamp. Insert the sample of interest to take its spectrum. The "convert active spectrum to overlay" button saves the spectrum on the screen, while the "save graph to files" feature saves the data. This procedure must be repeated at each angle and for each cavity sample which has a unique DBR.

**APPENDIX B**

## B.1 Sample catalog

Table B.1: List of tri-layer cavity samples created while studying the photophysics of CuTPP, ZnTPP, and $H_2$TPP. The approximate detunining from the Soret band is recorded to catalog the samples.

| Sample ID | Sample composition | Approximate detuning |
|---|---|---|
| 1 | DBR/PMMA/$SiO_2$/PMMA/Al | -184 meV |
| 2 | DBR/CuTPP/$SiO_2$/$H_2$TPP/Al | -184 meV |
| 3 | DBR/CuTPP/$SiO_2$/$H_2$TPP/Al | -184 meV |
| 4 | DBR/CuTPP/$SiO_2$/$H_2$TPP/Al | -184 meV |
| 4 | DBR/CuTPP/$SiO_2$/$H_2$TPP/Al | -184 meV |
| 5 | DBR only | N/A |
| 13 | DBR/PMMA/$SiO_2$/PMMA/Al | +4 meV |
| 14 | DBR/CuTPP/$SiO_2$/$H_2$TPP/Al | +4 meV |
| 15 | DBR/CuTPP/$SiO_2$/$H_2$TPP/Al | +4 meV |
| 16 | DBR/CuTPP/$SiO_2$/$H_2$TPP/Al | +4 meV |
| 17 | DBR/CuTPP/$SiO_2$/$H_2$TPP/Al | +4 meV |
| 18 | DBR only | N/A |
| 19 | DBR/PMMA/$SiO_2$/PMMA/Al | -120 meV |
| 20 | DBR/PMMA/$SiO_2$/$H_2$TPP/Al | -120 meV |
| 21 | DBR/PMMA/$SiO_2$/$H_2$TPP/Al | -120 meV |
| 22 | DBR/PMMA/$SiO_2$/$H_2$TPP/Al | -120 meV |
| 23 | DBR only | N/A |
| 24 | DBR/PMMA/$SiO_2$/PMMA/Al | +30 meV |
| 25 | DBR/PMMA/$SiO_2$/$H_2$TPP/Al | +30 meV |

| | | |
|---|---|---|
| 26 | DBR/PMMA/$SiO_2$/$H_2$TPP/Al | +30 meV |
| 27 | DBR/PMMA/$SiO_2$/$H_2$TPP/Al | +30 meV |
| 28 | DBR only | N/A |
| 29 | DBR only | N/A |
| 30 | DBR/CuTPP/$SiO_2$/$H_2$TPP/Al | +74 meV |
| 31 | DBR/CuTPP/$SiO_2$/$H_2$TPP/Al | +74 meV |
| 32 | DBR/CuTPP/$SiO_2$/$H_2$TPP/Al | +74 meV |
| 33 | DBR/PMMA/$SiO_2$/PMMA/Al | +74 meV |
| 34 | DBR/PMMA/$SiO_2$/$H_2$TPP/Al | +74 meV |
| 35 | DBR/PMMA/$SiO_2$/$H_2$TPP/Al | +74 meV |
| 36 | DBR/PMMA/$SiO_2$/$H_2$TPP/Al | +74 meV |
| 37 | DBR/CuTPP/$SiO_2$/PMMA/Al | -42 meV |
| 38 | DBR/CuTPP/$SiO_2$/PMMA/Al | -42 meV |
| 39 | DBR/CuTPP/$SiO_2$/PMMA/Al | -42 meV |
| 40 | DBR only | N/A |
| 41 | DBR only | N/A |
| 42 | DBR/PMMA/$SiO_2$/PMMA/Al | +161 meV |
| 43 | DBR/CuTPP/$SiO_2$/PMMA/Al | +161 meV |
| 44 | DBR/CuTPP/$SiO_2$/PMMA/Al | +161 meV |
| 45 | DBR/CuTPP/$SiO_2$/PMMA/Al | +161 meV |
| 1x | DBR only | N/A |
| 2x | DBR/$H_2$TPP/$SiO_2$/CuTPP/Al | -86 meV |
| 3x | DBR/$H_2$TPP/$SiO_2$/CuTPP/Al | -86 meV |
| 4x | DBR/$H_2$TPP/$SiO_2$/CuTPP/Al | -86 meV |
| 5x | DBR/PMMA/$SiO_2$/PMMA/Al | -86 meV |

| | | |
|---|---|---|
| Q | DBR/PMMA/$SiO_2$/PMMA/Al | -95 meV |
| R | DBR/CuTPP/$SiO_2$/CuTPP/Al | -95 meV |
| S | DBR/CuTPP/$SiO_2$/CuTPP/Al | -95 meV |
| T | DBR only | N/A |

Table B.2: List of tri-layer cavity samples possessing a stop band below the area of the Soret band.

| **Sample ID** | **Sample composition** | **FSR** |
|---|---|---|
| 1 | DBR only | N/A |
| 2 | DBR/PMMA/$SiO_2$/PMMA/Al | 0.942 eV |
| 3 | DBR/CuTPP/$SiO_2$/PMMA/Al | 0.942 eV |
| 4 | DBR/CuTPP/$SiO_2$/PMMA/Al | 0.942 eV |
| E | DBR only | N/A |
| F | DBR/PMMA/Al | 1.874 eV |
| G | DBR/CuTPP/Al | 1.874 eV |
| H | DBR/CuTPP/PMMA/Al | 1.874 eV |
| I | DBR only | N/A |
| J | DBR/PMMA/$SiO_2$/PMMA/Al | 0.951 eV |
| K | DBR/CuTPP/$SiO_2$/PMMA/Al | 0.951 eV |
| L | DBR/CuTPP/$SiO_2$/PMMA/Al | 0.951 eV |
| M | DBR/PMMA/$SiO_2$/PMMA/Al | 0.978 |
| N | DBR/CuTPP/$SiO_2$/$H_2$TPP/Al | 0.978 eV |
| O | DBR/CuTPP/$SiO_2$/$H_2$TPP/Al | 0.978 eV |

## B.2 Dispersive cavity linewidth model

The following is the cavity dispersion model used to estimate the dispersion of a cavity photon in Chapter 4. Note that the cavity photon FWHM is dispersive. This is likely due to the reflectivity changes in the DBR with respect to angle. When calculating the FWHM using the Hamiltonian model I attempt to account for the variation of the cavity photon FWHM by experimentally measuring an empty cavity at different angles, using a Lorentzian function $\frac{A}{(x-p)^2+(w^2)}+(mx+b)$ to estimate the FWHM $w$, and fitting the resulting FWHMs to a polynomial. The form of the polynomial is,

$$f = p_1 x^2 + p_2 x + p_3 \tag{B.1}$$

where $p_1 = 6.535 \times 10^{-6}$, $p_2 = 2,535 \times 10^{-5}$, and $p_3 = 0.04544$. A similar procedure was completed to estimate the cavity photon behavior of Cavity 2x, using the values $p_1 = 4.952 \times 10^{-6}$, $p_2 = 0.0001096$, and $p_3 = 0.04772$.

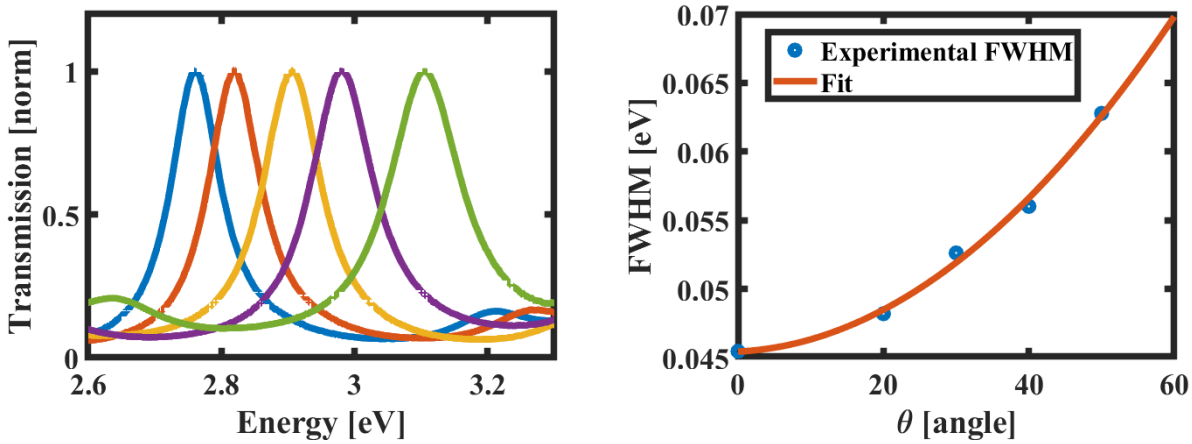


(a) (b)

Figure B1: a) Experimental FWHM for cavity 4 measured at angle 0 (blue), angle 20 (red), angle 30 (yellow), angle 40 (purple), and angle 50 (green). b) Fitted model as compared to experimentally measured cavity FWHM.

**APPENDIX C**

## C.1 Predicted Vibronic Polariton Energetics for 5 Disordered Molecules

Eq. (C1) shows the matrix form of the Hamiltonian we use to model the energetics of cavity polaritons formed from 5 molecules possessing different eigenenergies distributed normally around central values consistent with those characterizing the UV-vis absorption spectrum of polymer-embedded copper (II) tetraphenyl porphyrin molecules. We denote these differences in the matrix of Eq. (C1) with superscripts $(n)$ for the nth molecule.

$$\hat{H} = \begin{bmatrix} \hbar\omega_1^{(1)} & V_{HT} & 0 & 0 & 0 & 0 & 0 & 0 & 0 & 0 & V_{LM} \\ V_{HT} & \hbar\omega_2^{(1)} & 0 & 0 & 0 & 0 & 0 & 0 & 0 & 0 & 0 \\ 0 & 0 & \hbar\omega_1^{(2)} & V_{HT} & 0 & 0 & 0 & 0 & 0 & 0 & V_{LM} \\ 0 & 0 & V_{HT} & \hbar\omega_2^{(2)} & 0 & 0 & 0 & 0 & 0 & 0 & 0 \\ 0 & 0 & 0 & 0 & \hbar\omega_1^{(3)} & V_{HT} & 0 & 0 & 0 & 0 & V_{LM} \\ 0 & 0 & 0 & 0 & V_{HT} & \hbar\omega_2^{(3)} & 0 & 0 & 0 & 0 & 0 \\ 0 & 0 & 0 & 0 & 0 & 0 & \hbar\omega_1^{(4)} & V_{HT} & 0 & 0 & V_{LM} \\ 0 & 0 & 0 & 0 & 0 & 0 & V_{HT} & \hbar\omega_2^{(4)} & 0 & 0 & 0 \\ 0 & 0 & 0 & 0 & 0 & 0 & 0 & 0 & \hbar\omega_1^{(5)} & V_{HT} & V_{LM} \\ 0 & 0 & 0 & 0 & 0 & 0 & 0 & 0 & V_{HT} & \hbar\omega_2^{(5)} & 0 \\ V_{LM} & 0 & V_{LM} & 0 & V_{LM} & 0 & V_{LM} & 0 & V_{LM} & 0 & \hbar\omega_c \end{bmatrix}, \quad \text{(C.1)}$$

where $V_{HT}$ is the non-Condon vibronic coupling given by Eq. (3.1) of the main manuscript and $V_{LM}$ is the light-matter interaction Hamiltonian for each molecule. For simplicity, we presume each of the five molecules possess the vibronic and light-matter coupling strength.

Figure C1 shows the full energetics of the states we find following a single diagonaliza-

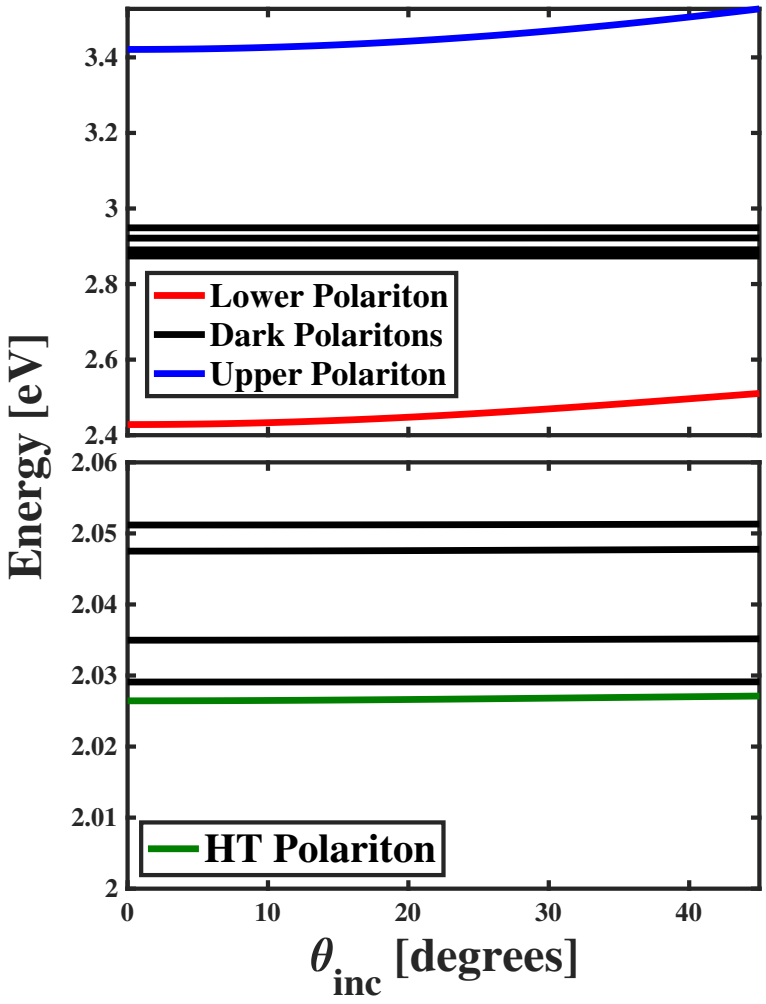


Figure C1: Top panel: dispersive energetics of lower (red), dark (black), and upper (blue) cavity polaritons states near the energy of the $|1\rangle$ state described in the text of the main manuscript file found from diagonalizing the matrix in Eq. (C1). Bottom panel: dispersive energetics of Herzberg-Teller (green) and dark (black) cavity polaritons states near the energy of the $|2\rangle$ state described in the text of the main manuscript file found from diagonalizing the matrix in Eq. (C1).

tion of the matrix in Eq. (C1). We found the states shown in figure C1 using $V_{LM} = 0.5$ eV and $V_{HT} = 0.1$ eV.

## C.2 Cavity Fabrication Methods

**Non-cavity Sample**: Commercially available CuTPP was dissolved in 10 mL PMMA-A4 solution obtained from Kayaku advanced materials. The final solution concentration was approximately 2 mM. The mixture was sonicated for 2 minutes and placed in a water bath at 70 °C for 10 minutes. The sample fabrication was completed at the University of Michigan's Lurie Nanofabrication Facility. Using the E-Beam spinner/Hot plate-21 approximately 400 microliters of the prepared PMMA solution was deposited on a fused silica substrate and spun coated using the static disperse method at 4000 rpm for 45 seconds. The silica substrates were obtained from MTI Corporation. The film was cured at 180 °C for 3 minutes. The spun coated substrates were next secured to the Enerjet evaporator instrument holder with polyimide tape. The vacuum chamber was pumped down to approximately 2 micro-Torr to begin aluminum PVD deposition. A layer of 15 nm of Al was deposited on the film at a rate of 4 Angstroms per second.

**Single Layer Cavity Polariton Sample**: Commercially available CuTPP was dissolved in 10 mL PMMA-A4 solution obtained from Kayaku advanced materials. The final solution concentration was approximately 2 mM. The mixture was sonicated for 2 minutes and placed in a water bath at 70 °C for 10 minutes. To make the Distributed Bragg Reflectors 1x1 inch fused silica substrates were obtained from MTI corporation to serve as substrates. Using the Plasmatherm-790 tool located in the University of Michigan's Lurie Nanofabrication facility 11 alternating layers of $SiO_2$ and $Si_3N_4$ were deposited on the silica substrates at a thickness of 58.29 nm. Using the E-Beam spinner/Hot plate-21 the CuTPP doped PMMA solution was spun coated unto the Distributed Bragg Reflectors at 6000 rpm. The

film was cured at 180 °C for 3 minutes. The film speed was selected to produce a final Fabry-Perot structure with a thickness of 145 nm. The spun coated substrates were next secured to the Enerjet evaporator instrument holder with polyimide tape. The vacuum chamber was pumped down to approximately 2 micro-Torr to begin aluminum PVD deposition. A layer of 15 nm of Al was deposited on the film at a rate of 4 Angstroms per second.

**Multiple Layer Cavity Polariton Sample 1**: Commercially available CuTPP was dissolved in 10 mL PMMA-A4 solution obtained from Kayaku advanced material. The final solution concentration was approximately 1 mM. The mixture was sonicated for 2 minutes and placed in a water bath at 70 °C for 10 minutes. To make the Distributed Bragg Reflectors, 1x1 inch fused silica substrates were obtained from MTI corporation to serve as substrates. Using the Plasmatherm-790 tool located in the University of Michigan's Lurie Nanofabrication facility 11 alternating layers of $SiO_2$ and $Si_xN_y$ were deposited on the silica substrates at a thickness of 58.29 nm. Using the E-Beam spinner/Hot plate-21 the CuTPP doped PMMA solution was spun coated unto the Distributed Bragg Reflectors at 4300 rpm. The film was cured at 180 °C for 3 minutes. The spun coated substrates were next secured to the AE evaporator instrument holder using polyimide tape. The instrument was pumped down to 3 micro-Torr. A layer of approximately 144.4 nm of $SiO_2$ was deposited at a rate of 3 Angstroms per second. After the deposition of $SiO_2$ the films were heated to 100 °F for 10 hours and allowed to sit for an additional 2 days to ensure any stresses in the film due to the PVD process were dissipated. Next, a layer of PMMA doped with 30% toluene was spun coated unto the samples using the static disperse method at 5500 rpm for 45 seconds. The samples were cured at 180 °C for 3 minutes. The samples were then secured

to the Enerjet evaporator instrument holder with polyimide tape. The vacuum chamber was pumped down to approximately 2 micro-Torr to begin aluminum PVD deposition. A layer of 13 nm of Al was deposited on the film at a rate of 4 Angstroms per second. This deposition process produced a Fabry-Perot cavity with a final thickness of approximately 433.2 nm.

**Multiple Layer Cavity Polariton Sample 2**: Commercially available CuTPP was dissolved in 10 mL PMMA-A4 solution obtained from Kayaku advanced material. The final solution concentration was approximately 1 mM. The mixture was sonicated for 2 minutes and placed in a water bath at 70 °C for 10 minutes. To make the Distributed Bragg Reflectors 1x1 inch fused silica substrates were obtained from MTI corporation. Using the Plasmatherm-790 tool located in the University of Michigan's Lurie Nanofabrication facility 11 alternating layers of $SiO_2$ and $Si_xN_y$ were deposited on the silica substrates at a thickness of 174.79 nm. Using the E-Beam spinner/Hot plate-21 the CuTPP doped PMMA solution was spun coated unto the Distributed Bragg Reflectors at 4300 rpm. The film was cured at 180 °C for 3 minutes. The spun coated substrates were next secured to the AE evaporator instrument holder using polyimide tape. The instrument was pumped down to 3 micro-Torr. A layer of approximately 143.7 nm of $SiO_2$ was deposited at a rate of 3 Angstroms per second. After the deposition of $SiO_2$ the films were heated to 100 °F for 10 hours and allowed to sit for an additional 2 days to ensure any stresses in the film due to the PVD process were dissipated. Next, a layer of PMMA doped with 30% toluene was spun coated from the 1 mM CuTPP/PMMA solution unto the samples using the static disperse method at 5500 rpm for 45 seconds. The samples were cured at 180 °C for 3 minutes. The samples were then secured to the Enerjet evaporator instrument holder with

polyimide tape. The vacuum chamber was pumped down to approximately 2 micro-Torr to begin aluminum PVD deposition. A layer of 13 nm of Al was deposited on the film at a rate of 4 Angstroms per second. This deposition process produced a Fabry-Perot cavity with a final thickness of approximately 431.1 nm.

## C.3 Spectroscopic Methods

To carry out steady-state transmission measurements of the cavity samples, we used a fiber-coupled deuterium lamp whose output beam we collimated with free space optics that polarized the incident light fields in the plane of our optical table. We took the resulting beam and focused it onto the cavity samples, collected the transmitted light, and coupled it into fiber-based spectrometer (OceanOptics OceanFX). We measured steady-state transmission spectra at different incident angles so we could estimate the dispersive energies of the cavity mode peaks. In addition, we tested for the anti-crossing behavior of the cavity polariton states in the transmission spectra of those samples we designed to maintain strong light-matter coupling. To more clearly isolate the properties of the polariton peaks in our measured transmission spectra, we fabricated DBR structures without converting them into complete cavity samples. Using these DBR blanks as backgrounds for our steady-state spectra allowed us to reduce significant portions of the baseline on the polariton transmission spectra stemming from the highly dispersive reflectivity of the TM mode of the DBR structure. We used a Horiba XPLoRA PLUS micro-spectrometer affixed with a 10x microscope objective to collect steady-state photoluminescence measurements on all the samples described in this study following excitation at 2.33 eV. We made all the reported measurements using a back-scattering geometry.

## C.4 Schematics of Cavity Structures

Figs. S2-S5 show schematic representations of the structures of the cavity samples we fabricated and characterized spectroscopically in the main manuscript. Each schematic shows both the pertinent layers of the resonator structures and the standing cavity modes we propose dominate the behavior of those samples. For example, we propose only the single, $\lambda/2$ standing mode dominates the behavior of the single layer cavity and Purcell cavity samples, which we show in Figs. S2 and S5, respectively. In contrast, we propose both the $3\lambda/2$ and $\lambda$ standing modes of the multi-layer cavity 1 and multi-layer cavity 2 samples participate in their photophysics, which we show in the resonator schematics of Figs. S3 and S4. More specifically, the dispersion curves in figure 3.3 of the main manuscript indicate the photons of the $3\lambda/2$ modes of the multi-layer cavity 1 and multi-layer cavity 2 samples couple strongly to the Soret transition of CuTPP while $\lambda$ mode couples weakly to the light emission from both HT polaritons and uncoupled molecules within the cavity.

## C.5 Cavity Transmission Spectra

The left and right panels of Figure C5 show the transmission spectra through the SL cavity and ML cavity 1 samples, respectively, for incident angles that result in resonant coupling between the Soret transition of CuTPP and the highest energy photon modes supported by each resonator structure. These spectra indicate the clear indications of strong light-matter coupling necessary for cavity polariton formation, which are consistent with the dispersive behavior shown in the panels of Figure 3.3 of the main document.

Figure C6 shows the transmission spectra of the ML cavity 2 sample in the region near

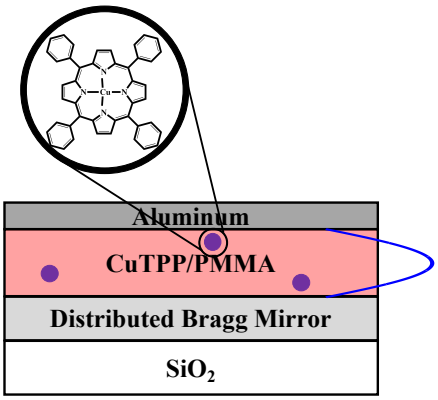


Figure C2: Schematic representation of the single mode cavity sample used to form cavity polaritons from copper (II) tetraphenylporphyrin. The cavity was designed to support a single mode at ∼435 nm for normally incident light.

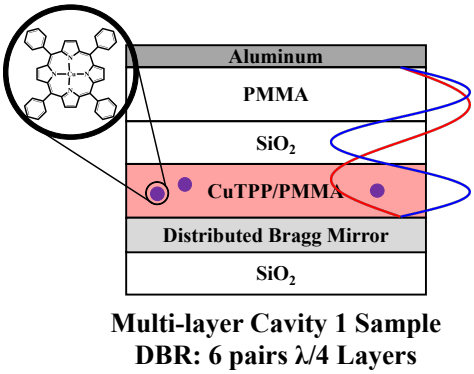


Figure C3: Schematic representation of the multimode cavity 1 sample used to form cavity polaritons from copper (II) tetraphenylporphyrin. The distributed Bragg mirror in this sample was formed from 11 alternating layers of $SiO_2$ and $Si_3N_4$ were deposited on the silica substrates at a thickness of 58.29 nm.The cavity was designed to support a single, high-Q mode at ∼435 nm for normally incident light, but also supports an additional low-Q cavity mode at ∼650 nm, as shown in Fig. 3.2 of the main manuscript.

the Soret transition of CuTPP for several incident angles. For angles that cause the photon to possess energy below that of the molecule's Soret transition, like 24°, we find the presence of a single, predominant peak in the transmission spectrum. As we increase the angle, we find the overall transmission become attenuated relative to low angle measurements and the single peak splits into two peaks, which is most clearly seen for an incident angle

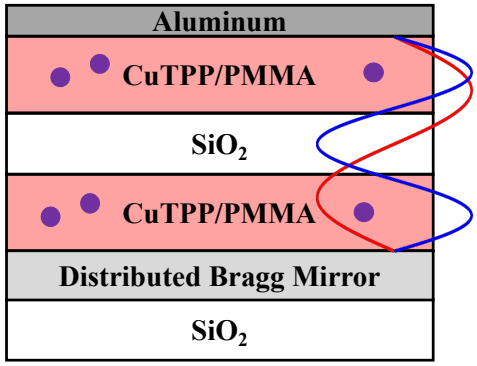


Figure C4: Schematic representation of the multimode cavity 2 sample used to form cavity polaritons from copper (II) tetraphenylporphyrin. The distributed Bragg mirror in this sample was formed from 11 alternating layers of $SiO_2$ and $Si_3N_4$ were deposited on the silica substrates at a thickness of 174.79 nm.The cavity was designed to support high-Q cavity modes at ∼430 nm and ∼640 nm for normally incident light, as shown in Fig. 3.2 of the main document.

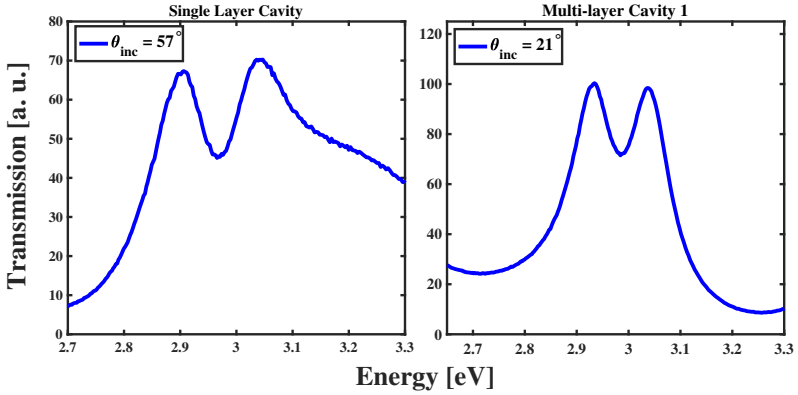


Figure C5: Left panel: transmission spectrum of the single layer cavity polariton sample for an incident angle of 57°, which enforces resonant coupling between the photons of the $\lambda/2$ resonator mode and the Soret transition of CuTPP. Right panel: transmission spectrum of the multi-layer cavity polariton 1 sample for an incident angle of 25°, which enforces resonant coupling between the photons of the $3\lambda/2$ resonator mode and the Soret transition of CuTPP.

of 29°.

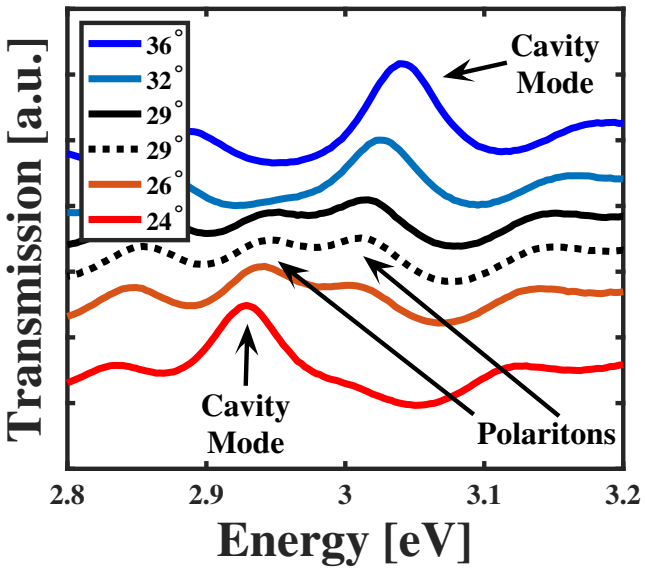


Figure C6: Angularly resolved transmission spectra of the multi-layer cavity 2 sample showing the avoided crossing of the cavity photon mode and the CuTPP Soret transition resulting in the appearance of two distinct peaks at $\theta_{inc} = 29°$. At angles below this value we only observe the peak due to transmission through the cavity at energies below the Soret transition of CuTPP. In addition, At angles above 29° we only observe the peak due to transmission through the cavity at energies above the Soret transition of CuTPP.

## C.6 Modeling Photoluminescence Spectra

We modeled the temperature-dependent PL spectra of single layer and multi-layer 2 CuTPP cavity polariton samples using the following equation,

$$I_T(E) = A_1 \text{exp}\left(-\left[(E-E_1)/(2\Delta E_1)\right]^2\right) + \frac{A_2}{(E-E_2)^2 + \Delta E_2^2} \tag{C.2}$$
$$+A_3(T)\text{exp}\left(-\left[(E-E_3)/(2\Delta E_3)\right]^2\right) + A_4(T)\text{exp}\left(-\left[(E-E_4)/(2\Delta E_4)\right]^2\right),$$

where we assign the light emission intensity corresponding to the first and second terms of Eq. (C2) as stemming from the Q states of those CuTPP molecules decoupled from the cavity photons and the HT polaritons, respectively. We assign the third and fourth terms

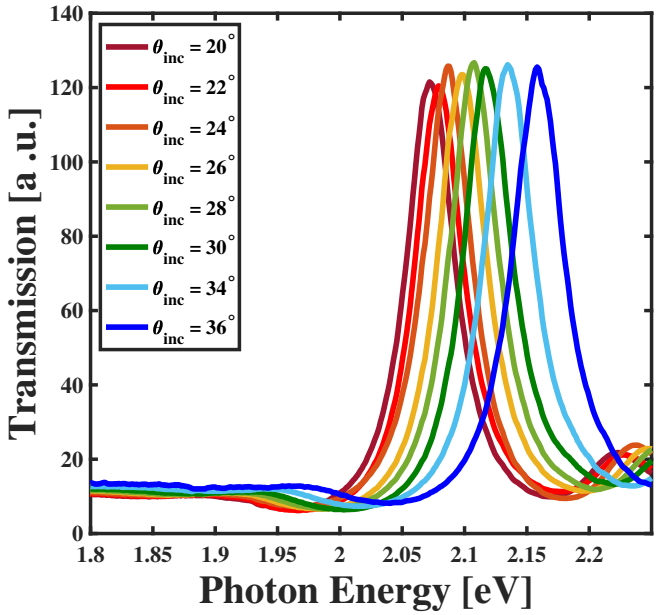


Figure C7: Angularly resolved transmission spectra in the region around the $\nu_2$ cavity mode of the multi-layer cavity 2 sample showing the dispersive behavior of the energy of this resonator mode. In addition to the clear appearance of the $\nu_2$, we do not observe any distinct cavity modes at energies near 1.9 eV that would overlap with light emission from the $^2$Q state of CuTPP or Herzberg-Teller polaritons formed using this molecular chromophore.

of Eq. (C2) as stemming from light emission from the $^2T_1$ and $^4T_1$ states of CuTPP, which are known to possess temperature-dependent lifetimes.

Figure C8 compares the PL spectra we measure emitted by the SL cavity and ML cavity 1 samples to the model in Eq. (C2) showing the ability of this model to predict all the salient features of the experimental spectra. Fits were produced using a nonlinear least squares regression to Eq. (C2) as implemented with the curve fitting toolbox of Matlab.

Table C.1: Quantitative comparison between the intensities, energies, and widths of the light emission peaks in the vicinity of that of the $^2$Q state of CuTPP. *indicates assumed value based on measurements made on control samples.

| **Sample** | $A_1$ [cnts.] | **$E_1$ [eV]** | **$\Delta E_1$ [meV]** | $A_2$ [cnts.] | **$E_2$ [eV]** | **$\Delta E_2$ [meV]** |
|---|---|---|---|---|---|---|
| SL Cavity | 1970±155 | 1.895* | 83±2.3 | 1.058±0.22 | 1.883±0.001 | 19.9±1.8 |
| ML Cavity 1 | 2522±290 | 1.899±0.005 | 88.8±5.4 | 1.24±0.33 | 1.882±0.001 | 15.6±1.9 |

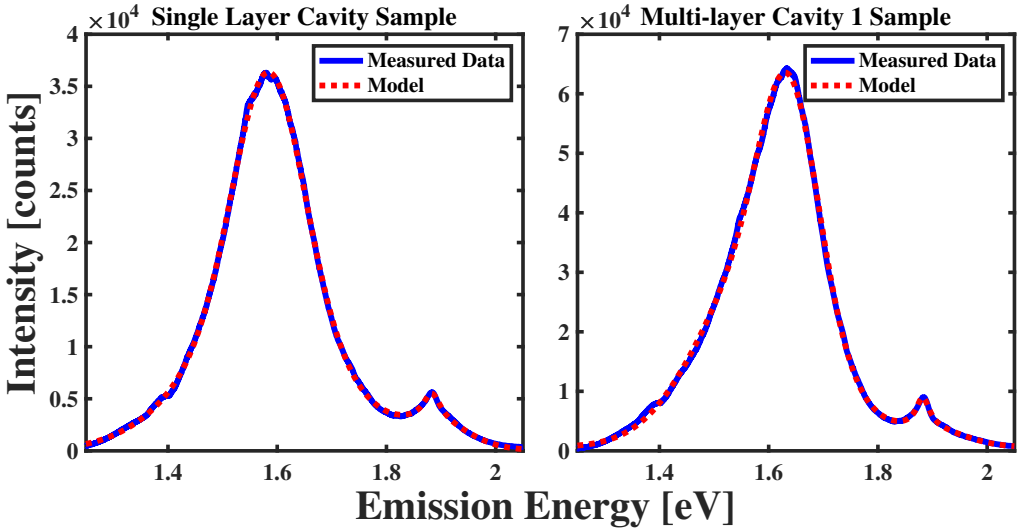


Figure C8: Comparison between the photoluminescence spectrum of the single layer cavity (left panel) and multi-layer cavity 1 (right panel) polariton samples measured experimentally (solid blue) to a model found using Eq. (C2) through nonlinear least squares regression analysis.

Table C.2: Quantitative comparison between the intensities, energies, and widths of the light emission peaks in the vicinity of that of the $^2T_1$ and $^4T_1$ states of CuTPP.

| **Sample** | $A_3$ [cnts.] | $\mathbf{E_3}$ **[eV]** | $\mathbf{\Delta E_3}$ **[meV]** | $A_4$ [cnts.] | $\mathbf{E_4}$ **[eV]** | $\mathbf{\Delta E_4}$ **[meV]** |
|---|---|---|---|---|---|---|
| SL Cavity | 23780±270 | 1.585±0.001 | 90.1±1.5 | 12540±260 | 1.576±0.001 | 187.6±1.5 |
| ML Cavity 1 | 34940±490 | 1.638±0.001 | 74.8±0.6 | 30810±410 | 1.586±0.001 | 155.8±0.8 |

We show a similar comparison between experimental and modeled PL spectra of the ML cavity 2 sample using Eq. (C2) in the bottom left panel of figure 3.5 in the main document. We report the parameters found from the regression analysis of the two highest energy features in each spectrum with their estimated uncertainties in Table C1. In addition, we report the parameters found from the regression analysis of the two lowest energy features in each spectrum with their estimated uncertainties in Table C2.

## C.7 ML Cavity 2 Samples

The photoluminescence of the ML cavity 2 sample present more challenges in fitting due to the complex background stemming from the additional photonic stopband in the

spectral vicinity of the molecule's light emission spectrum. To fit the spectrum of this sample we used the following equation,

$$I_{\text{ML Cavity 2}}(E) = \frac{A_1}{(E-E_1)^2 + [\Delta E_1/2]^2} + \frac{A_2}{(E-E_2)^2 + [\Delta E_2/2]^2} \tag{C.3}$$
$$+A_3(T)\text{exp}\left(-\left[(E-E_3)/(2\Delta E_3)\right]^2\right) + A_4(T)\text{exp}\left(-\left[(E-E_4)/(2\Delta E_4)\right]^2\right)$$
$$+A_5(T)\text{exp}\left(-\left[(E-E_5)/(2\Delta E_5)\right]^2\right) + A_6(T)\text{exp}\left(-\left[(E-E_6)/(2\Delta E_6)\right]^2\right)$$
$$+A_7(T)\text{exp}\left(-\left[(E-E_7)/(2\Delta E_7)\right]^2\right),$$

where the first two terms are assigned to the $\nu_2$ cavity and HT polariton peaks of the ML cavity 2 sample PL spectrum, as described in the text of the main manuscript. The remaining terms represented the light emission of the triplet states of CuTPP filtered by the Bragg peaks of the distributed Bragg reflector present on the red-side of the optic's photonic stopband. Figure C9 shows the comparison between PL spectrum of the ML cavity 2 sample and the fit we find using Eq.(C3), demonstrating the adequate agreement between the two.

## C.8 Temperature Dependence of ML Cavity 2 Sample Photoluminescence Spectra

Our measured photoluminescence spectra from the different CuTPP-cavity samples feature several temperature-dependent changes in peak characteristics such as intensity and central energy. We fit the temperature dependent PL spectra of the ML cavity 2 sample with Eq. (C3) and extracted the positions of the $\nu_2$ cavity mode and HT polariton peaks as a function of temperature. In addition, we extracted the position of the light emission of

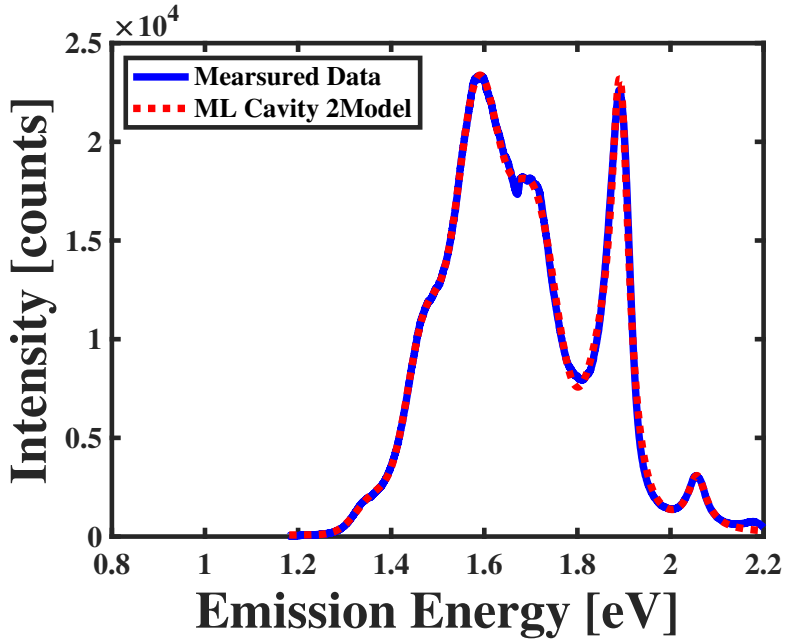


Figure C9: Comparison between the photoluminescence spectrum of the multi-layer cavity 2 polariton sample measured experimentally at 373 K(solid blue) to a model found using Eq. (C3) through nonlinear least squares regression analysis.

the $^2$Q state of CuTPP in the non-cavity sample as a function similar temperature. Figure C10 compares the different temperature-dependent trends and shows the peaks of the ML cavity 2 sample shift in a qualitatively different manner than the $^2$Q peak in the non-cavity sample. This difference suggests entirely different physical processes drive the peak shifts in the different samples.

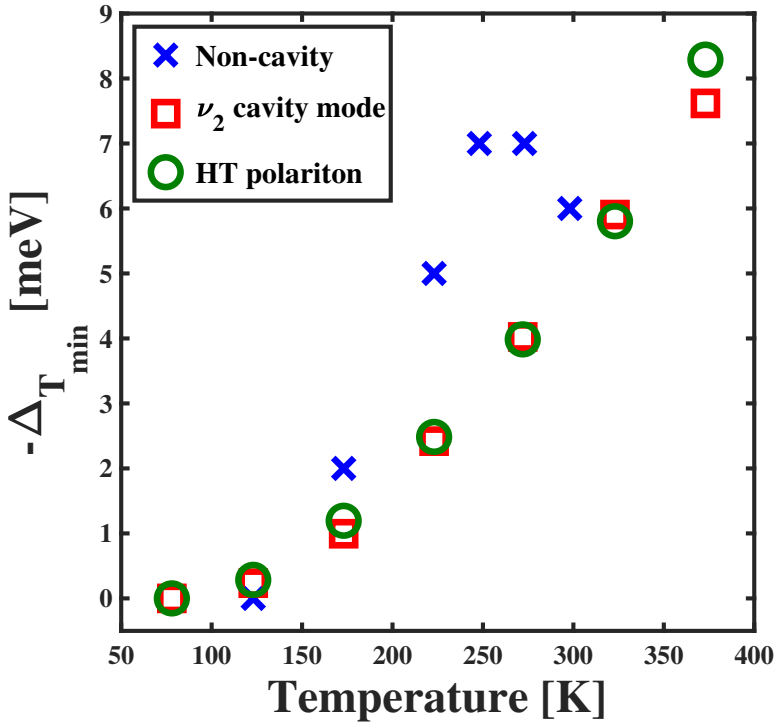


Figure C10: Comparison between the photoluminescence spectrum of the single layer cavity and multi-layer cavity 1 polariton samples measured experimentally (solid blue) to a model found using Eq. (C2) through nonlinear least squares regression analysis.

**REFERENCES**

[1] A. M. Kelley, *Condensed-phase molecular spectroscopy and photophysics*. John Wiley & Sons, 2012.

[2] T. W. Ebbesen, "Hybrid Light-Matter States in a Molecular and Material Science Perspective," *Acc. Chem. Res.*, vol. 49, no. 11, pp. 2403–2412, 2016.

[3] T. Schwartz, J. A. Hutchison, J. Léonard, C. Genet, S. Haacke, and T. W. Ebbesen, "Polariton dynamics under strong light–molecule coupling," *ChemPhysChem*, vol. 14, no. 1, pp. 125–131, 2013.

[4] A. G. Avramenko and A. S. Rury, "Quantum control of ultrafast internal conversion using nanoconfined virtual photons," *J. Phys. Chem. Lett.*, vol. 11, no. 3, pp. 1013–1021, 2020.

[5] A. G. Avramenko and A. S. Rury, "Interrogating the structure of molecular cavity polaritons with resonance raman scattering: An experimentally motivated theoretical description," *The Journal of Physical Chemistry C*, vol. 123, no. 50, pp. 30551–30561, 2019.

[6] J. A. Hutchison, T. Schwartz, C. Genet, E. Devaux, and T. W. Ebbesen, "Modifying chemical landscapes by coupling to vacuum fields," *Angew. Chem., Int. Ed.*, vol. 51, no. 7, pp. 1592–1596, 2012.

[7] M. Slootsky, X. Liu, V. M. Menon, and S. R. Forrest, "Room temperature frenkel-wannier-mott hybridization of degenerate excitons in a strongly coupled microcavity," *Phys. Rev. Lett.*, vol. 112, p. 076401, Feb 2014.

[8] R. Holmes and S. Forrest, "Strong exciton-photon coupling and exciton hybridiza-

tion in a thermally evaporated polycrystalline film of an organic small molecule," *Physical review letters*, vol. 93, no. 18, p. 186404, 2004.

[9] D. M. Coles, Y. Yang, Y. Wang, R. T. Grant, R. A. Taylor, S. K. Saikin, A. Aspuru-Guzik, D. G. Lidzey, J. K.-H. Tang, and J. M. Smith, "Strong coupling between chlorosomes of photosynthetic bacteria and a confined optical cavity mode," *Nature communications*, vol. 5, no. 1, pp. 1–9, 2014.

[10] M. Skolnick, T. Fisher, and D. Whittaker, "Strong coupling phenomena in quantum microcavity structures," *Semiconductor Science and Technology*, vol. 13, no. 7, p. 645, 1998.

[11] K. Stranius, M. Hertzog, and K. Börjesson, "Selective manipulation of electronically excited states through strong light–matter interactions," *Nat. Comm.*, vol. 9, no. 1, p. 2273, 2018.

[12] A. Graf, *Strong light-matter interactions and exciton-polaritons in carbon nanotubes*. PhD thesis, 2019.

[13] J. Hopfield, "Theory of the contribution of excitons to the complex dielectric constant of crystals," *Physical Review*, vol. 112, no. 5, p. 1555, 1958.

[14] D. Lidzey, J. Wenus, D. Whittaker, G. Itskos, P. Stavrinou, D. Bradley, and R. Murray, "Hybrid polaritons in strongly coupled microcavities: experiments and models," *Journal of luminescence*, vol. 110, no. 4, pp. 347–353, 2004.

[15] M. A. Robb and M. Olivucci, "Photochemical processes: potential energy surface topology and rationalization using vb arguments," *Journal of Photochemistry and Photobiology A: Chemistry*, vol. 144, no. 2-3, pp. 237–243, 2001.

[16] B. E. Saleh and M. C. Teich, *Fundamentals of Photonics*. John Wiley & Sons, Ltd, NY NY, 2019.

[17] H. Kogelnik and T. Li, "Laser beams and resonators," *Applied optics*, vol. 5, no. 10, pp. 1550–1567, 1966.

[18] X. Zhong, T. Chervy, L. Zhang, A. Thomas, J. George, C. Genet, J. A. Hutchison, and T. W. Ebbesen, "Energy transfer between spatially separated entangled molecules," *Angewandte Chemie International Edition*, vol. 56, pp. 9034–9038, 2019/07/19 2017.

[19] A. D. Rakić, "Algorithm for the determination of intrinsic optical constants of metal films: application to aluminum," *Applied optics*, vol. 34, no. 22, pp. 4755–4767, 1995.

[20] H. Bennett, R. Peck, D. Burge, and J. Bennett, "Formation and growth of tarnish on evaporated silver films," *Journal of applied physics*, vol. 40, no. 8, pp. 3351–3360, 1969.

[21] J. Peatross and M. Ware, "Physics of light and optics: a free online textbook," in *Laser Science*, p. JWA64, Optical Society of America, 2010.

[22] D. M. Beggs, *Computational studies of one and two-dimensional photonic microstructures*. PhD thesis, Durham University, 2006.

[23] C. Weisbuch, M. Nishioka, A. Ishikawa, and Y. Arakawa, "Observation of the coupled exciton-photon mode splitting in a semiconductor quantum microcavity," *Physical Review Letters*, vol. 69, no. 23, p. 3314, 1992.

[24] R. André, D. Heger, L. S. Dang, and Y. M. d'Aubigné, "Spectroscopy of polaritons in cdte-based microcavities," *Journal of crystal growth*, vol. 184, pp. 758–762, 1998.

[25] M. Pieczarka, P. Podemski, A. Musiał, K. Ryczko, G. Sęk, J. Misiewicz, F. Langer, S. Höfling, M. Kamp, and A. Forchel, "Gaas-based quantum well exciton-polaritons beyond 1 $\mu$m.," *Acta Physica Polonica, A.*, vol. 124, no. 5, 2013.

[26] D. G. Lidzey, D. Bradley, M. Skolnick, T. Virgili, S. Walker, and D. Whittaker, "Strong exciton–photon coupling in an organic semiconductor microcavity," *Nature*, vol. 395, no. 6697, pp. 53–55, 1998.

[27] J. Galego, F. J. Garcia-Vidal, and J. Feist, "Suppressing photochemical reactions with quantized light fields," *Nature Communications*, vol. 7, no. 1, pp. 1–6, 2016.

[28] J. Feist, J. Galego, and F. J. Garcia-Vidal, "Polaritonic chemistry with organic molecules," *ACS Photon.*, vol. 5, no. 1, pp. 205–216, 2018.

[29] R. Houdré, R. P. Stanley, and M. Ilegems, "Vacuum-field rabi splitting in the presence of inhomogeneous broadening: Resolution of a homogeneous linewidth in an inhomogeneously broadened system," *Phys. Rev. A*, vol. 53, pp. 2711–2715, Apr 1996.

[30] D. Whittaker, P. Kinsler, T. Fisher, M. Skolnick, A. Armitage, A. Afshar, M. Sturge, and J. Roberts, "Motional narrowing in semiconductor microcavities," *Physical review letters*, vol. 77, no. 23, p. 4792, 1996.

[31] J.-H. Song, Y. He, A. V. Nurmikko, J. Tischler, and V. Bulovic, "Exciton-polariton dynamics in a transparent organic semiconductor microcavity," *Phys. Rev. B*, vol. 69, p. 235330, Jun 2004.

[32] S. Wang, T. Chervy, J. George, J. A. Hutchison, C. Genet, and T. W. Ebbesen, "Quantum yield of polariton emission from hybrid light-matter states," *The journal of physical chemistry letters*, vol. 5, no. 8, pp. 1433–1439, 2014.

[33] V. M. Agranovich, M. Litinskaia, and D. G. Lidzey, "Cavity polaritons in microcavities containing disordered organic semiconductors," *Phys. Rev. B*, vol. 67, p. 085311, Feb 2003.

[34] T. Virgili, D. Coles, A. M. Adawi, C. Clark, P. Michetti, S. K. Rajendran, D. Brida, D. Polli, G. Cerullo, and D. G. Lidzey, "Ultrafast polariton relaxation dynamics in an organic semiconductor microcavity," *Phys. Rev. B: Condens. Matter Mater. Phys.*, vol. 83, p. 245309, Jun 2011.

[35] E. Eizner, L. A. Martínez-Martínez, J. Yuen-Zhou, and S. Kéna-Cohen, "Inverting singlet and triplet excited states using strong light-matter coupling," *Science Advances*, vol. 5, no. 12, 2019.

[36] R. Englman and J. Jortner, "The energy gap law for radiationless transitions in large molecules," *Molecular Physics*, vol. 18, no. 2, pp. 145–164, 1970.

[37] D. G. Lidzey, A. M. Fox, M. D. Rahn, M. S. Skolnick, V. M. Agranovich, and S. Walker, "Experimental study of light emission from strongly coupled organic semiconductor microcavities following nonresonant laser excitation," *Phys. Rev. B: Condens. Matter Mater. Phys.*, vol. 65, p. 195312, May 2002.

[38] C. A. DelPo, S.-U.-Z. Khan, K. H. Park, B. Kudisch, B. P. Rand, and G. D. Scholes, "Polariton decay in donor–acceptor cavity systems," *The Journal of Physical Chemistry Letters*, vol. 12, no. 40, pp. 9774–9782, 2021.

[39] D. Whittaker, P. Kinsler, T. Fisher, M. Skolnick, A. Armitage, A. Afshar, J. Roberts, G. Hill, and M. Pate, "Motional narrowing in semiconductor microcavities," *Superlattices and microstructures*, vol. 22, no. 1, pp. 91–96, 1997.

[40] D. M. Coles, N. Somaschi, P. Michetti, C. Clark, P. G. Lagoudakis, P. G. Savvidis,

and D. G. Lidzey, "Polariton-mediated energy transfer between organic dyes in a strongly coupled optical microcavity.," *Nature materials*, vol. 13, no. 7, pp. 712–9, 2014.

[41] J. Galego, F. J. Garcia-Vidal, and J. Feist, "Cavity-Induced Modifications of Molecular Structure in the Strong-Coupling Regime," *Phys. Rev. X*, vol. 5, no. 4, p. 041022, 2015.

[42] E. Orgiu, J. George, J. A. Hutchison, E. Devaux, J. F. Dayen, B. Doudin, F. Stellacci, C. Genet, J. Schachenmayer, C. Genes, G. Pupillo, P. Samorì, and T. W. Ebbesen, "Conductivity in Organic Semiconductors Hybridized with the Vacuum Field," *Nat. Mater.*, vol. 14, pp. 1123–1130, 2015.

[43] F. C. Spano, "Optical Microcavities Enhance the Exciton Coherence Length and Eliminate Vibronic Coupling in J-aggregates," *J. Chem. Phys.*, vol. 142, no. 18, p. 184707, 2015.

[44] M. Kowalewski, K. Bennett, and S. Mukamel, "Cavity Femtochemistry: Manipulating Nonadiabatic Dynamics at Avoided Crossings," *J. Phys. Chem. Lett.*, vol. 7, no. 11, pp. 2050–2054, 2016.

[45] F. Herrera and F. C. Spano, "Cavity-Controlled Chemistry in Molecular Ensembles," *Phys. Rev. Lett.*, vol. 116, p. 238301, 2016.

[46] M. Kowalewski, K. Bennett, and S. Mukamel, "Non-adiabatic dynamics of molecules in optical cavities," *J. Chem. Phys.*, vol. 144, no. 5, p. 054309, 2016.

[47] K. Bennett, M. Kowalewski, and S. Mukamel, "Novel Photochemistry of Molecular Polaritons in Optical Cavities," *Faraday Discussions*, vol. 194, p. 10.1039/C6FD00095A, 2016.

[48] X. Zhong, T. Chervy, S. Wang, J. George, A. Thomas, J. A. Hutchison, E. Devaux, C. Genet, and T. W. Ebbesen, "Non-radiative energy transfer mediated by hybrid light-matter states," *Angewandte Chemie International Edition*, vol. 55, pp. 6202–6206, 2019/07/19 2016.

[49] R. F. Ribeiro, L. A. Martínez-Martínez, M. Du, J. Campos-Gonzalez-Angulo, and J. Yuen-Zhou, "Polariton chemistry: Controlling molecular dynamics with optical cavities," *Chemical Science*, vol. 9, pp. 6325–6339, 2018.

[50] L. A. Martínez-Martínez, M. Du, R. F. Ribeiro, S. Kéna-Cohen, and J. Yuen-Zhou, "Polariton-assisted singlet fission in acene aggregates," *J. Phys. Chem. Lett.*, vol. 9, no. 8, pp. 1951–1957, 2018.

[51] M. Du, L. A. Martínez-Martínez, R. F. Ribeiro, Z. Hu, V. M. Menon, and J. Yuen-Zhou, "Theory for polariton-assisted remote energy transfer," *Chem. Sci.*, vol. 9, pp. 6659–6669, 2018.

[52] R. Sáez-Blázquez, J. Feist, A. I. Fernández-Domínguez, and F. J. García-Vidal, "Organic polaritons enable local vibrations to drive long-range energy transfer," *Phys. Rev. B: Condens. Matter Mater. Phys.*, vol. 97, p. 241407, Jun 2018.

[53] A. M. Berghuis, A. Halpin, Q. Le-Van, M. Ramezani, S. Wang, S. Murai, and J. Gómez Rivas, "Enhanced delayed fluorescence in tetracene crystals by strong light-matter coupling," *Adv. Funct. Mater.*, vol. 29, p. 1901317, 2020/09/04 2019.

[54] D. Polak, R. Jayaprakash, T. P. Lyons, L. Á. Martínez-Martínez, A. Leventis, K. J. Fallon, H. Coulthard, D. G. Bossanyi, K. Georgiou, A. J. Petty, II, J. Anthony, H. Bronstein, J. Yuen-Zhou, A. I. Tartakovskii, J. Clark, and A. J. Musser, "Manipulating

molecules with strong coupling: Harvesting triplet excitons in organic exciton microcavities," *Chemical Science*, vol. 11, pp. 343–354, 2020.

[55] B. Gu and S. Mukamel, "Manipulating nonadiabatic conical intersection dynamics by optical cavities," *Chemical Science*, vol. 11, pp. 1290–1298, 2020.

[56] B. Liu, V. M. Menon, and M. Y. Sfeir, "The role of long-lived excitons in the dynamics of strongly coupled molecular polaritons," *ACS Photon.*, vol. 7, no. 8, pp. 2292–2301, 2020.

[57] O. Vendrell, "Collective jahn-teller interactions through light-matter coupling in a cavity," *Phys. Rev. Lett.*, vol. 121, p. 253001, Dec 2018.

[58] C. A. DelPo, B. Kudisch, K. H. Park, S.-U.-Z. Khan, F. Fassioli, D. Fausti, B. P. Rand, and G. D. Scholes, "Polariton transitions in femtosecond transient absorption studies of ultrastrong light–molecule coupling," *J. Phys. Chem. Lett.*, vol. 11, no. 7, pp. 2667–2674, 2020.

[59] P. G. Savvidis, L. G. Connolly, M. S. Skolnick, D. G. Lidzey, and J. J. Baumberg, "Ultrafast polariton dynamics in strongly coupled zinc porphyrin microcavities at room temperature," *Phys. Rev. B: Condens. Matter Mater. Phys.*, vol. 74, p. 113312, Sep 2006.

[60] M. Gouterman, "Study of the effects of substitution on the absorption spectra of porphin," *J. Chem. Phys.*, vol. 30, no. 5, pp. 1139–1161, 1959.

[61] D. G. Lidzey, D. D. C. Bradley, M. S. Skolnick, T. Virgili, S. Walker, and D. M. Whittaker, "Strong Exciton-Photon Coupling in an Organic Semiconductor Microcavity," *Nature*, vol. 395, no. 6697, pp. 53–55, 1998.

[62] H.-Z. Yu, J. S. Baskin, and A. H. Zewail, "Ultrafast dynamics of porphyrins in the

condensed phase: Ii. zinc tetraphenylporphyrin," *J. Phys. Chem. A*, vol. 106, no. 42, pp. 9845–9854, 2002.

[63] T. Kobayashi, D. Huppert, K. D. Straub, and P. M. Rentzepis, "Picosecond kinetics of copper and silver protoporphyrins," *The Journal of Chemical Physics*, vol. 70, no. 4, pp. 1720–1726, 1979.

[64] J. Rodriguez, C. Kirmaier, and D. Holten, "Optical properties of metalloporphyrin excited states," *Journal of the American Chemical Society*, vol. 111, no. 17, pp. 6500–6506, 1989.

[65] M.-H. Ha-Thi, N. Shafizadeh, L. Poisson, and B. Soep, "An efficient indirect mechanism for the ultrafast intersystem crossing in copper porphyrins," *J. Phys. Chem. A*, vol. 117, no. 34, pp. 8111–8118, 2013.

[66] D. Jeong, D.-g. Kang, T. Joo, and S. K. Kim, "Femtosecond-resolved excited state relaxation dynamics of copper (ii) tetraphenylporphyrin (cutpp) after soret band excitation," *Sci. Rep.*, vol. 7, no. 1, p. 16865, 2017.

[67] B. Gu and S. Mukamel, "Cooperative conical intersection dynamics of two pyrazine molecules in an optical cavity," *J. Phys. Chem. Lett.*, vol. 11, no. 14, pp. 5555–5562, 2020.

[68] B. Gu and S. Mukamel, "Optical-cavity manipulation of conical intersections and singlet fission in pentacene dimers," *J. Phys. Chem. Lett.*, vol. 12, no. 8, pp. 2052–2056, 2021.

[69] C. Lee, W. Yang, and R. G. Parr, "Development of the colle-salvetti correlation-energy formula into a functional of the electron density," *Phys. Rev. B*, vol. 37, pp. 785–789, Jan 1988.

[70] A. D. Becke, "Density-functional thermochemistry. iii. the role of exact exchange," *J. Chem. Phys.*, vol. 98, no. 7, pp. 5648–5652, 1993.

[71] P. J. Stephens, F. J. Devlin, C. F. Chabalowski, and M. J. Frisch, "Ab initio calculation of vibrational absorption and circular dichroism spectra using density functional force fields," *J. Phys. Chem.*, vol. 98, pp. 11623–11627, 11 1994.

[72] M. J. Frisch, G. W. Trucks, H. B. Schlegel, G. E. Scuseria, M. A. Robb, J. R. Cheeseman, G. Scalmani, V. Barone, G. A. Petersson, H. Nakatsuji, X. Li, M. Caricato, A. V. Marenich, J. Bloino, B. G. Janesko, R. Gomperts, B. Mennucci, H. P. Hratchian, J. V. Ortiz, A. F. Izmaylov, J. L. Sonnenberg, D. Williams-Young, F. Ding, F. Lipparini, F. Egidi, J. Goings, B. Peng, A. Petrone, T. Henderson, D. Ranasinghe, V. G. Zakrzewski, J. Gao, N. Rega, G. Zheng, W. Liang, M. Hada, M. Ehara, K. Toyota, R. Fukuda, J. Hasegawa, M. Ishida, T. Nakajima, Y. Honda, O. Kitao, H. Nakai, T. Vreven, K. Throssell, J. A. Montgomery, Jr., J. E. Peralta, F. Ogliaro, M. J. Bearpark, J. J. Heyd, E. N. Brothers, K. N. Kudin, V. N. Staroverov, T. A. Keith, R. Kobayashi, J. Normand, K. Raghavachari, A. P. Rendell, J. C. Burant, S. S. Iyengar, J. Tomasi, M. Cossi, J. M. Millam, M. Klene, C. Adamo, R. Cammi, J. W. Ochterski, R. L. Martin, K. Morokuma, O. Farkas, J. B. Foresman, and D. J. Fox, "Gaussian∼16 Revision C.01," 2016. Gaussian Inc. Wallingford CT.

[73] R. J. Holmes and S. R. Forrest, "Strong exciton-photon coupling and exciton hybridization in a thermally evaporated polycrystalline film of an organic small molecule," *Phys. Rev. Lett.*, vol. 93, p. 186404, Oct 2004.

[74] Y. Tsuchimoto, H. Nagai, M. Amano, K. Bando, and H. Kondo, "Cavity polaritons in an organic single-crystalline rubrene microcavity," *Applied Physics Letters*, vol. 104,

no. 23, p. 233307, 2014.

[75] S.-H. Lim, T. G. Bjorklund, F. C. Spano, and C. J. Bardeen, "Exciton delocalization and superradiance in tetracene thin films and nanoaggregates," *Phys. Rev. Lett.*, vol. 92, p. 107402, Mar 2004.

[76] A. L. Stancik and E. B. Brauns, "A simple asymmetric lineshape for fitting infrared absorption spectra," *Vib. Spec.*, vol. 47, no. 1, pp. 66–69, 2008.

[77] D. M. Whittaker, "What determines inhomogeneous linewidths in semiconductor microcavities?," *Phys. Rev. Lett.*, vol. 80, pp. 4791–4794, May 1998.

[78] F. Tassone, C. Piermarocchi, V. Savona, A. Quattropani, and P. Schwendimann, "Bottleneck effects in the relaxation and photoluminescence of microcavity polaritons," *Phys. Rev. B*, vol. 56, pp. 7554–7563, Sep 1997.

[79] J. Mony, M. Hertzog, K. Kushwaha, and K. Börjesson, "Angle-independent polariton emission lifetime shown by perylene hybridized to the vacuum field inside a fabry–pérot cavity," *J. Phys. Chem. C*, vol. 122, no. 43, pp. 24917–24923, 2018.

[80] R. A. Cowley, "Anharmonic crystals," *Rep. Prog. Phys.*, vol. 31, no. 1, p. 123, 1968.

[81] J. Menéndez and M. Cardona, "Temperature dependence of the first-order raman scattering by phonons in si, ge, and $\alpha - \mathrm{Sn}$: Anharmonic effects," *Phys. Rev. B*, vol. 29, pp. 2051–2059, Feb 1984.

[82] R. Cuscó, E. Alarcón-Lladó, J. Ibáñez, L. Artús, J. Jiménez, B. Wang, and M. J. Callahan, "Temperature dependence of raman scattering in $\mathrm{ZnO}$," *Phys. Rev. B*, vol. 75, p. 165202, Apr 2007.

[83] A. M. Sanni, S. N. Lavan, and A. S. Rury, "Anharmonic molecular vibrational probes

of dynamical organic–inorganic interactions in two-dimensional hybrid lead iodide perovskites," *J. Phys. Chem. C*, vol. 124, pp. 13942–13955, 2020.

[84] H. Zoubi and G. C. La Rocca, "Microscopic theory of nonlinear polariton interactions in strongly coupled hybrid organic-inorganic microcavities," *Phys. Rev. B*, vol. 76, p. 035325, Jul 2007.

[85] T. Nishimura, K. Yamashita, S. Takahashi, T. Yamao, S. Hotta, H. Yanagi, and M. Nakayama, "Quantitative evaluation of light-matter interaction parameters in organic single-crystal microcavities," *Opt. Lett.*, vol. 43, pp. 1047–1050, Mar 2018.

[86] L. Mewes, M. Wang, R. A. Ingle, K. Börjesson, and M. Chergui, "Energy relaxation pathways between light-matter states revealed by coherent two-dimensional spectroscopy," *Comm. Phys.*, vol. 3, no. 1, p. 157, 2020.

[87] J. J. Hopfield, "Theory of the contribution of excitons to the complex dielectric constant of crystals," *Phys. Rev.*, vol. 112, pp. 1555–1567, Dec 1958.

[88] N. Somaschi, L. Mouchliadis, D. Coles, I. E. Perakis, D. G. Lidzey, P. G. Lagoudakis, and P. G. Savvidis, "Ultrafast polariton population build-up mediated by molecular phonons in organic microcavities," *Appl. Phys. Lett.*, vol. 99, no. 14, p. 143303, 2011.

[89] D. M. Coles, P. Michetti, C. Clark, W. C. Tsoi, A. M. Adawi, J.-S. Kim, and D. G. Lidzey, "Vibrationally assisted polariton-relaxation processes in strongly coupled organic-semiconductor microcavities," *Adv. Funct. Mater.*, vol. 21, pp. 3691–3696, 2019/10/27 2011.

[90] A. S. Rury, L. E. Goodrich, M. G. I. Galinato, N. Lehnert, and R. J. Sension, "Ligand

recruitment and spin transitions in the solid-state photochemistry of fe(iii)tppcl," *J. Phys. Chem. A*, vol. 116, no. 32, pp. 8321–8333, 2012.

[91] A. S. Rury, T. E. Wiley, and R. J. Sension, "Energy cascades, excited state dynamics, and photochemistry in cob(iii)alamins and ferric porphyrins," *Acc. Chem. Res.*, vol. 48, no. 3, pp. 860–867, 2015.

[92] M. Bixon and J. Jortner, "Intramolecular radiationless transitions," *J. Chem. Phys.*, vol. 48, no. 2, pp. 715–726, 1968.

[93] P. Michetti and G. C. La Rocca, "Exciton-phonon scattering and photoexcitation dynamics in $j$-aggregate microcavities," *Phys. Rev. B*, vol. 79, p. 035325, Jan 2009.

[94] M. Asano, Y. Kaizu, and H. Kobayashi, "The lowest excited states of copper porphyrins," *The Journal of Chemical Physics*, vol. 89, no. 11, pp. 6567–6576, 1988.

[95] V. N. Peters, M. O. Faruk, J. Asane, R. Alexander, D. A. Peters, S. Prayakarao, S. Rout, and M. A. Noginov, "Effect of strong coupling on photodegradation of the semiconducting polymer p3ht," *Optica*, vol. 6, pp. 318–325, Mar 2019.

[96] A. B. Grafton, A. D. Dunkelberger, B. S. Simpkins, J. F. Triana, F. J. Hernández, F. Herrera, and J. C. Owrutsky, "Excited-state vibration-polariton transitions and dynamics in nitroprusside," *Nat. Comm.*, vol. 12, no. 1, p. 214, 2021.

[97] A. S. Rury, S. Sorenson, E. Driscoll, and J. M. Dawlaty, "Electronic State-Resolved Electron-Phonon Coupling in an Organic Charge Transfer Material from Broadband Quantum Beat Spectroscopy," *J. Phys. Chem. Lett.*, vol. 6, pp. 3560–3564, 2015.

[98] A. S. Rury, S. A. Sorenson, and J. M. Dawlaty, "Coherent vibrational probes of hydrogen bond structure following ultrafast electron transfer," *J. Phys. Chem. C*, vol. 120, no. 38, pp. 21740–21750, 2016.

[99] A. S. Rury, S. A. Sorenson, and J. M. Dawlaty, "Evidence of ultrafast charge transfer driven by coherent lattice vibrations," *J. Phys. Chem. Lett.*, vol. 8, pp. 181–187, 2017.

[100] R. E. McAnally, J. A. Bender, L. Estergreen, R. Haiges, S. E. Bradforth, J. M. Dawlaty, S. T. Roberts, and A. S. Rury, "Defects Cause Subgap Luminescence from a Crystalline Tetracene Derivative," *J. Phys. Chem. Lett.*, vol. 8, pp. 5993–6001, 2017.

[101] D. Sanvitto and S. Kéna-Cohen, "The road towards polaritonic devices," *Nat. Mater.*, vol. 15, no. July, pp. 1061–1073, 2016.

[102] A. G. Avramenko and A. S. Rury, "Local molecular probes of ultrafast relaxation channels in strongly coupled metalloporphyrin-cavity systems," *J. Chem. Phys.*, vol. 155, no. 6, p. 064702, 2021.

[103] T. Schwartz, J. A. Hutchison, C. Genet, and T. W. Ebbesen, "Reversible switching of ultrastrong light-molecule coupling," *Phys. Rev. Lett.*, vol. 106, p. 196405, May 2011.

[104] F. C. Spano, "The spectral signatures of frenkel polarons in h- and j-aggregates," *Acc. Chem. Res.*, vol. 43, no. 3, pp. 429–439, 2010.

[105] R. J. Holmes and S. R. Forrest, "Exciton-photon coupling in organic materials with large intersystem crossing rates and strong excited-state molecular relaxation," *Phys. Rev. B: Condens. Matter Mater. Phys.*, vol. 71, p. 235203, Jun 2005.

[106] J. A. Shelnutt, "A simple interpretation of raman excitation spectra of metalloporphyrins," *J. Chem. Phys.*, vol. 74, no. 12, pp. 6644–6657, 1981.

[107] G. Orlandi and W. Siebrand, "Theory of vibronic intensity borrowing: Comparison

of herzberg - teller and born - oppenheimer coupling," *J. Chem. Phys.*, vol. 58, no. 10, pp. 4513–4523, 1973.

[108] J. Du, T. Teramoto, K. Nakata, E. Tokunaga, and T. Kobayashi, "Real-time vibrational dynamics in chlorophyll a studied with a few-cycle pulse laser," *Biophys. J.*, vol. 101, no. 4, pp. 995–1003, 2011.

[109] J. R. Reimers, Z.-L. Cai, R. Kobayashi, M. Rätsep, A. Freiberg, and E. Krausz, "Assignment of the q-bands of the chlorophylls: Coherence loss via $q_x$-$q_y$ mixing," *Sci. Rep.*, vol. 3, no. 1, p. 2761, 2013.

[110] F. D. Fuller, J. Pan, A. Gelzinis, V. Butkus, S. S. Senlik, D. E. Wilcox, C. F. Yocum, L. Valkunas, D. Abramavicius, and J. P. Ogilvie, "Vibronic coherence in oxygenic photosynthesis," *Nat. Chem.*, vol. 6, no. 8, pp. 706–711, 2014.

[111] V. Perlík, J. Seibt, L. J. Cranston, R. J. Cogdell, C. N. Lincoln, J. Savolainen, F. Šanda, T. Mančal, and J. Hauer, "Vibronic coupling explains the ultrafast carotenoid-to-bacteriochlorophyll energy transfer in natural and artificial light harvesters," *J. Chem. Phys.*, vol. 142, no. 21, p. 212434, 2015.

[112] J. Lim, D. Paleček, F. Caycedo-Soler, C. N. Lincoln, J. Prior, H. von Berlepsch, S. F. Huelga, M. B. Plenio, D. Zigmantas, and J. Hauer, "Vibronic origin of long-lived coherence in an artificial molecular light harvester," *Nat. Comm.*, vol. 6, no. 1, p. 7755, 2015.

[113] D. M. Jonas, "Vibrational and nonadiabatic coherence in 2d electronic spectroscopy, the jahn–teller effect, and energy transfer," *Ann. Rev. Phys. Chem.*, vol. 69, no. 1, pp. 327–352, 2018. PMID: 29677467.

[114] E. A. Arsenault, Y. Yoneda, M. Iwai, K. K. Niyogi, and G. R. Fleming, "Vibronic

mixing enables ultrafast energy flow in light-harvesting complex ii," *Nat. Comm.*, vol. 11, no. 1, p. 1460, 2020.

[115] E. A. Arsenault, Y. Yoneda, M. Iwai, K. K. Niyogi, and G. R. Fleming, "The role of mixed vibronic qy-qx states in green light absorption of light-harvesting complex ii," *Nat. Comm.*, vol. 11, no. 1, p. 6011, 2020.

[116] E. Bukartė, A. Haufe, D. Paleček, C. Büchel, and D. Zigmantas, "Revealing vibronic coupling in chlorophyll c1 by polarization-controlled 2d electronic spectroscopy," *Chem. Phys.*, vol. 530, p. 110643, 2020.

[117] M. Reppert, "Delocalization effects in chlorophyll fluorescence: Nonperturbative line shape analysis of a vibronically coupled dimer," *J. Phys. Chem. B*, vol. 124, no. 45, pp. 10024–10033, 2020.

[118] C. C. Rich and R. R. Frontiera, "Vibronic coupling and exciton chirality: Electronic and structural rearrangement between helical to zero momentum molecular exciton states," *J. Phys. Chem. C*, vol. 125, no. 39, pp. 21511–21520, 2021.

[119] J. S. Higgins, L. T. Lloyd, S. H. Sohail, M. A. Allodi, J. P. Otto, R. G. Saer, R. E. Wood, S. C. Massey, P.-C. Ting, R. E. Blankenship, and G. S. Engel, "Photosynthesis tunes quantum-mechanical mixing of electronic and vibrational states to steer exciton energy transfer," *Proc. Natl. Acad. Sci. U.S.A*, vol. 118, no. 11, 2021.

[120] J. S. Higgins, M. A. Allodi, L. T. Lloyd, J. P. Otto, S. H. Sohail, R. G. Saer, R. E. Wood, S. C. Massey, P.-C. Ting, R. E. Blankenship, and G. S. Engel, "Redox conditions correlated with vibronic coupling modulate quantum beats in photosynthetic pigment–protein complexes," *Proc. Natl. Acad. Sci. U.S.A*, vol. 118, no. 49, 2021.

[121] C.-J. Yu, M. D. Krzyaniak, M. S. Fataftah, M. R. Wasielewski, and D. E. Freedman,

"A concentrated array of copper porphyrin candidate qubits," *Chem. Sci.*, vol. 10, pp. 1702–1708, 2019.

[122] J. A. Shelnutt and D. C. O'Shea, "Resonance raman spectra of copper tetraphenylporphyrin: Effects of strong vibronic coupling on excitation profiles and the absorption spectrum," *The Journal of Chemical Physics*, vol. 69, no. 12, pp. 5361–5374, 1978.

[123] J. A. Shelnutt and V. Ortiz, "Substituent effects on the electronic structure of metalloporphyrins: a quantitative analysis in terms of four-orbital-model parameters," *J. Phys. Chem.*, vol. 89, no. 22, pp. 4733–4739, 1985.

[124] F. Herrera and F. C. Spano, "Dark vibronic polaritons and the spectroscopy of organic microcavities," *Phys. Rev. Lett.*, vol. 118, p. 223601, May 2017.

[125] F. Herrera and F. C. Spano, "Absorption and photoluminescence in organic cavity qed," *Phys. Rev. A: At., Mol., Opt. Phys.*, vol. 95, p. 053867, May 2017.

[126] L. Mazza, L. Fontanesi, and G. C. La Rocca, "Organic-based microcavities with vibronic progressions: Photoluminescence," *Phys. Rev. B: Condens. Matter Mater. Phys.*, vol. 80, p. 235314, Dec 2009.

[127] P. Meystre and M. Sargent, *Elements of Quantum Optics*. Springer, Berlin-Heidelberg, 2007.

[128] J. R. Widom, W. Lee, A. Perdomo-Ortiz, D. Rappoport, T. F. Molinski, A. Aspuru-Guzik, and A. H. Marcus, "Temperature-dependent conformations of a membrane supported zinc porphyrin tweezer by 2d fluorescence spectroscopy," *J. Phys. Chem. A*, vol. 117, no. 29, pp. 6171–6184, 2013.

[129] V. Tiwari, Y. A. Matutes, A. T. Gardiner, T. L. C. Jansen, R. J. Cogdell, and J. P.

Ogilvie, “Spatially-resolved fluorescence-detected two-dimensional electronic spectroscopy probes varying excitonic structure in photosynthetic bacteria,” *Nat. Comm.*, vol. 9, no. 1, p. 4219, 2018.

[130] V. Tiwari, Y. A. Matutes, A. Konar, Z. Yu, M. Ptaszek, D. F. Bocian, D. Holten, C. Kirmaier, and J. P. Ogilvie, “Strongly coupled bacteriochlorin dyad studied using phase-modulated fluorescence-detected two-dimensional electronic spectroscopy,” *Opt. Ex.*, vol. 26, pp. 22327–22341, Aug 2018.

[131] A. Tamimi, T. Landes, J. Lavoie, M. G. Raymer, and A. H. Marcus, “Fluorescence-detected fourier transform electronic spectroscopy by phase-tagged photon counting,” *Opt. Ex.*, vol. 28, pp. 25194–25214, Aug 2020.

[132] D. Agathangelou, A. Javed, F. Sessa, X. Solinas, M. Joffre, and J. P. Ogilvie, “Phase-modulated rapid-scanning fluorescence-detected two-dimensional electronic spectroscopy,” *J. Chem. Phys.*, vol. 155, no. 9, p. 094201, 2021.

[133] S. D. Barrett, P. Kok, K. Nemoto, R. G. Beausoleil, W. J. Munro, and T. P. Spiller, “Symmetry analyzer for nondestructive bell-state detection using weak nonlinearities,” *Phys. Rev. A: At., Mol., Opt. Phys.*, vol. 71, p. 060302, Jun 2005.

[134] J. L. O’Brien, “Optical quantum computing,” *Science*, vol. 318, no. 5856, pp. 1567–1570, 2007.

[135] B. Hacker, S. Welte, G. Rempe, and S. Ritter, “A photon–photon quantum gate based on a single atom in an optical resonator,” *Nature*, vol. 536, no. 7615, pp. 193–196, 2016.

[136] S. Slussarenko and G. J. Pryde, “Photonic quantum information processing: A concise review,” *Appl. Phys. Rev.*, vol. 6, no. 4, p. 041303, 2019.

[137] M. Hertzog, M. Wang, J. Mony, and K. Börjesson, "Strong light–matter interactions: a new direction within chemistry," *Chemical Society Reviews*, vol. 48, no. 3, pp. 937–961, 2019.

[138] J. Wainstain, C. Delalande, D. Gendt, M. Voos, J. Bloch, V. Thierry-Mieg, and R. Planel, "Dynamics of polaritons in a semiconductor multiple-quantum-well microcavity," *Physical Review B*, vol. 58, no. 11, p. 7269, 1998.

[139] A. G. Avramenko and A. S. Rury, "Polariton-mediated coupling of quasi-degenerate porphyrin excitons," in *Frontiers in Optics*, pp. JTh5A–107, Optical Society of America, 2021.

[140] D. G. Lidzey, D. D. C. Bradley, A. Armitage, S. Walker, and M. S. Skolnick, "Photon-mediated hybridization of frenkel excitons in organic semiconductor microcavities," *Science*, vol. 288, no. 5471, pp. 1620–1623, 2000.

[141] P. Kinsler and D. Whittaker, "Linewidth narrowing of polaritons," *Physical Review B*, vol. 54, no. 7, p. 4988, 1996.

[142] V. Savona, C. Piermarocchi, A. Quattropani, F. Tassone, and P. Schwendimann, "Microscopic theory of motional narrowing of microcavity polaritons in a disordered potential," *Physical Review Letters*, vol. 78, no. 23, p. 4470, 1997.

[143] C. Bardeen, Q. Wang, and C. Shank, "Selective excitation of vibrational wave packet motion using chirped pulses," *Physical review letters*, vol. 75, no. 19, p. 3410, 1995.

[144] A. M. Sanni, S. N. Lavan, A. Avramenko, F. A. Rabuffetti, L. Suescun, and A. S. Rury, "Room-temperature broadband light emission from hybrid lead iodide perovskite-like quantum wells: Terahertz spectroscopic investigation of metastable defects," *The Journal of Physical Chemistry Letters*, vol. 10, no. 8, pp. 1653–1662, 2019.

[145] M. C. Weidman, M. Seitz, S. D. Stranks, and W. A. Tisdale, "Highly tunable colloidal perovskite nanoplatelets through variable cation, metal, and halide composition," *ACS nano*, vol. 10, no. 8, pp. 7830–7839, 2016.

[146] M. R. Wasielewski, "Photoinduced electron transfer in supramolecular systems for artificial photosynthesis," *Chem. Rev.*, vol. 92, no. 3, pp. 435–461, 1992.

[147] I. H. Malitson, "Interspecimen comparison of the refractive index of fused silica," *Josa*, vol. 55, no. 10, pp. 1205–1209, 1965.

[148] R. Blümel, M. Bağcioğlu, R. Lukacs, and A. Kohler, "Infrared refractive index dispersion of polymethyl methacrylate spheres from mie ripples in fourier-transform infrared microscopy extinction spectra," *JOSA A*, vol. 33, no. 9, pp. 1687–1696, 2016.

[149] K. Luke, Y. Okawachi, M. R. Lamont, A. L. Gaeta, and M. Lipson, "Broadband mid-infrared frequency comb generation in a si 3 n 4 microresonator," *Optics letters*, vol. 40, no. 21, pp. 4823–4826, 2015.

**ABSTRACT**

**PHOTOPHYSICS OF METALLOPORPHYRINS STRONGLY COUPLED TO CAVITY PHOTONS**

by

**ALEKSANDR GREGOROVICH AVRAMENKO**

**August 2022**

**Advisor:** Dr. Aaron Rury

**Major:** Physical Chemistry

**Degree:** Doctor of Philosophy

This dissertation will discuss the photophysics of metalloporphyrins, mainly CuTPP, ZnTPP, and $H_2$TPP under strong light-matter coupling conditions. Strong light-matter coupling was achieved by embedding the previously mentioned chromophores into a spun coated PMMA polymer coating which is then incorporated as a spacer layer in a Fabry-Pérot nano-cavity. The cavity thickness is chosen so that the cavity photon is of similar energy as the B, or Soret transition (2nd excited state) of the porphyrin molecule. The exchange of energy between the cavity photon and the molecular mode leads to the formation of polariton states.

Increasing the concentration of the molecules leads to an increase in the Rabi splitting, or the splitting between the polariton states. By increasing the Rabi splitting the lower polariton is pushed closer in energy to that of the porphyrin's 1st excited state (Q band). By doing this we observe an increase in the rate of nonradiative relaxation between the LP and the 1st excited state of ZnTPP. However, this rate does not follow the established gap law. We attribute this to interpolariton decay channels which play an important role

in determining the dynamics of polaritons.

We also observe an increase in CuTPP emission in the region of the 1st excited state under strong light-matter coupling conditions. By constructing a set of multi-layer cavities we are able to account for the Purcell effect which may be responsible for this feature. We determine that using the CuTPP Soret band to form polaritons also produces a lower lying polariton state slightly below the Q band. We attribute this to vibronic coupling between the Q band and the now hybridized B band ($S_2$ state) of our cavity system. Moreover, we observe that the emission from this state is greatly amplified when the energy difference between the lower lying $\nu_2$ cavity mode and the HT polariton matches the vibration energy of the collective vibrational states.

We extend the multi-layer cavity system to include a layer of $H_2$TPP, whose Soret band is nearly degenerate with that of CuTPP. Using a 3x3 oscillator Hamiltonian we determine that despite their near degeneracy, the resulting polaritons inherit unique excitonic characteristics. We observe that the lower polariton is dominated by the $H_2$TPP exciton fraction, while CuTPP is the dominant exciton fraction in the upper polariton. Moreover, we determine that the photonic contribution to the middle polariton is small at all angles. We also observe a narrowing of the lower polariton lineshapes near the resonance angles, suggesting that polariton motional narrowing must be considered when modeling the dynamics of molecular polaritons.

**AUTOBIOGRAPHICAL STATEMENT**

**Aleksandr Gregorovich Avramenko**

## Education

Wayne State University, Ph.D. August 2022
Detroit, MI
Major: Physical Chemistry
Advisor: Aaron Rury

Eastern Michigan University, M.S. April 2017
Ypsilanti, MI
Major: Polymer and coatings technology
Advisor: Vijay Mannari

Northern Michigan University, B.S. May 2014
Marquette, MI
Major: Chemistry, Economics
Advisor: Mark Paulsen

## Publications

**Aleksandr G. Avramenko**, Aaron S. Rury, Light Emission from Vibronic Polaritons in Coupled Metalloporphyrin-Multimode Cavity Systems Systems, *The Journal of Physical Chemistry Letters*, 2022, 13, 18, 4036–4045.

**Aleksandr G. Avramenko**, Aaron S. Rury, Local molecular probes of ultrafast relaxation channels in strongly coupled metalloporphyrin-cavity systems, *The Journal of Chemical Physics*, 2021, 155, 6, 064702.

**Aleksandr G. Avramenko**, Aaron S. Rury, Quantum Control of Ultrafast Internal Conversion using Nano-Confined Virtual Photons, *The Journal of Physical Chemistry Letters*, 2020 11, 3, 1013-1021.

**Aleksandr G. Avramenko**, Aaron S. Rury, Interrogating the Structure of Molecular Cavity Polaritons with Resonance Raman Scattering: An Experimentally Motivated Theoretical Description, *Journal of Physical Chemistry C*, 2019, 123, 50, 30551-30561.

Adedayo M. Sanni, Sydney N. Lavan, **Aleksandr Avramenko**, Federico A. Rabuffetti, Leopoldo Suescun, and Aaron S. Rury, Room-Temperature Broadband Light Emission from Hybrid Lead Iodide Perovskite-Like Quantum Wells: Terahertz Spectroscopic Investigation of Metastable Defects, *The Journal of Physical Chemistry Letters*, 2018, 10, 8, 1653-1662.